Faculty of Engineering of the University of Porto

Battery cell materials with Scanning Kelvin Probe and Electrochemical Analysis

António Nuno de Sousa Chaves Guerreiro

Master in Electrical and Computer Engineering
Major Energy

Supervisor: Prof. Dr. Maria Helena Sousa Soares de Oliveira Braga
Co-Supervisor: Prof. Dr. José Rui da Rocha Pinto Ferreira

July 2022

Resumo

A maior conquista socioeconómica da humanidade foi a descoberta da eletricidade e sua relevância global, conduzindo a uma mudança de paradigma. Desde a mais simples utilização doméstica até a um nível industrial, todas dependem da "matéria prima" eletricidade. Seria impensável viver sem energia hoje em dia. A crescente necessidade de energia atingiu níveis nunca previstos. Parte considerável desse crescimento deveu-se ao consumo de energias fósseis, suprindo as necessidades energéticas, e sacrificando o equilíbrio ecológico do planeta.

Devido ao uso extremo de combustíveis fósseis, o mundo encontra-se em desequilíbrio, ambiental, havendo as respetivas repercussões socioeconómicas. Desde o Protocolo de Kyoto, com o acordo de redução de gases, até ao mais recente, em Paris, tem sido feito um esforço de mudança e criação de novos sistemas económico-políticos, de transição energética para um abastecimento energético sustentável e estável. A combinação das crescentes necessidades energéticas, problemas ambientais associados, e atual situação de necessidade emergente de fornecimento de energia, leva à procura de processos mais "verdes" de produção de energia associada a sistemas de armazenamento de energia eficientes. Este facto exige que sejam feitos ajustes significativos nos métodos de sistemas de energia e tecnologia digital para garantir os próximos anos, garantindo a segurança do fornecimento de energia e competitividade económica sustentável.

Diversos aparelhos de uso corrente, desde um simples telemóvel até equipamentos aeroespaciais, são feitos de variados materiais e são criteriosamente escolhidos para que o seu comportamento e controle sejam mais confiáveis, tendendo a ser mais limpos e menos dispendiosos. O desenvolvimento destes está diretamente relacionado à escolha criteriosa dos materiais, sua natureza, estrutura, características morfológicas, contaminantes ou dopantes e energia de ionização. Esses parâmetros são de suma importância para a qualidade e funcionamento de diversos dispositivos, altamente dependentes da estrutura, condições da superfície e composição básica do material em estudo. Neste sentido, a técnica SKP é uma ferramenta útil que pode medir parâmetros relativos a materiais, em diversas áreas de estudo para a atualização de diversos equipamentos. A análise de materiais de células e baterias, como condutores (cobre, alumínio e zinco), dielétricos (óxidos) e isolantes (óxidos e cortiça), pode ser complementada por Impedância por Espectroscopia (EIS) para caracterização eletroquímica do par de metais com eletrólito sólido ou óxidos, como o ZnO. Esta pode ser uma área de melhoria de células/baterias e campos que estejam relacionados. O ZnO é um dielétrico com ampla gama de aplicações tecnológicas, na saúde e indústrias adequadas, sendo de baixo custo, seguro e estável. O ZnO foi estudado com detalhe.

Página em branco

Abstract

The greatest socio-economic achievement of humankind was the discovery of electricity and its usefulness for all of us, which was an overwhelming change of the paradigm. From the smallest domestic utilization to the largest industries, all rely upon electricity. It would be unthinkable to live without energy nowadays. The growing need for energy was tremendous and rocked to levels never previewed. A considerable part of this growth was due to fossil energies, fulfilling energy needs, and sacrificing the ecological balance of the planet.

Due to the extreme use of fossil fuels, the world finds itself in an imbalance, environmentally speaking. From Kyoto Protocol, with gases reduction agreement, to the most recent, in Paris, an effort has been made for changes and the creation of new economic-political systems for energy transition for a sustainable and stable energy supply. Due to the growing energy needs, the environmental problems associated, and the current situation with the emerging need for energy supply, there is an immense need for clean energy and energy storage systems. These require significant adjustments to be made in energy power systems methods and digital technology to ensure years to come, ensuring the security of energy supply and sustainable economic competitiveness.

Several devices of our daily life, from a simple mobile phone to aerospace equipment, are made of various materials and are carefully chosen so that their behavior and control are more reliable, tending to be cleaner and less expensive. The improvement of these is directly related to the choice and improvement of materials, their nature, structure, morphological characteristics, contaminants or dopants, and ionization energy. These parameters are of paramount importance for various devices' quality and operation. These quantities depend highly on the structure, surface conditions, and basic composition of the material under study. Thus, the SKP technique is a useful tool that can measure parameters concerning materials in various fields of study for the improvement of devices such as cells and batteries and materials like conductors (copper, aluminium and zinc), dielectrics (oxides) and insulators (oxides and cork). These studies can be complemented by Impedance Spectroscopy (EIS) for electrochemistry characterization of the pair of metals with solid electrolytes or oxides, such as ZnO. An improvement in cell/battery features and related fields is expected. ZnO is a dielectric with a wide range of features suitable for technology, health and industrial applications, being low-cost, safe and stable. Here ZnO was studied in detail.

Página em branco

Acknowledgments

I would like to express my deepest gratitude to all who contributed to my learning and achievement of results.

Firstly, I would like to thank my supervisor, Professor Maria Helena Braga, for all her compelling words, guidance, and support. Thanks for teaching me objectivity and precision.

I would also like to thank Professor Rui Ferreira for his kindness and motivational words.

Thank you to the MatER staff for your companionship.

I would like to thank very much Mr. Ramiro Soares for his goodwill and help.

Finally, to my family and close friends for being there whenever needed.

Página em branco

Contents

List of figures

Abbreviation and Symbols

AC Alternate Current
AFM Atomic Force Microscopy
CHM Capacitive Height Measurement
CPD Contact Potential Difference
CTM Capacitive Tracking Measurement
DC Direct Current
EFM Electric Force Microscopy
EIS Electrochemical Impedance Spectroscopy
EEP External Electric Potential
ITO Indium Tin Oxide
IUPAC
Intermittent contact Scanning Electrochemical Microscopy (ic-SECM)
LIA Lock-in Amplifier
SEM Scanning Electron Microscopy
SECM Scanning Electro-Chemical Microscopy
SKP Scanning Kelvin Probe
SPM Scanning Probe Microscopy
STM Scanning Tunneling Microscopy
SFOM Scanning near-field Optical Microscopy
TFT Thin Film Transistors
OSP Non-Contact Optical Surface Profiling
OCV Open Circuit Voltage
SHE Standard Hydrogen Electrode

Symbol list

Al	Aluminium
Cu	Copper
E	Energy
E_F	Fermi level
K	Boltzmann constant
Q	Charge
T	Temperature

Zn	Zinc
ZnO	Zinc oxide
ε_0	Permittivity of free space
ε_r	Relative permittivity
φ	Work function
μ	chemical potential
ω	Angular frequency

Chapter 1

1.1 - Introduction and motivation

In recent years we have witnessed rapid technological development alongside greater energy production and consumption. Since the 1980s until today, we have been aware of the negative consequences of pollution generated by fossil fuels. In recent decades, energy policies have been implemented, invested in and stimulated to mitigate and reduce the adverse effects that we have been experiencing such as climate change.

The effort to change the attitude toward equilibrium and sustainable path is also made in the search for new materials that are efficient, green, safe and clean. In the field of energy storage there is still a long way to go, although there have been important developments. Lithium batteries have revolutionized our relationship with many everyday devices such as cell phones and laptops. It would also be desirable for other applications where the energy requirement is higher, such as for renewable energy equipment or electric vehicles, where further development and maturity are required.

The study and search for new materials are essential to improve energy storage systems, in order to be an active partner in the energy transition, power systems, renewable energies and new technologies. The study of a material to be used in equipment goes through its intrinsic characteristics, interaction with other materials, treatment of the material and analysis of surface phenomena at the micro scale.

The emerging Scanning Probe technology (SKP) based Atomic Force Microscopy (AFM) technique, is able to analyze the surface of materials (conductors, semiconductors and dielectrics), being a non-destructive and non-contact method. In this way, it may contribute to point to improvements and study new materials for batteries and cells, such as zinc oxide (ZnO), being the main goals of this study. SKP method is based on the work function characteristic of each material sample, which is related to its surface condition. The applications of SKP can also be suitable to evaluate the surface conditions of the material under study and the changes to the material that has been subjected, such as corrosion. Thus, this work can be more comprehensive and contribute to areas and studies, such as semiconductors. The electrochemical study was complemented with another technique, Electrochemical Impedance Spectroscopy (EIS), to study the system's impedance.

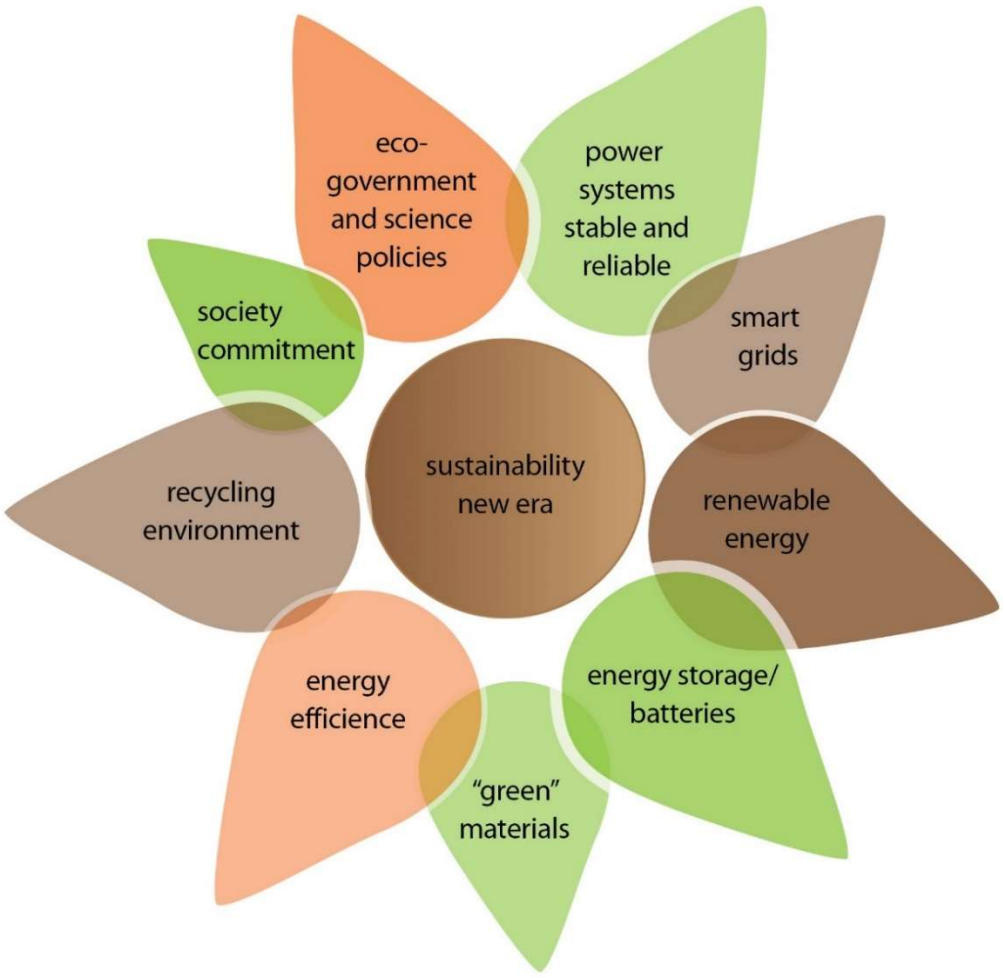

Figure 1. New challenges for energy systems

1.2 - Thesis framework

The present work intends to study the dynamics and behavior of the surfaces of various materials used in the constituents of cells and batteries. Among these are copper, aluminum, and zinc metallic electrodes. In addition to these, insulating materials for structural batteries, cork, and zinc oxide (ZnO) were studied. In the case of ZnO, its properties are used as a dielectric, placed between two pairs of battery-type metals, double heterojunctions. These will be the main components of this work.

The surface study of the different materials was carried out using the highly sensitive SKP technique, which made it possible to map all the surfaces of the samples of the proposed materials and to study the evolution of the electrical contact potential difference between the surface of these materials and a known standard material (SKP tip). Any surface alteration, such as oxidation

or contamination, influences the analysis of samples. The experiments were carried out on the Biological Instruments M470 electrochemical station.

The results obtained by the SKP were recorded by the specific software of the electrochemical station of Biological Instruments. Data were processed in OriginPro 2022.

The cell system impedance study was performed on the Gamry 1000, and the data were recorded in the specific software EC-Lab V11.02 from Biological Instruments. Calculations for the system equivalent circuit were also done in EC-Lab V11.02. The crystal structures of the molecules were built with *Vestas* software.

1.3 - Thesis roadmap

The thesis is structured and divided as follows:

Chapter 2 describes the evolution and introduces the principles and applications of the SKP. Topographic techniques (CTM and CHM) and the notion of working function are also described.

Chapter 3 is divided into two main parts: the first one is the characterization of metal materials copper, aluminum and zinc. Description and characterization of other non-metallic materials: zinc oxide and cork. Present the description of the cells in study. The other part is the preparation of the sample materials and cells. The experimental methods used in this work are described in this chapter.

Chapter 4 presents the results and discussion of the experiences. Firstly, is the study of metal elements copper, aluminum, and zinc. Secondly, it presents and analyzes the single heterojunctions structures copper/aluminium, copper/zinc, zinc/aluminium and cork/copper tape. In section 4.3.2 is presented and analyzed the case study of ZnO: double heterojunctions Cu/ZnO/Al and Cu/ZnO/Zn.

Chapter 5 presents the sum analysis and the conclusions of the study of the materials, cells, single and double heterojunctions of this work.

Chapter 6 gives a perspective and future works that would be interesting to compare with other materials (Al_2O_3, Li_2O, CaO, MgO, SiO and SnO_2) and techniques.

Chapter 7 summarizes the research assets of the author who has done and participated in this and related fields.

Appendix 3 contains the published article intitule “Interfacial chemistry with ZnO: in operating work functions in hetero cells”. It also includes the SKP experimental results sheets of Cu/ZnO/Al (appendix 1) and Cu/ZnO/Zn (appendix 2) cell heterojunctions.

Chapter 2

Scanning Kelvin Probe

2.1 - Scanning Kelvin Probe – an overview

The Scanning Kelvin Probe (SKP) is a non-destructive and non-invasive technique that allows obtaining the chemical surface's potential of several different materials on a delimited sample area in a study.

Hankel and Pellet's work [1] in the middle nineteenth century was one of the basis of the work carried out in the late 1800s by Lord Kelvin, who named the SKP method, demonstrating the contact potential difference (CPD) between two electrically connected metals that could be measured[2]. The studies started with a plane parallel capacitance structure with two different metal electrodes. This method was developed in the early 1930s by W.A.Zisman, placing one electrode fixed while the other electrode oscillates at a frequency driven, which results also in a capacitor[2]. Over time improvements have been implemented to the method, for instance, the oscillating plate electrode was replaced by a steered needle, which improved the lateral resolution of the system[3].

In the 40s, Rosenfeld and Hostkings used cathode-ray oscillography as a detecting instrument, and Meyerhof and Miller obtained accurate results for smaller samples by amplifying the pulse from the condenser when moving and stopping the different plates nearby[1]. Later, many other followers made investigations and improvements throughout the 20th century, like T.A.Delchar and B.H.Blott who worked in the '60s on the rectification of the AC signal and stability of the system, and studied methods of vibrating the electrode for electrochemical methods by J.H. Parker/R.W. Warren, who introduced the SKP version[4][5].

In the '70s, N.A. Surplice, R. J. D'Arcy, P.P. Craig, and V. Radeka worked to improve the system in the modulated capacitance circuit[4][6]. At the beginning of the '80s, B. Ritty e et, improved a method that proved it was more advantageous to detect current rather than voltage as before[7].

The first time a Kelvin Probe System was controlled and associated with a computer was in the late 1980s, developed by J. Baczynski, leading to the commercial development of the Kelvin Probe. It also made it possible to improve it by reducing measurement errors from previous systems[4][8].

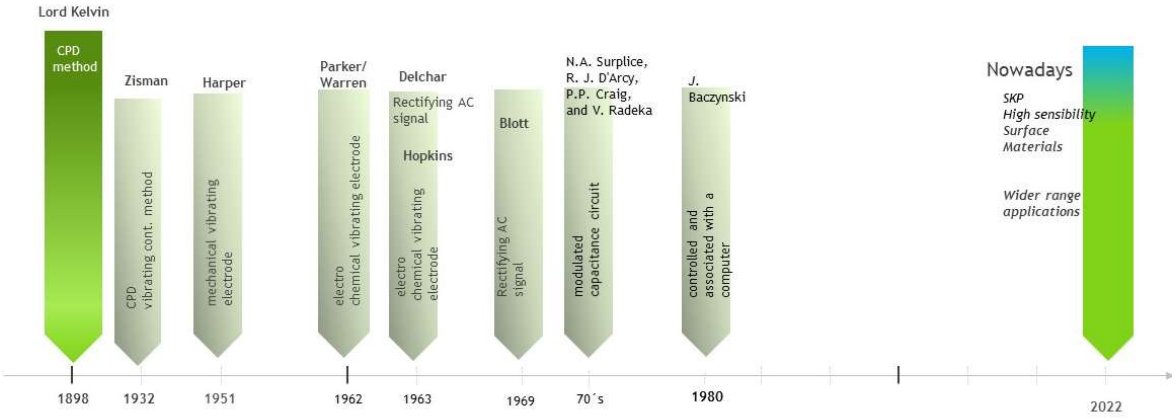

Figure 2. Kelvin method Line time

Although the scan tip-sample interaction techniques were developed over one hundred years ago, it has aroused interest in the last decades for surface science and improved the methods related to these techniques such as the SKP and Scanning probe microscopy families: Scanning tunneling microscopy, Atomic force microscopy, Electric force microscopy, Scanning near-field optical microscopy or Scanning electrochemical microscopy[9][10][11][12]. These techniques can be valuable to characterize and study the surface electrochemical properties of varied materials like metals, semiconductors, insulators, and even biological[12]. Within this perspective, making use of electrical surface phenomena can enable an improvement for various applications in the scientific and industrial fields: electric vehicles, mobile phones, laptops, micro and nano electronics, production, and energy storage [13].

The SKP method is used in several examples of studies of corrosion protection like steel marine corrosion protection with paint[14] and investigation of corrosion protection mechanism with nanoparticles[15]. In other fields is utilized for detecting oxide films on metals[16][17], studies on coatings in cooper-containing electrolytes[18] and investigation on hydrogen absorption in some metallic materials in hydrogen storage systems[19]. It is also suitable for studies: electronic properties for photovoltaic applications[20][21], semiconductor [22], materials interface [23][24], batteries [25], insulators [26],fingermark identification [27] and examining biomaterials being an alternative technique to the traditional methods [28][29].

The SKP is a noncontact tip vibrating mode that measures the work function difference between the surface sample in the study and the SKP's tip that is related to a characteristic of the surface condition potential difference (CPD). This technique allows the measurement of the surface's CPD distribution on a micrometrical scale nearby between the sample and the tip probe. Furthermore, the SKP technique is capable to acquire the topography of the surface's materials: maps the topography of the sample´s materials, which can also be applied to electrochemical studies and benefit from advances in several fields, such as batteries, photovoltaic cells, catalyzers, ferroelectrics, semiconductor's materials. It can be obtained through SKP Capacitive Height Measurement (CHM-SKP) or SKP Capacitive Tracking Measurement (CTM-SKP). Thus, besides getting

information on the material's topography, it can be a tool to study the changes in the surface of a material over time [30]. There are other different techniques to archive the sample's topography like Non-Contact Optical Surface Profiling (OSP), Scanning Electro-Chemical Microscopy (SECM), and intermittent contact Scanning Electrochemical Microscopy (ic-SECM)[31]. The SECM beyond topography is an electrochemical method that can study the current evolution, such as the Scanning Droplet Cell[31].

2.2 - SKP principles

The SKP derives from the AFM, a technique for scanning the materials' surface, which measures the interaction forces between the tip and the sample by contact or non-contact mode[11].

The SKP interactive elements are formed by the sample's surface and parallel reference metal tip separated by air. The tip is used in vibration mode and perpendicularly to the sample's surface. The tip's vibration and the variation of the distance cause an alternate current proportional to the CDP between the tip and the material's sample. When the sample and the probe tip are electrically connected, the current flow between the two different materials and their Fermi levels align at the vacuum level[32]. The result of this equilibrium is: a potential difference giving rise to a surface charge at the different materials and a formation of a parallel capacitor. Before connecting electrically the materials, the material with the lowest work function (WF) is charged more negatively than the material with the highest WF material (figure 3a). After connecting both materials (sample and tip), in figure 3b, the electrons will flow from the material with a lower value of work function to the material with the higher work function until their Fermi levels equalized (figure 3c). When balanced, the surface of the material with the lowest WF will be charged positively and the other material will be negatively (figure 3d).

To determine the point of CDP, an external electric potential (EEP) is applied between the probe and sample to null the surface's charge and the Fermi levels return to their original positions (figure 3e). The EEP is the equal value (with opposite sign) to the CDP and is applied between the probe and the sample to null the surface charge and consequently the electric field. The bias potential at which the surface charge nulls is equal to the work function difference between the probe and the material's sample.

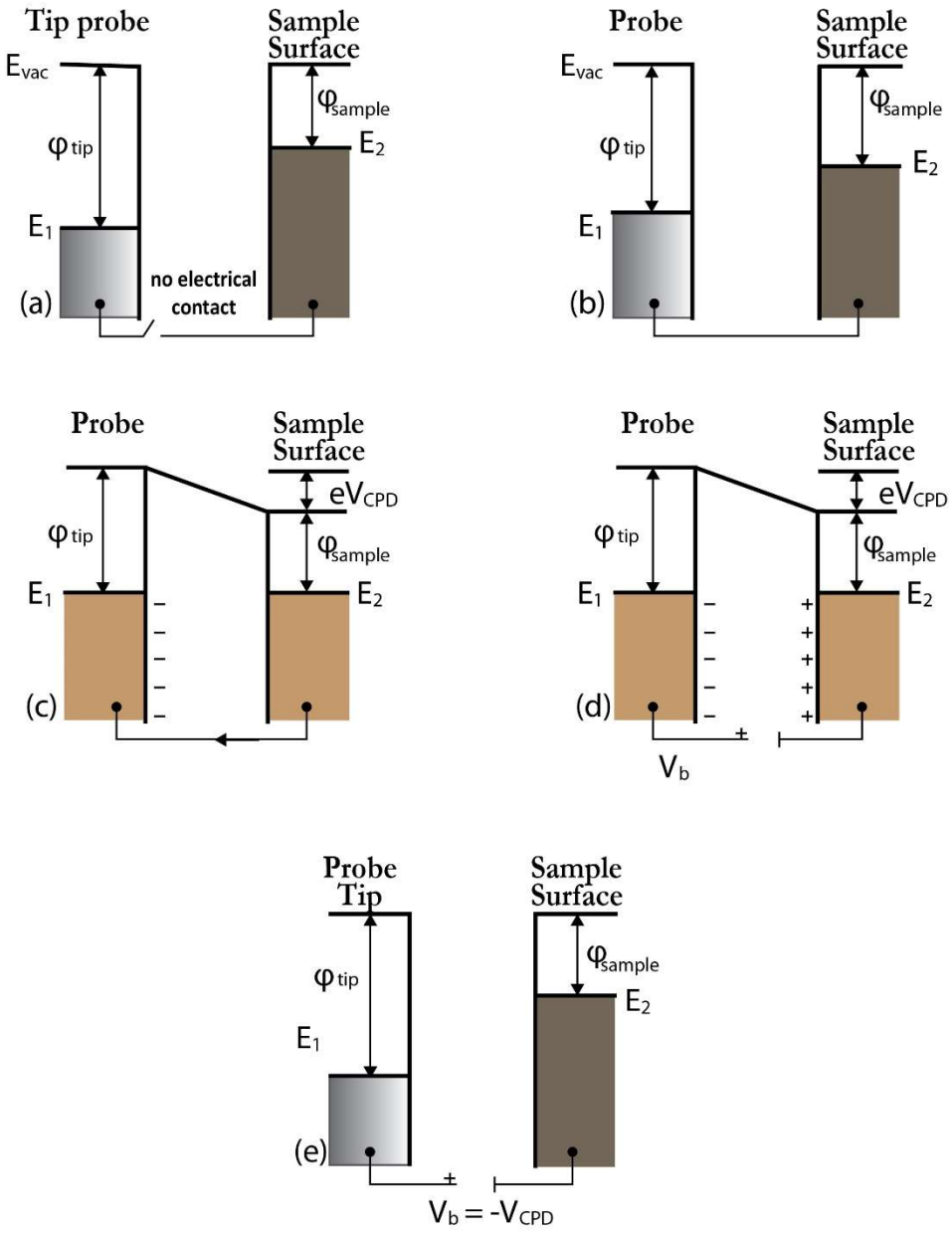

Figure 3. SKP principles

(a) when SKP and sample do not have an electrical connection each has its own distinct Fermi level; (b) the probe and sample are electrically connected; (c) leading to charge flow from sample to probe; rise to a surface charge between the probe and sample with a CPD V_{CPD}; (d) backing potential Vb, equal (but opposite in sign) to the contact potential difference is applied between the probe and the sample to null the surface charge and return the Fermi levels to their original positions (e). Figure adapted from Bio-Logic Science Instruments

Thus, if the tip's work function (φ_{tip}) is known, the work function of the sample (φ_{sample}) can be determined[20]:

$$V_{CPD} = \frac{\varphi_{tip} - \varphi_{sample}}{-e} \qquad (2.1)$$

and

$$\varphi_{sample} = [V_{CPD} \,.(e)] - \varphi_{tip} \quad (2.2)$$

Where *e* is the elemental electron charge.

The charge **Q** is given by the equation:

$$Q = C.V \quad (2.3)$$

where V is the potential between the two different materials. Considering the capacitance **C** is inversely proportional to the distance between the probe and the sample:

$$C = \varepsilon_0 \varepsilon_r (A/d) \quad (2.4)$$

Where,

ε_0 - permittivity of free space

ε_r - relative permittivity

A – active area of the material

d - distance between the SKP tip and sample

The probe is vibrated with a sinusoidal signal, so the other parameters (distance ***d*** of probe surfaces sample and capacitance **C** will have a correspondent sinusoidal characteristic, varying with time(t)[3][33]:

$$C(t) = \varepsilon_0 \varepsilon_r [\frac{A}{d(t)}] \quad (2.5)$$

$$d(t) = d_0 + K.sin(wt) \quad (2.6)$$

With,

d_0 – average distance between the SKP tip and sample

k- amplitude of the periodic signal

w – tip's vibration frequency

Therefore, the charge Q:

$$Q(t) = C(t).V \quad (2.7)$$

The induced AC current in the external circuit is,

$I(t) = dQ(t)/dt$

Thus, associated with the equation 2.5 to 2.7,

$$I(t) = A\varepsilon_0 \varepsilon_r \left[\frac{-Kw.cos(wt)}{(d0 + K.\sin(wt))^2}\right].V \quad (2.8)$$

and the V_{CPD} is compensated by an external voltage V_{EEP} source inserted into the circuit system,

$$I(t) = A\varepsilon_0\varepsilon_r\left[-\frac{Kwcos(wt)}{(d0 + K.\sin(wt))^2}\right].(V_{CPD} + V_{EEP}) \quad (2.9)$$

When,

$V_{CPD} = -V_{EEP}$ → $I(t)$ is null (figure3.e)

The SKP output value of the CDP amplitude is a dc result. The AC signal is demodulated by the Lock-in Amplifier (LIA) and turned into a dc signal. The LIA is responsible to demodulates the ac signal into a dc output signal[34]. It is done by multiplying the ac output by a demodulation ac signal (with different phases) and results in a final signal. The phase difference between these two signals is minimized to maximize the final dc output response. After that, the signal will be smoothed by a filter (figure 4). These steps are controlled by the SKP unit control[34]:

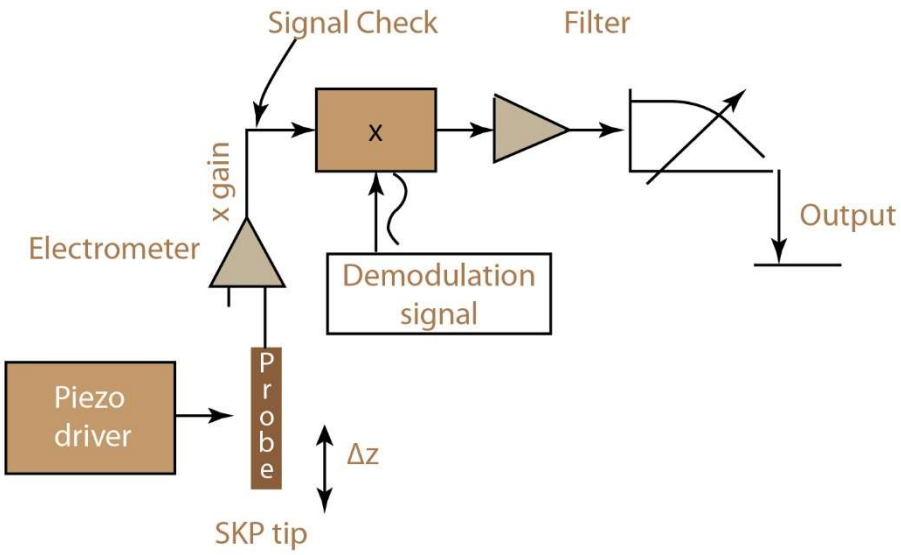

Figure 4. Steps of AC signal's demodulation (adapted from Biologic Instruments)

In figure 5 is described the SKP M470 electrochemical workstation and in figure 6 is presented the block diagram of SKP M470:

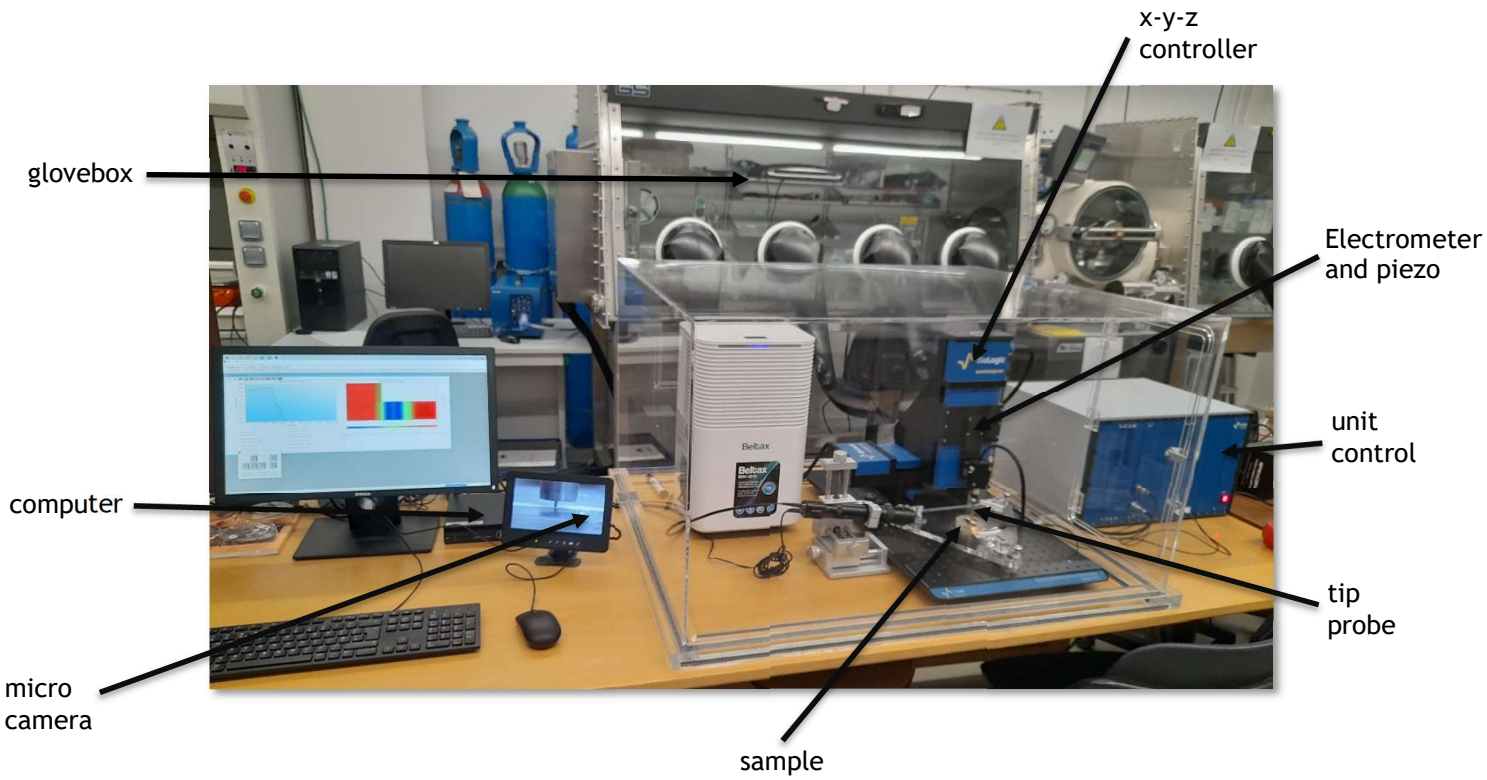

Figure 5. M470-SKP electrochemical workstation

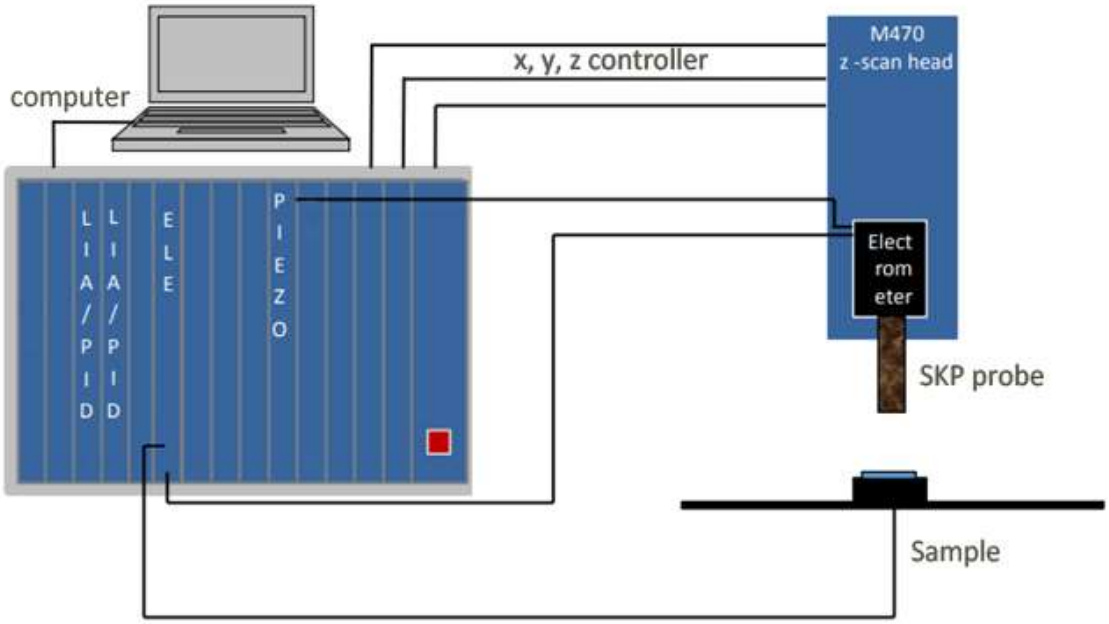

Figure 6. SKP block diagram

2.3 - Work Function

The materials can be distributed in three major groups according to conductivity: conductors, semiconductors, and insulators.

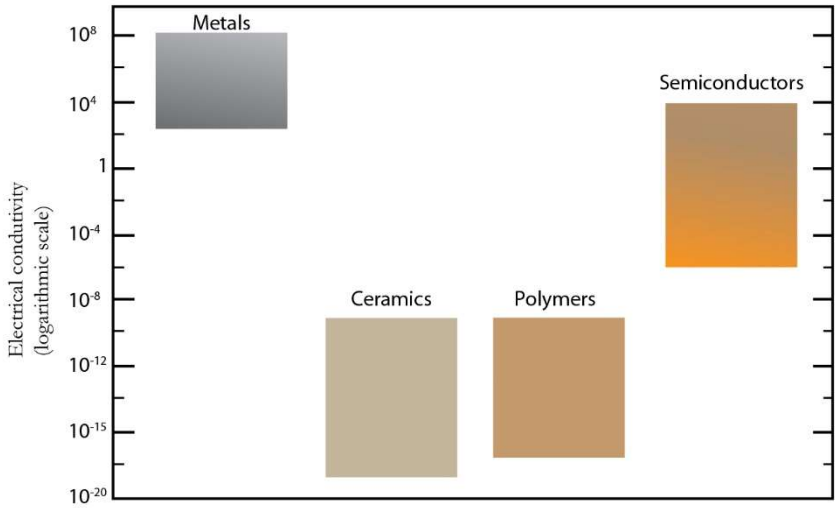

Figure 7.Electrical conductivity of various materials

These materials differ in their bulk and surface structure which is related to energy levels. Between the valence and the conducting bands is the forbidden energy gap (Eg) that determines the electric conduction. In metals, the two bands are over each other, which means it forms a "continuous" band for the two energy levels with valence and conducting properties. The conductivity increases when the purity of metal increases and decreases with temperature.

For semiconductors, the valence band is the lower energy level and is filled with electrons. The conduction band is a higher energy level where the electrons can reach it if receive energy higher than Eg. The difference value of the energy between the conductive and valence level is considered a small value, Eg<3eV (figure 8). Low energy is needed to excite the electrons to be able to jump from the valence band to the empty conduction band. Thus, the semiconductors have some conduction properties which increase with temperature. With the temperature rising the semiconductor's resistivity decreases.

The organization of energy on insulators is similar to the semiconductors but in this case, the Eg between the two energy levels is quite large, Eg >3eV, without any chance to be conductive [35] (figure 8).

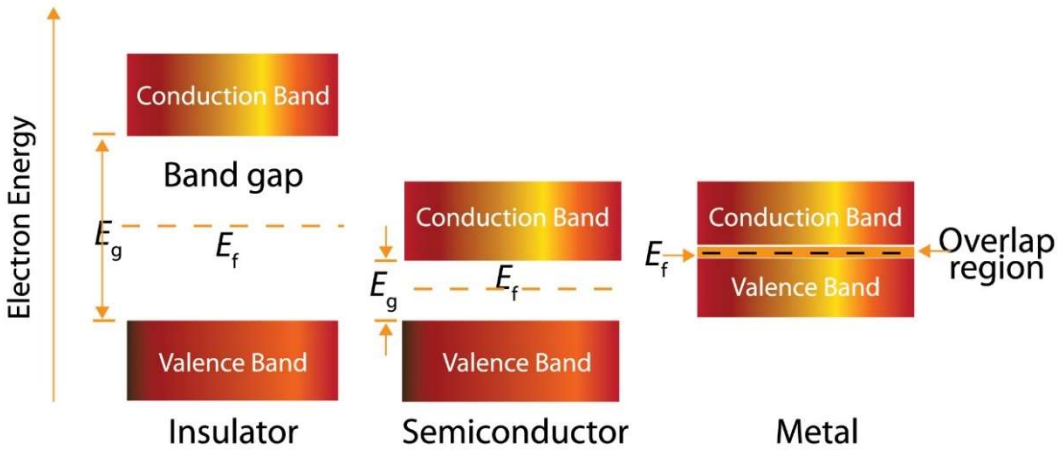

Figure 8. Valence and conduction bands for insulators, semiconductors and metals

The WF, Fermi level, vacuum level, ionization energy, and electron affinity are important characteristics that determine the conductive properties of a material.

The WF corresponds to the minimum energy required to remove an electron from the surface of the material to the vacuum level. The WF´s value is greatly affected by the condition of the surface and by several variables like: the presence of oxide layers, absorbents, contaminants, evaporated layers, surface roughness, surface and bulk contamination, illumination and catalysis[36]. These can modify substantially the electrochemical surface´s characteristics. Consequently, alter the energy condition that an electron needs to leave the sample.

For semiconductors, the surface´s properties and WF also are significant parameters[32]. The semiconductors are characterized by having an energy gap (Eg) between the valence and conductive band. Between them can be found the Fermi level energy. In semiconductors, the analyses below considered the probability function of quantum distribution of Fermi-Dirac (f_{FD}) gives the probability of occupation by an electron in an energy level [37][38],

$$f_{FD}(E) = 1/[e^{(E-EF)/kT} + 1] \quad (2.10)$$

Where,

EF - Fermi level

E- energy

K – Boltzmann´s constant

T – temperature

For the pure (or intrinsic) semiconductors, when energy (E) is equal to Fermi level (EF) and the temperature (T) is different from zero Kelvin, EF lies probability in the middle of the valence and

conductive bands. This means that with E=EF state has a 50% of probability being occupied by electrons. When f_{FD} is closer to zero is more likely that the energy level is unoccupied. On the other hand, if it is near 1, it is nearer to being full.

Thus, the Fermi level of the semiconductors is located theoretically inside of the band gap which means the work function is different from the ionization energy´s value (figure 9) which does not happen with the metals whose values are equal (figure 10).

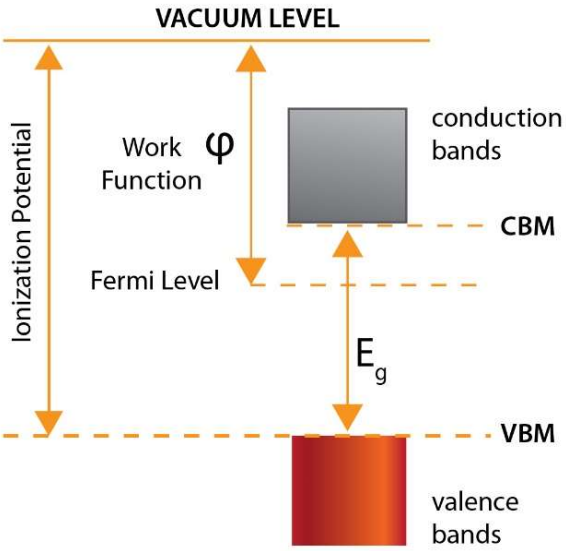

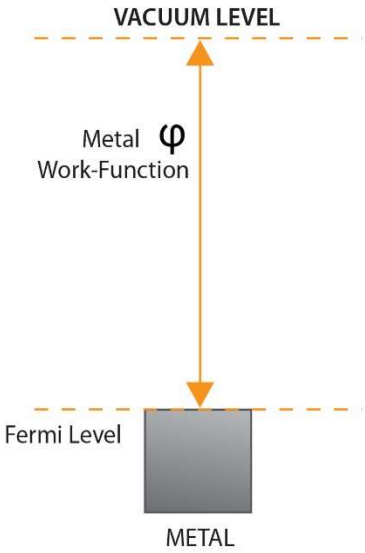

Figure 9. Work function: semi-conductor

Figure 10. Work function: metals

Adding small quantities of dopants (impurities) to pure semiconductors (like silicon or Germanium) it is obtained extrinsic semiconductors: P-type and N-type. P-type is obtained by adding excess positively charged holes with a very small amount of impurities (elements of the 13th group of the periodic table like boron and aluminium) to the pure semiconductors. Thus, with dopation the semiconductor has a new energy level (acceptor of electrons) near to valence band and consequently the EF. On the other hand N-types are obtained by adding a very small amount of elements from the 15th group of the periodic table, like arsenic and phosphorous, pentavalents, with an excess of electrons. Hence, the new energy level (donor level) is displaced near to conductive band (receptive to gain electrons) and also to the EF.

2.4 - CTM and CHM topography measurements

CTM and CHM developed from capacitance phenomena that arise between the tip and the sample. In this work, it was used the CTM technique to scan the sample´s surfaces. Most of the samples were characterized by non-flat surfaces and with many irregularities, which could be in most areas highly accentuated.

CTM is a height tracking technique that maintains a constant distance between the SKP probe and the sample and therefore, "follows" the surface without losing proximity information of the sample´s surface (figure 11).

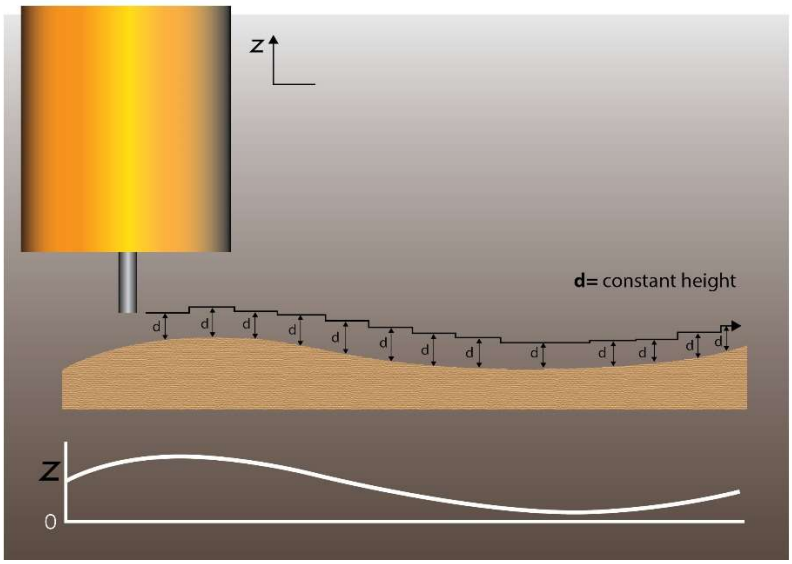

Figure 9. CTM measurement

Z-position changes to maintain the set distance between the probe tip and the sample (Figure adapted from Bio-Logic Science Instruments)

At CHM, the Z-position setting does not change regardless of the irregularities of the sample, it uses a fixed height and measures scans from the initial Z-position up to each different area of the sample (figure 12).

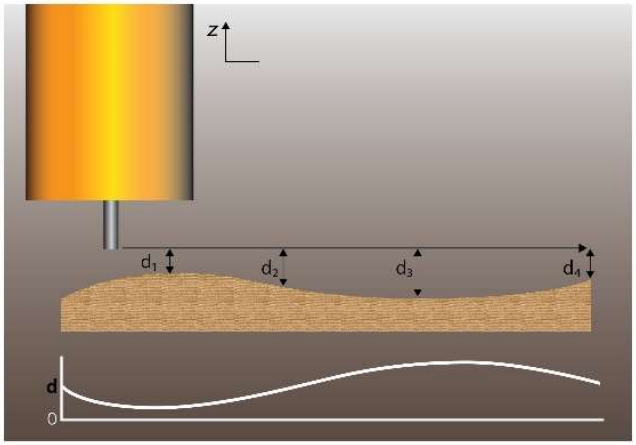

Figure 10. CHM measurement

As the probe scans from left to right, the distance between the probe and the sample increases, and the effect is shown in the graph in the lower half of the image- (Figure adapted from Bio-Logic Science Instruments)

CTM is the most accurate way to obtain the sample topology, specially if the sample has many irregularities. For samples that have a surface with insignificant irregularities, it can use the CHM. This technique is faster in time than CTM but loses accuracy. Therefore, in this specific work the option used was the CTM method.

Chapter 3

Characterization: Methods and materials

3.1 - Materials

3.1.1. Zinc oxide

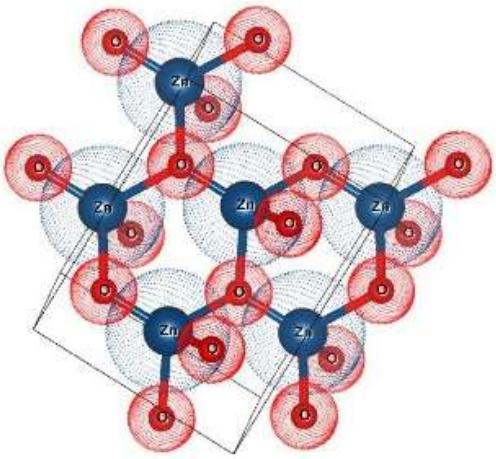

Figure 11. Wurtzita structure crystial ZnO (*Vestas* Software)

Zinc oxide is a unique and very useful material to actual scientific and socio-economic society. It is used in vastly different fields such as electronics, optoelectronics, electrical devices, wave devices, storage batteries, solar cells, sensors, biomedical and environmental treatments. Also participates in plastics, paints, rubber products, pharmaceuticals, soaps, cosmetics, construction materials, textiles, food packaging and antibacterial[39].

The fast development of technology led to a growing increase in optoelectronic and electronic devices into the nanoscale. This oxide has singular characteristics: semiconducting, pyroelectric and piezoelectric properties, due to its crystal Wurtzite structure, noncentral symmetry and polar surfaces, which are relevant for these applications [40]. Hence, ZnO is relevant in materials, being suitable for electronics, photonics, n-type intrinsic semiconductors and nanotechnology with a wide direct band gap of 3.37 eV and a high exciting binding energy (60 meV) at room temperature [41]. ZnO band gap is large (near of limits of the conductors) and has a wide exciting binding energy, exhibiting near-ultraviolet emission. These characteristics make it special in semiconductors. It has an important property for transparent conductivity: the conductivity of ZnO on thin films can be significantly improved by doping atoms, implying that ZnO based transparent conductive films are a valid option for others more expensive, such as Indium Tin Oxide (ITO) film, the leading transparent conductive oxide films [42]. There are also other studies with very promising results in thin film transistors (TFTs), due to their superior electrical performance and good optical transmittance

compared to conventional a-Si:H and organic materials. Concerning studies on their high mobility, good uniformity and low processing temperatures have also been extended to other areas such as panel system (SOP), pixel memory and transparent memory displays.[43].

ZnO works as a dielectric that does not have a flow of charge through it but permits an electrostatic field and store charge. One of the dielectric properties of the material is the constant *k* which determines the charge storage capability of the material. The high *k* materials are used as gate dielectrics in MOS transistors, memory cells, capacitors and super capacitors. ZnO, such as other elements from transition metal oxides, has a high dielectric constant (8,66)[44] which placed it **in** a prominente position in the microelectronics world and the capacitors for energy storage [45].

ZnO is also used in heterostructures applications such as graphene/ZnO[46], SnO_2/ZnO [48], GaN/ZnO [49], NiO/ZnO [50]–[52], Au/ZnO[53] or Cu_2O/ZnO [54].

Physical properties ZnO: 99.99 %, powder with diameters < 74 μm from Alfa Aesar, is used as the dielectric material. Stored and manipulated in the glovebox (GS Systemtechnik GmbH) with argon atmosphere controlled, H_20<1ppm, O_2<1ppm and 0.8 *bar*.

3.1.2. Metal elements: Copper, aluminium and zinc

The chemical elements aluminium, zinc and copper belong to the metal group and are in a solid state at room temperature. In the experiments, copper (Cu), aluminium(Al) and zinc (Zn) were studied as metal electrodes, individually and as part of the cells in study, as we will see in the following chapters. Below, these elements are presented.

3.1.2.1. Copper (Cu)

Cu metal commercial; physical properties: It has an electron affinity of 1.228eV, ionization of 7.68eV, work function of 4.48–4.98eV[55], electrical resistivity of 16.8 nΩ.m, and thermal conductivity of 401 W/(m·K). Copper oxidation states: Cu^+ and Cu^{2+}. As a metal solid state has a reddish color; with a density of 8.92 g/cm^3, a melting point of 1084.62ºC, and a boiling point of 2562ºC [56][39][57]. At room temperature, copper is presented in the solid state, belonging to group 11 of the periodic table, the transition metals group, by IUPAC[58]. The crystal structure for copper metal has a cubic geometry, face-centered cubic. The atoms are located at each of the corners and the centers of all the cube faces [57].

Copper is a preponderant element in several fields from current technology to the pharmaceutical medical area. It is used in several branches such as the electrical industry, electronics technology, batteries, building construction, vehicle components, metals alloy industry, chemicals, health products, jewellery, coins, and domestic utensils[59][60]. Copper has impressive electrical and thermal conductivity (marginally surpassed by silver), being two of its main applications. It also has

high ductility, malleability as well as good corrosion resistance[59][61]. In nature it can occur natively but, essentially, is found in many minerals such as cuprite, malachite, azurite, chalcopyrite, and bornite[39].

Due to its properties, copper is one of the most recycled metals with good quality[60].

3.1.2.2. Aluminium (Al)

Al metal commercial; Physical properties: It has an electron affinity of 0.441 eV, ionization of 5.986 eV, work function 4.06–4.26 eV[55], electrical resistivity of 26.5 nΩ.m, and thermal conductivity of 247 W/(m·K). Aluminium has an oxidation state: Al^{3+}. As a metal state has a silver color, with a density of 2.6989 g/cm^3, a melting point of 660.2°C, and a boiling point of 2480°C [39])[62][63]. At room temperature, copper is presented in the solid state, belonging to group 13 of the periodic table, the post-transition group by IUPAC[58]. The crystal structure for copper metal has a cubic geometry, face-centered cubic. The atoms are located at each of the corners and the centers of all the cube faces[41][63].

Aluminium is the most abundant metal in nature but never it found on its own, due to its nature of easy chemically bonding with other materials. In order to obtain it, it must suffer an industrial refining process. Pure aluminium is a soft light metal, with a silver appearance, is easily molded or melted, with high thermal conductivity and has very good corrosion resistance. It is non-magnetic, malleability and ductility metal[40][47][50]. The natural solid state is solid at room temperature. It is used in a wide application in industry, transports, construction and buildings, machinery, domestic and decoration utensils. Although its electrical conductivity is only about 60% that of copper, it is used in electrical transmission lines because of its lightweight [40][46][50]. It easily settles alloys with small amounts of copper, magnesium, silicon, manganese, tin and zinc [51].

3.1.2.3. Zinc (Zn)

Zn metal commercial; physical properties: It has an electron affinity of 1.228eV, ionization of 7.68eV, work function 3.63–4.9 eV[55], electrical resistivity of 59.16 nΩ.m and thermal conductivity of 113 W/(m·K). Copper has two oxidation states: Zn^{2+}. As a metal state it resembles a bluish-silver colour, with a density of 7.14 g/cm3, a melting point of 419.53ºC, and a boiling point of 907ºC [39][62][64]. At room temperature, copper is presented in the solid state, belonging to group 12 of the periodic table, the transition metals group by IUPAC[58]. The crystal structure for copper metal is Hexagonal Close-Packed.

Zinc is an essential element for human beings and animals' health. Zinc is extensively used to prevent the corrosion of other metals, such as iron, by galvanization. It is considered an important industrial method, being one of the most cost-effective. Large quantities of zinc are used to produce

die castings, widely applied by the automotive, electrical, and hardware industries [40][52]. It has other applications in household appliances, tools and toys, fittings, rubber, fertilizers, animal feeds and also used in pharmaceuticals and cosmetics. It is soft, malleable and fair conductor of electricity. Zinc metal is employed to form numerous alloys with other metals: brass, nickel silver, typewriter metal, commercial bronze, spring brass, german silver, soft solder, and aluminum solder are some of the more important alloys[40][52].

3.1.2.4. Cork

Commercial Cork foil, 1,7mm thick.

Cork is a natural material produced from the phellogen tissue of Quercus suber L., which grows in the Mediterranean basin. Cork is the outer bark of the cork´s tree, constituted by empty cells, that acts as an extraordinary natural protective barrier against humidity, gases and fire[65]. Cork is most known in the wine world as bottle stoppers. Nowadays, it is used in vast applications fields like construction, fashion industries, vehicles and the aerospace industry. The scope and vertability of this material make it an excellent reason for study. Herein, surface cork was studied itself electrochemically and, in the future, can be combined with other materials[66]. Is a promising and innovative material for usage in structural batteries based on solid ferroelectric electrolytes[67].

3.1.3. Cells: ZnO cells and cork's shell

The ZnO cells were assembled with a pair of different parallelepiped metal pieces' electrodes (copper/aluminium) and (copper/Zinc), fixed on epoxy support, separated by a design gap between them. The cell's gap was filled with the ZnO. The average dimensions of the cell´s materials used in the experiments:

1) Cell "1": Cu/ZnO/Al - Cu with (10 x 22 x 4.7) mm^3; ZnO with (4.5 x 22 x 4.7) mm^3; Al with (10 x 22 x 4.7) mm^3;

2) Cell "2": Cu/ZnO/Zn - Cu with (10 $\times$ 20 $\times$ 6.2) mm^3; ZnO with (5 $\times$ 20 $\times$ 6.2) mm^3; Zn with (11 $\times$ 20 $\times$ 6.2) mm^3;

The cork cell was assembled with copper tape, and fixed on a glass support.

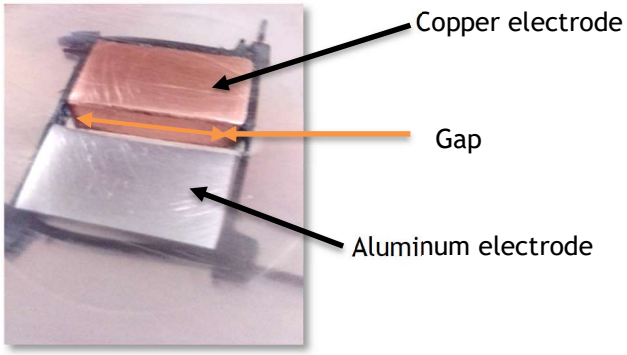

Figure 12. The perspective of cell copper/gap for sample/aluminum with empty gap

3.2 - Methods

3.2.1. Metals preparation

The metals are sanded and polished before any experimental action. Afterwards, the metal is thoroughly cleaned and dried.

3.2.2. Cell preparation

Before beginning the calibration procedures on SKP, the cell is prepared in the following steps: 1) sand and polish the electrodes; 2) thoroughly clean the particles' residues and fully dry and preserve it in the glovebox; afterwards, the cell is filled with the sample in the gap, inside the glovebox, tightly compressed and levelled with the electrodes.

3.2.3. SKP

In this work, it was used the SKP method, which is a highly sensitive technique that characterizes and studies the surface's properties. The experiments were performed with a Biologic SKP – M470 to measure changes in sample function related to surface state changes correlated to CDP. All SKP potentials are given versus the standard hydrogen electrode (SHE) (figure 41). The tip scan in the X direction, from the left to the right, and in the Y direction with two or more controlled runs, vanishing the defined area of the different materials of the cells covering the electrode, firstly, then the oxide and the other electrode. In the case of the cork cell, first the electrode and then the cork. The Z line direction is established as soon as the calibration step is executed.

Before running the SKP measurement, the CTM control topologic measurement is done. A vibrating capacitor tip is used to measure the local work function difference between the sample and the tip. It results in a potential difference giving rise to a surface charge at the different materials and the formation of a capacitor. SKP measurements obtain: 1) work function of the materials; 2) variations

in the work function of the sample at the surface; 3) CDP; 4) material topography; 5) capacitance with a non-destructive method,6) electrochemical study of the materials and 7) a non-invasive experiments technique.

3.2.4. SKP measurements

All SKP measurements were performed through a Biologic SKP-M470 with an SKP tip U-SKP370/1 (figure 15) made of tungsten wire with a 500 µm diameter [68]. The distance chosen for this study, between the probe tip and the sample, was 100 µm with CTM mode, appropriated for our samples, and SKP monitored through a micro camera scale. The calibration is done by adjusting the distance between the probe tip and levelled sample, having selected the correct phase angle of the amplifier. Before the measurements, the calibration was made concerning each kind of metal electrode: copper, aluminum, or zinc in independent experiences, depending on the case under study.

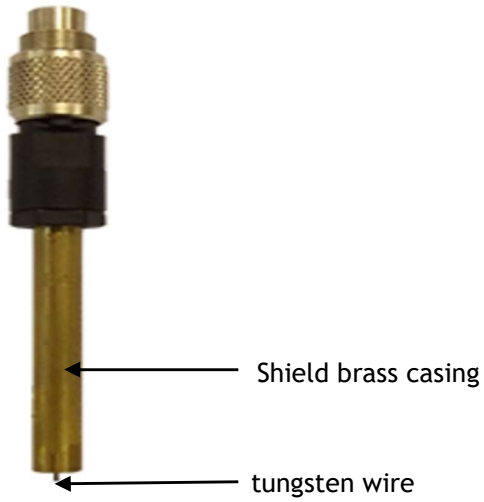

Figure 13. Probe SKP U-SKP370/1

3.2.5. Electrochemical Impedance Spectroscopy (EIS)

In the EIS technique, GAMRY (GAMRY1000) equipment imposes a small amplitude AC signal to the terminals of the cell. The AC voltage and current response of the sample cell allow determining the impedance (resistive, capacitive, and inductive characteristics) of the cells and equivalent circuits related to their components at controlled frequencies. This technique complements the study of the surface phenomenon of the cells. EIS was performed in the frequency range of 1 MHz to 0.1 Hz with an amplitude signal of 10 mV, determining the resistance and capacitance of our cells.

Chapter 4

Results and discussion

4.1 - Metal elements study: Copper, aluminium and zinc

Here is presented the study for metallic elements that are commonly used in various applications, specifically in batteries. The study was conducted using the SKP method with CTM (figure 16) presents the CTM topography map of the metal Cu. The material does not show great roughness or accentuated discrepancies.

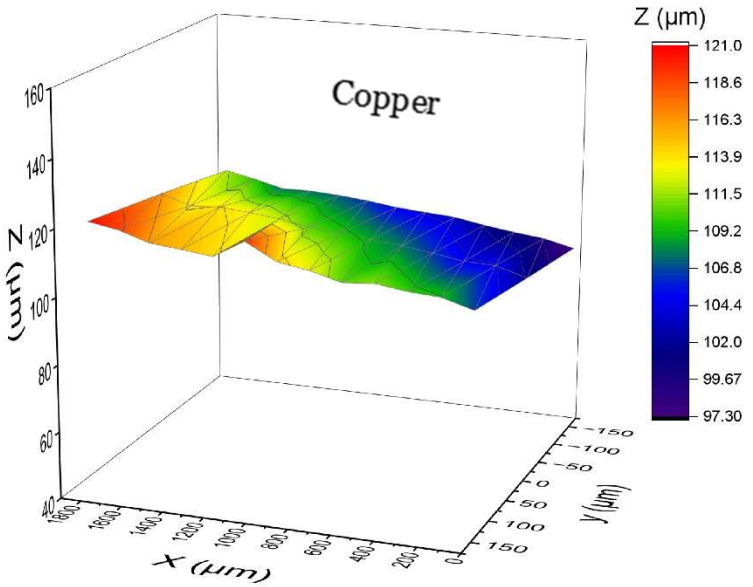

Figure 14. CTM topography of the Cu metal

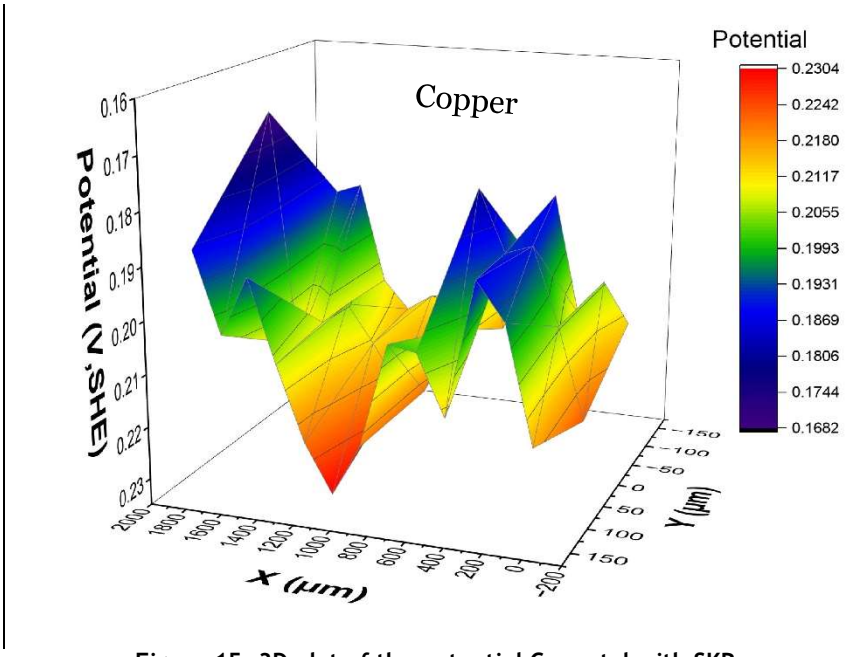

Figure 15. 3D plot of the potential Cu metal with SKP

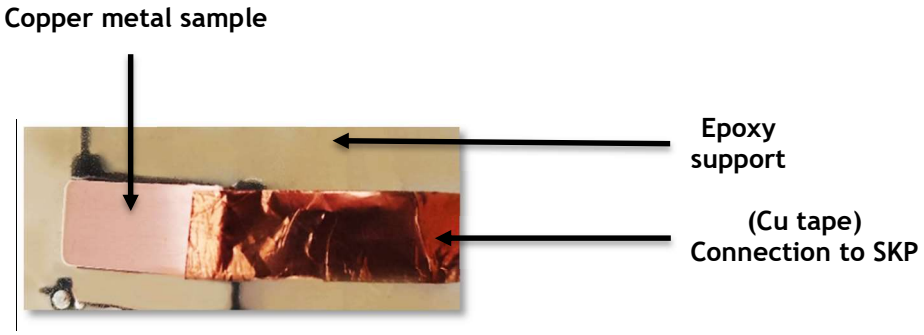

Figure 16. Cu metal sample on epoxy support

With SKP measurements of the Cu metal (figure 17) it was obtained the result CDP of the surface of the metal. It varies from 0.23 to 0.18 V. The tests carried out with the CTM/SKP make it possible to study the nature, purity, roughness, flatness and uniformity of the material. In figure 18 Cu's sample is presented after preparation and ready to start the experiment.

In figures 20 and 21, is presented the SKP of the aluminium and zinc metal. In the case of aluminium has values from 1.2 to 1.73 V, which is approximate to the electrochemical scale SHE.

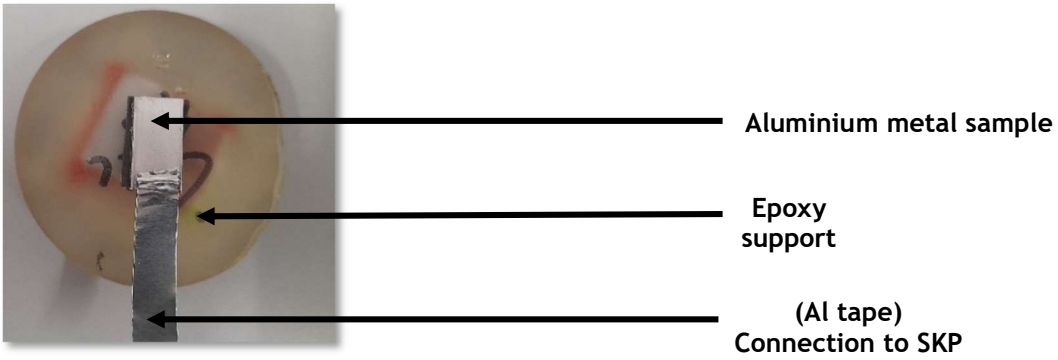

Figure 17. Al metal sample on epoxy support

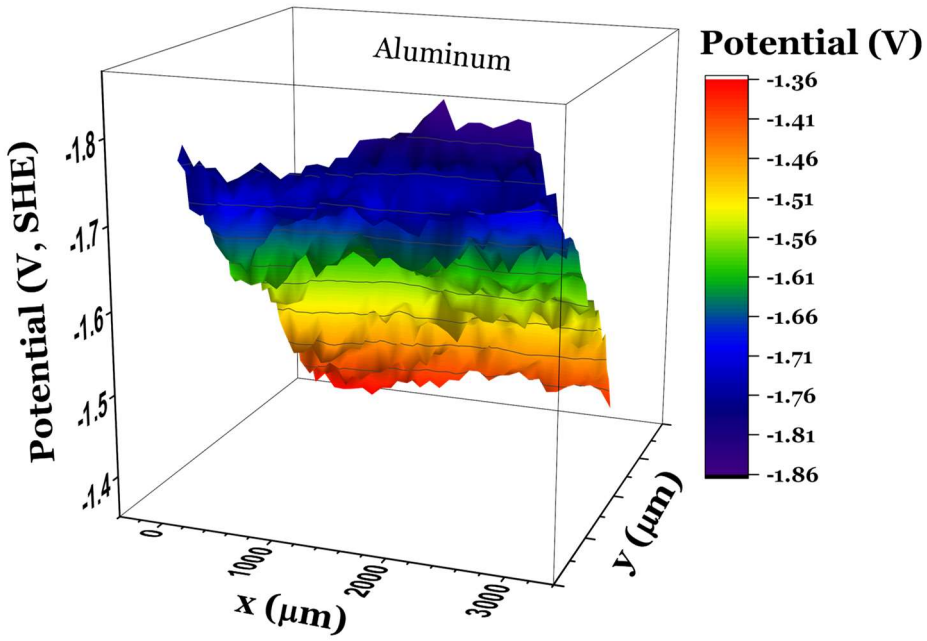

Figure 18. 3D plot of the potential Al metal with SKP

In the case of Zinc (figure 21), it was obtained values ranging from 0.68 to 1.1 V, which can be considered within the standard values of the SHE table.

Considering the mean values of the measurements, all of them are found in the electrochemical standard values of SHE.

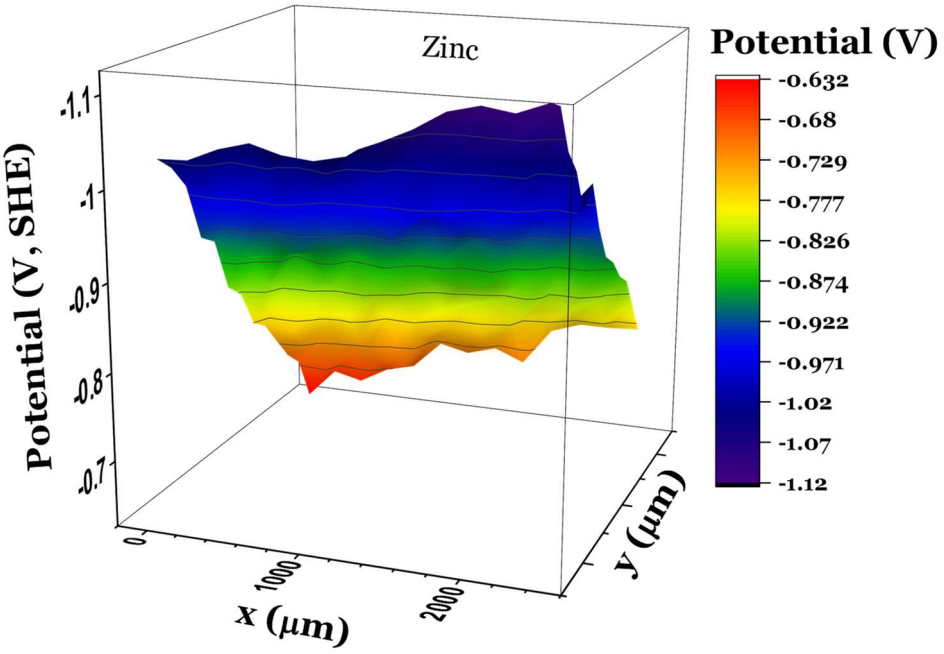

Figure 19. 3D plot of the potential Zn metal with SKP

Figure 20. Zn metal sample

4.2 - Single heterojunctions study

The study of the heterojunctions of two metals was carried out for the pairs of metals Cu/Al, Cu/Zn and Al/Zn. These metals are used as electrodes and current collectors in batteries. Each pair of metals are air-seed, not in contact. An experiment was also made with two different materials, metal and not metal: Cu and cork.

In the experiments Cu/Al and Cu/Zn, the connection to the SKP was made by copper electrode through copper tape. In the Al/Zn the connection was made through aluminium.

4.2.1. Copper and aluminium heterojunction

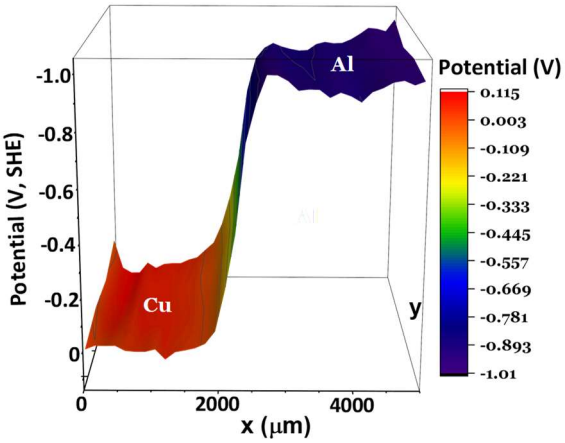

Figure 21. 3D plot of the Potential vs surface of the Cu/Al cell with SKP

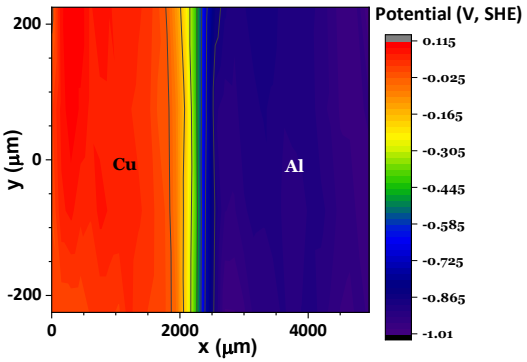

Figure 22. 2D plot of the potential of the Cu/Al cell's obtained with SKP.

In these experiments (figures 23 and 24) the two metals are separated by air, as if it was a potential well. The copper was used to establish the connection to the SKP electrode station and presented a potential average surface of 0.19 V. Al had a potential average surface of approximately –1V. These are values that commit the results when SKP measurement was performed with metals alone. As can be seen the Al metal is more "negative" than Cu metal in agreement with the SHE scale (figure 41).

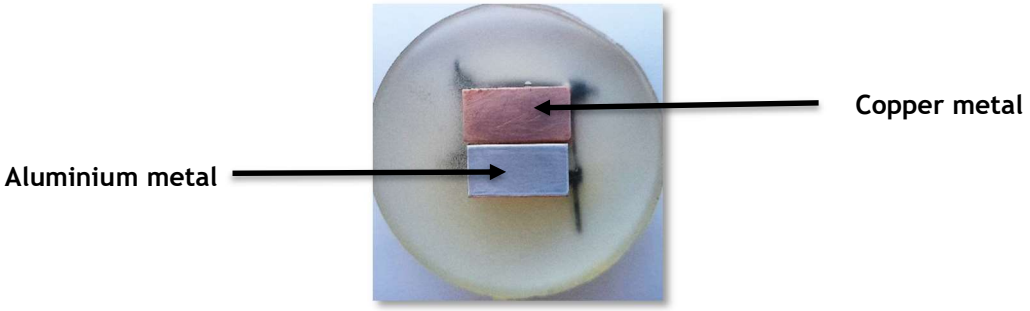

Figure 23. Heterojunction Cu/Al

4.2.2. Copper and zinc heterojunction

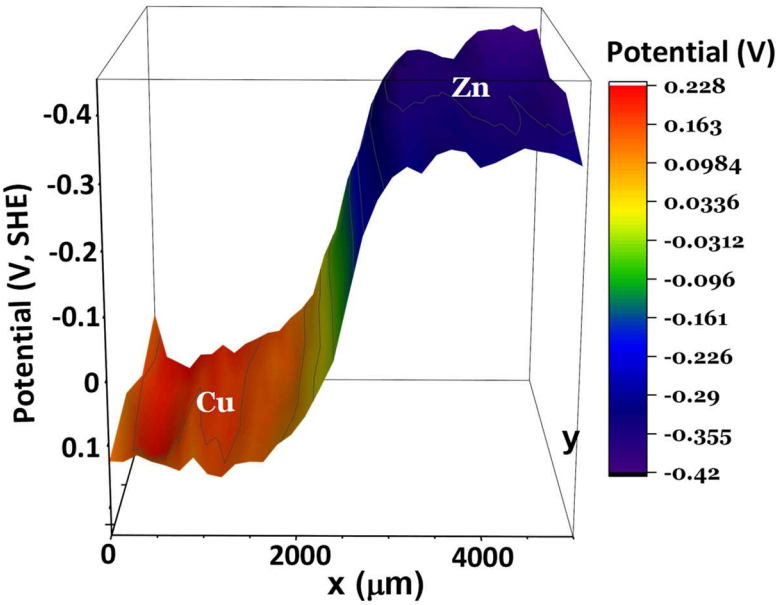

Figure 24. 3D plot of the Potential vs Surface of the Cu/Zn cell with SKP

As can be seen the Cu metal is more "positive" than Zn metal in line with the SHE scale (figure 41).

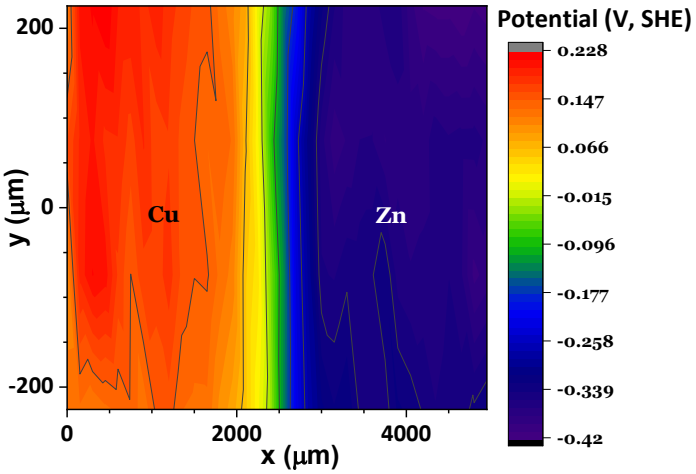

Figure 25. 2D plot of the potential of the Cu/Zn cell's obtained with SKP

In the experiments with the metal pair Cu/Zn (figures 26 and 27), the Cu was used to establish the connection to the SKP electrode station and presented a potential average surface of 0.20 V. Zn shows a potential average surface around – 0.4 V. This value is below compared to that measured alone, it may have been because it suffered oxidation (material that easily oxidizes after cleaning) or calibration differences. A slight difference in calibration caused by environmental or operational reasons may also change the results.

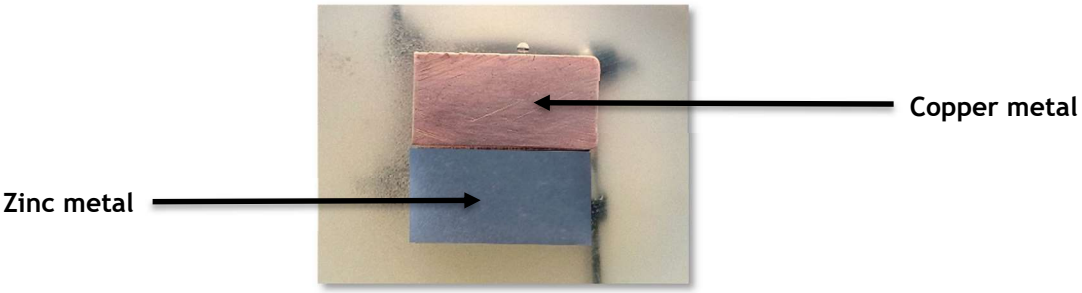

Figure 26. Heterojunction Cu/Zn

4.2.3. Zinc and aluminium heterojunction

In experiments with metal pair Al/Zn (figures 29-34), the aluminium was used to establish the connection to the SKP electrode station and presented a potential average surface of 1.2V, value that confirms the previous results. Two experiences were carried out, CTM (black line) e SKP (red line) that verified that the values obtained for Al and Zn were very close. The average value of Zn was 0.92V, similar to the value obtained when measured alone (figure 21).

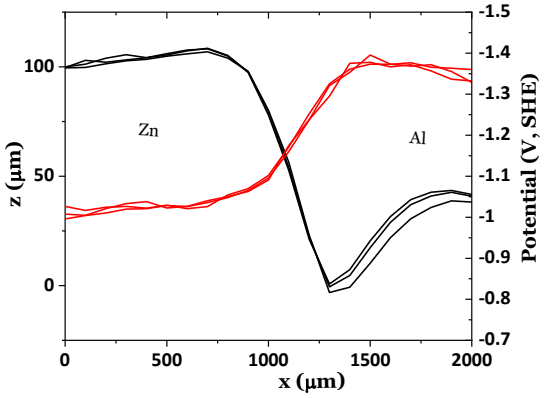

Figure 27. CTM and SKP experiments of the cell Al/Zn metal pair; Potential (V,SHE)

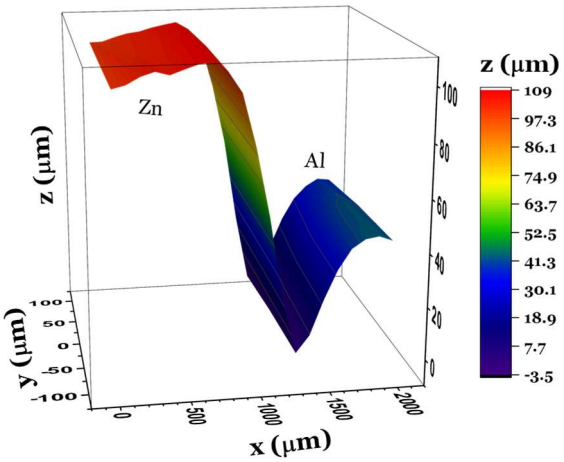

Figure 28. CTM topography of the Al/Zn metal pair; 1st experiment

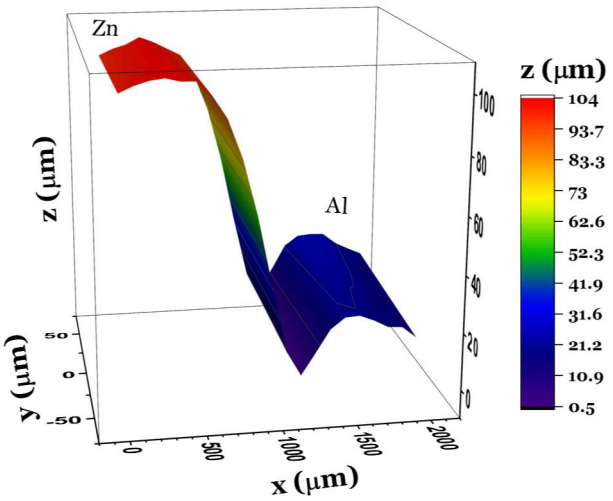

Figure 29. CTM topography of the Al/Zn metal pair; 2nd experiment

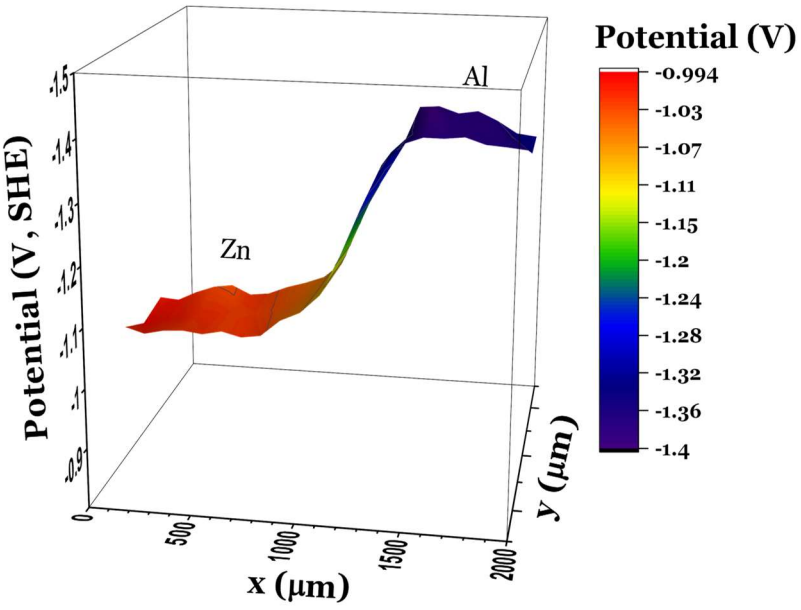

Figure 30. 3D plot of the Potential *vs* surface of the Al/Zn cell with SKP; 1st experiment

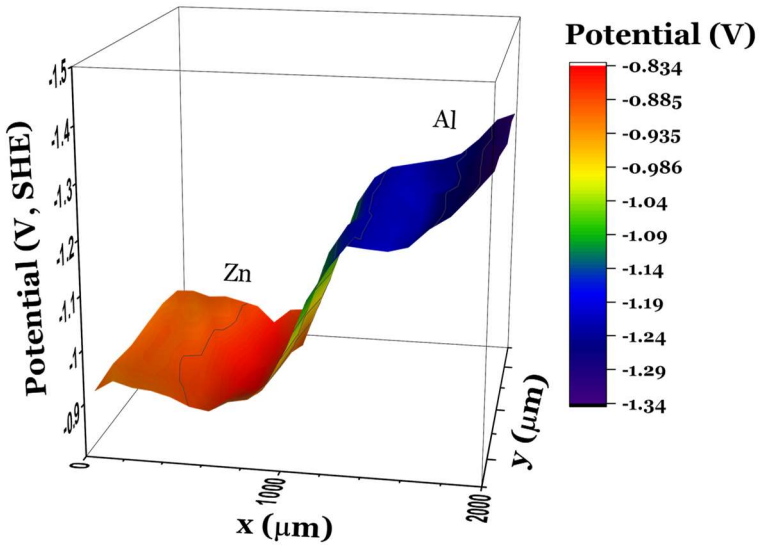

Figure 31. 3D plot of the Potential vs surface of the Al/Zn cell with SKP; 2nd experiment

As can be seen the Al metal is more “negative” than Zn metal according to the SHE scale (figure 41).

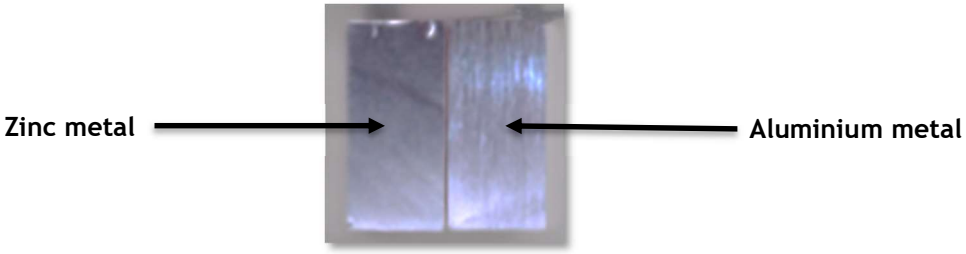

Figure 32. Heterojunction Al/Zn

4.2.4. Copper and cork heterojunction

Cork is a lightweight material considered a thermal and hydrophobic insulator in several different areas such as wine and aerospace applications. It can be a material of interest to energy storage equipment.

Two experiments (figures 36-38) were performed in different areas of the sample, with cork connected to the SKP by a copper tape and calibration made on copper. The results are in agreement with each other (figures 36 and 38). Cork showed to have a more positive potential than copper, with an average difference between the two of 0.15 V.

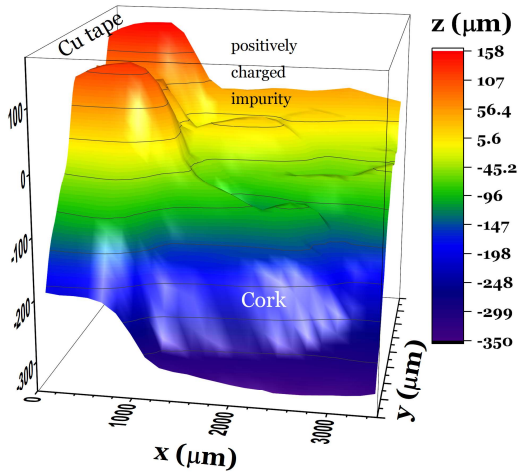

Figure 33. CTM topography of the Cork/ Cu tape; 1st experiment

In the first experiment, the SKP result showed that cork has a potential that can be considered relatively uniform, but revealed a positive high peak. This peak can certainly be an impurity due to the treatment which it is subjected to cork or something that has encrusted in transports or during its development in nature.

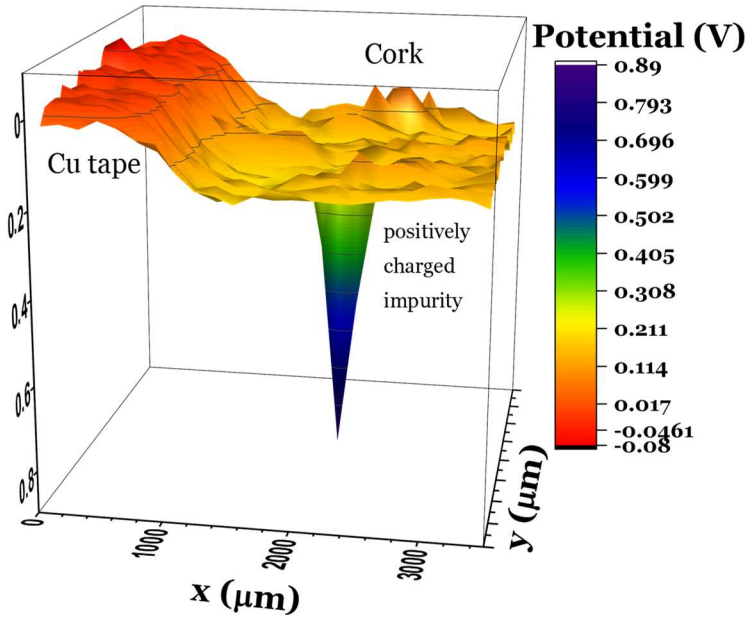

Figure 34. 3D plot of the Potential vs Surface of the Cork/Cu tape with SKP; 1st experiment

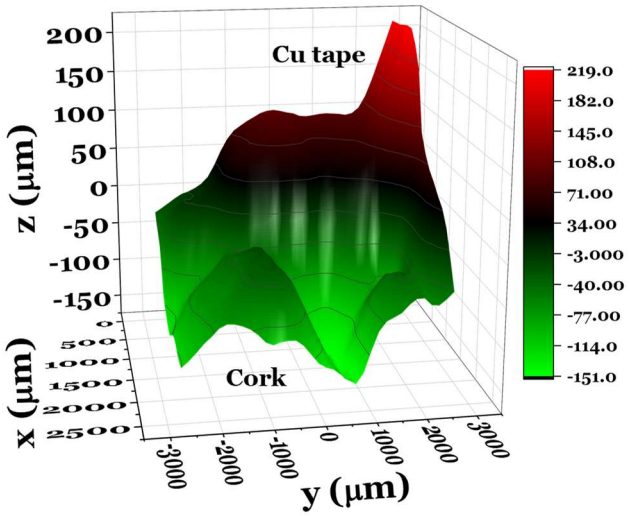

Figure 35. CTM topography of the Cork/ Cu tape; 2nd experiment

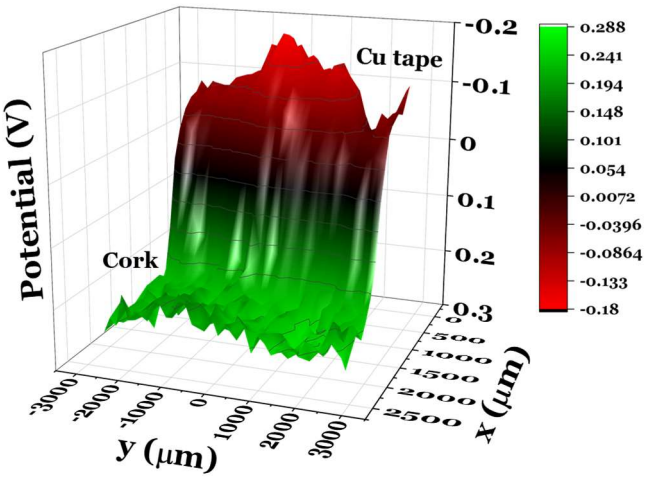

Figure 36. 3D plot of the Potential vs Surface of the Cork/Cu tape with SKP; 2nd experiment

Figure 37. Cork´s sample

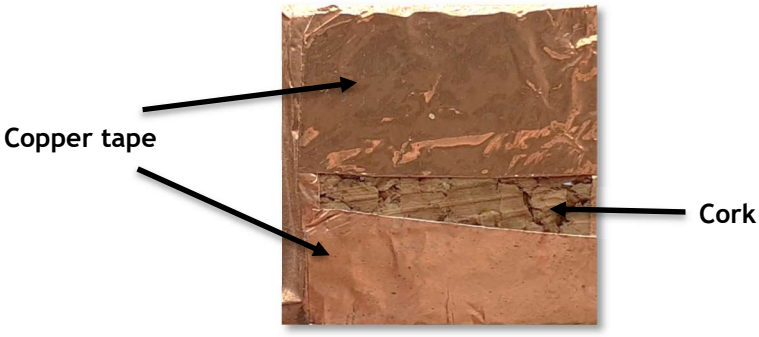

Figure 38. Cork with Cu tape

4.3 - Double heterojunction cell: The ZnO case study

In this case, ZnO is studied with two different cells Cu/ZnO/Al and Cu/ZnO/Zn making use of the SKP technique, with different scans length: 1.2 and 2.2 cm. These experiments aim to study some properties and the dielectric behavior of ZnO, in a double heterojunction cell with metal-semiconductor characteristics, through the dynamic study of the potentials on the various surfaces of the metals and the oxide. The comparative analysis of all these elements gives us an overview of the demeanor of positive electrode/ZnO and negative electrode/ZnO. Copper was used as a positive electrode, while aluminum and zinc were used as negative electrodes. From the results we can evaluate and improve the application of ZnO and metallic electrodes in other studies of lithium-based cells. All SKP

measurements were performed with topography's capacitive tracking (CTM) and it is taken into account by the instrument in the SKP measurements.

In this work, the SKP results are referenced to the standard hydrogen electrode (SHE). The values can be easily converted to the Physical scale, having as reference the electrons at rest in vacuum at 0ev, as the publication by IUPAC[69]. The corresponding of reference SHE scale 0V = -4.4 eV (Physical scale). The absolute chemical potential energy measured from the vacuum corresponds to the work function when the surface potential is φ=0. The relationship between the absolute Physical scale and SHE scale enables referring the energy levels to a common reference value.

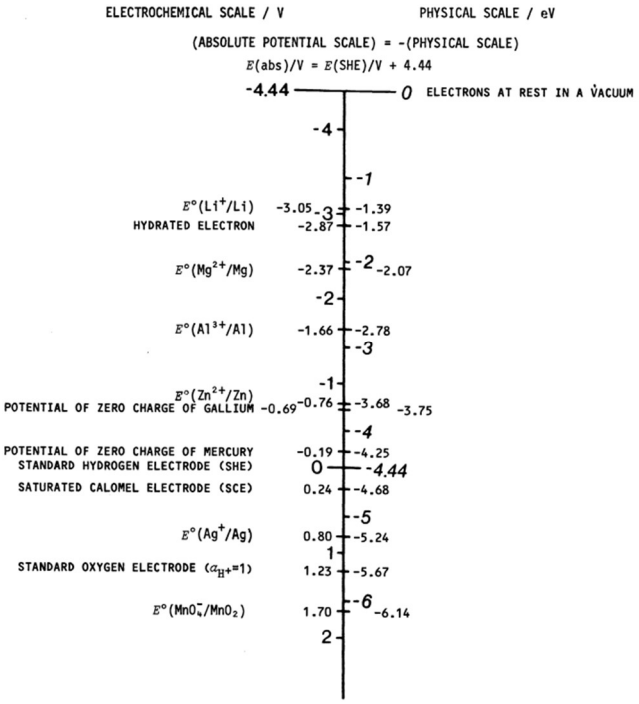

Figure 39. Conversion of relative electrode potentials into electronic energies[69]

4.3.1. Double heterojunction Cu/ZnO/Al cell

The following figure 42 presents the results of the analysis of the topography of the cell´s surface, by CTM, electrically connected to SKP with Cu tape, and Figure 43 shows the SKP results for the CDP of the Cu/ZnO/Al cell.

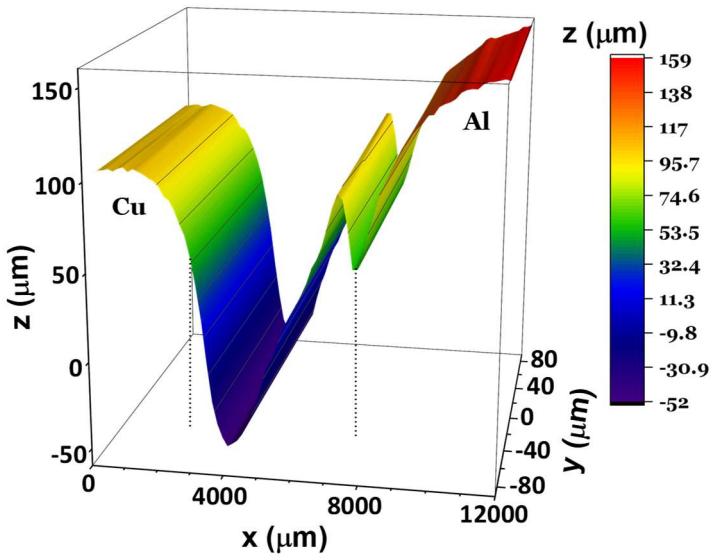

Figure 40. CTM topography of the cell´s surface Cu/ZnO/Al. Cu electrode Connect to M470 through Cu tape.The different regions are separated by dots.

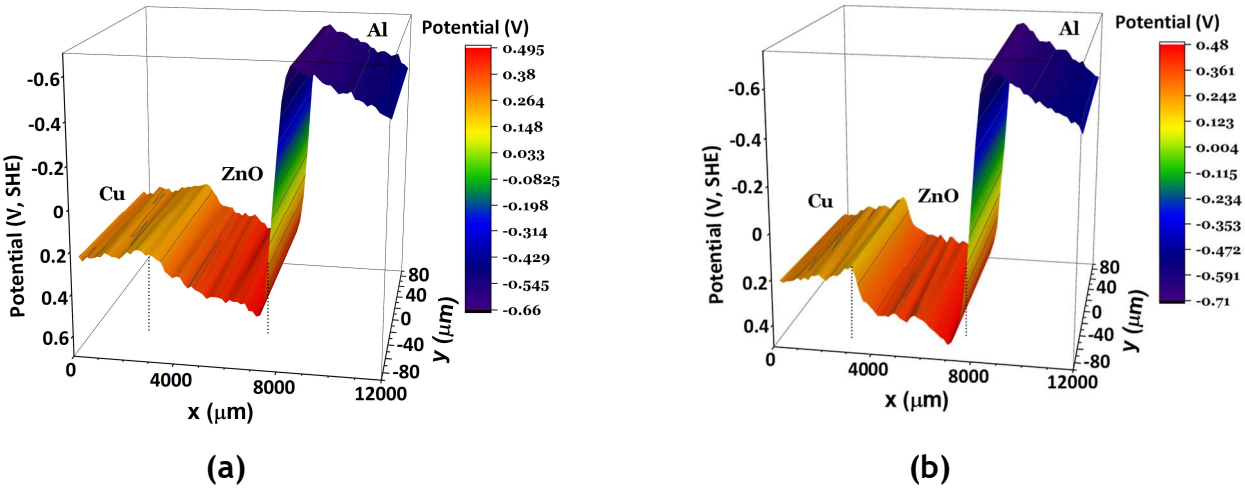

Figure 41. 3D plots of the Potential *vs* Surface of the Cu/ZnO/Al cell with SKP:
(a) First cell experiment (b) cell experiment made ~40 min interval after the 1st experiment.

The cell was electrically connected to SKP with Cu tape. SKP surface chemical potentials of the Cu and Al show a substantial gradient, especially with the Al electrode. The electrode Cu tends to align its electrochemical potential with ZnO potential. There is a

small peak observed (orange arrow) that must be related to the electrical double-layer capacitor with associated charge gradients. Figures 43(a), (b) and 44, SKP show two cell experiments made with 40 minutes of interval and can observe that the surface potentials almost do not change.

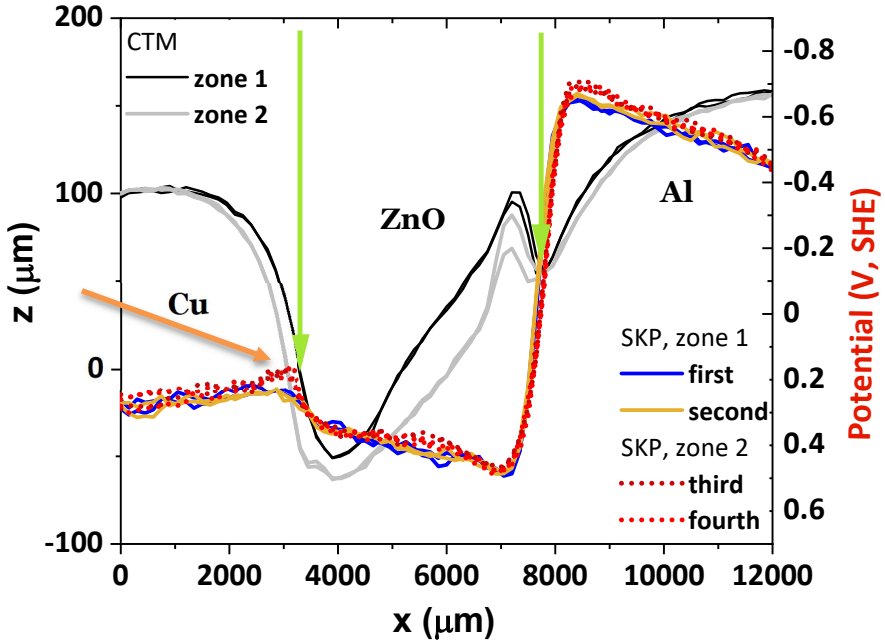

Figure 42. Consecutive CTM and SKP experiments correspond to two different zones of the cell Cu/ZnO/Al.

As can be seen, figure 44 shows CTM (grey and black lines) and SKP (blue, brown and dots lines) consecutive experiments with time intervals of 30-40 min corresponding to two different zones of the cell. The results analysis shows the surface potential almost does not change which indicates a reliable and stable system throughout time.

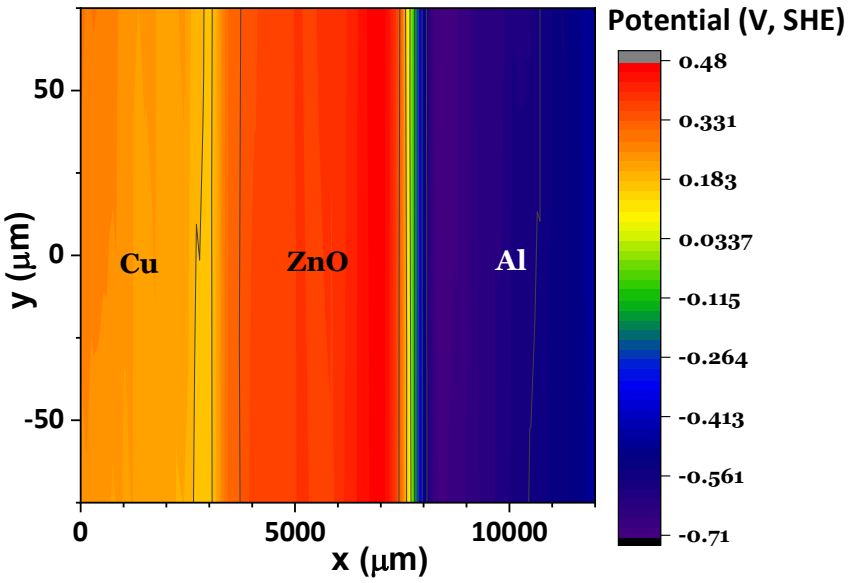

Figure 43. 2D plots of the potential gradient of the Cu/ZnO/Al cell's obtained with SKP.

The gradient of potential (figure 45) shows the soft passage Cu/ZnO and the sharp transition from 0.48V (ZnO) to -0.66V(Al), highlighting the internal resistance (quantum well) correspondent to an almost opened circuit at the ZnO/Al interface.

Performing experiments in a wider scan (figures 46-47) 2.2 cm, it is confirmed the alignment of the surface chemical potentials at the Cu/ZnO heterojunction and discontinuity at the ZnO/Al heterojunction.

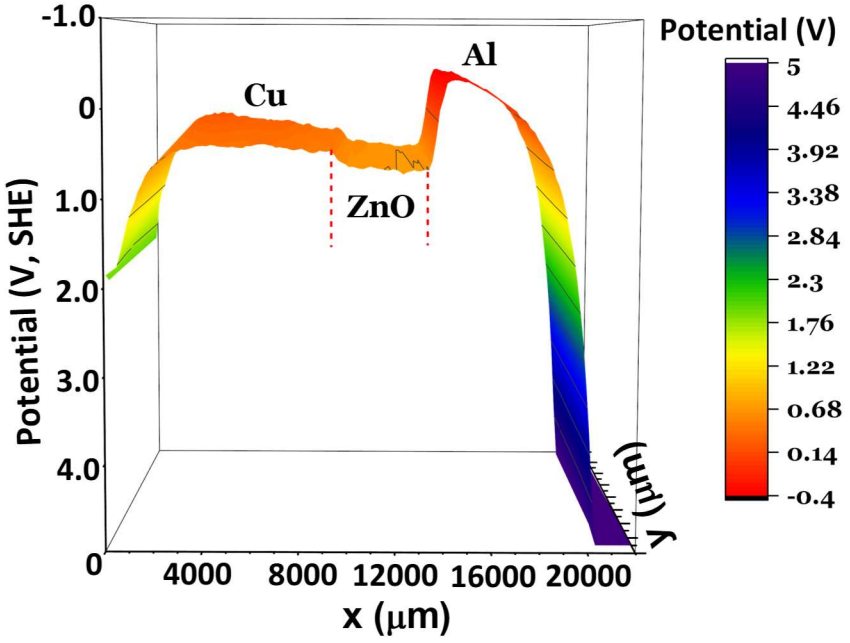

Figure 44. 3D plot of the Potential *vs* Surface extended Cu/ZnO/Al cell experience with SKP.

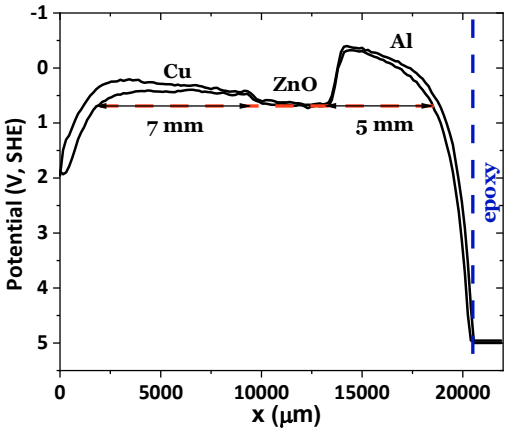

Figure 45. Extended Cu/ZnO/Al cell experiment Potential *vs* Surface with SKP.
Cu electrode connected to the M470 through the Cu tape, approaching the epoxy at the Al end

These experiences show that the Cu/ZnO heterojunction has a continuity of the surface chemical potential, with a slight accumulation of negative charge at the interface (figures 43-46). At the ZnO/Al junction, there is a step increase in the surface potential, possibly corresponding to a potential well.

Experimental tests were performed by closing the SKP/CTM circuit to the cell by the Al electrode (figure 47). These results confirm the expected when compared to previous experiences, performed with the circuit closed by the Cu electrode, evaluating the evolution and experimental values of surface potential. The Al/ZnO heterojunction is seeing a brutal discontinuity of the surface chemical potential and on the ZnO/Cu side there is a smooth transition of the surface potentials.

In figure 48, it notices a bending of the surface chemical potential of ZnO (orange arrow) at the ZnO/Cu interface that may indicate a more positively charged region, in this case an accumulation of Zn^{2+} ions, an effect that may arise when metal-semiconductor contact exists.

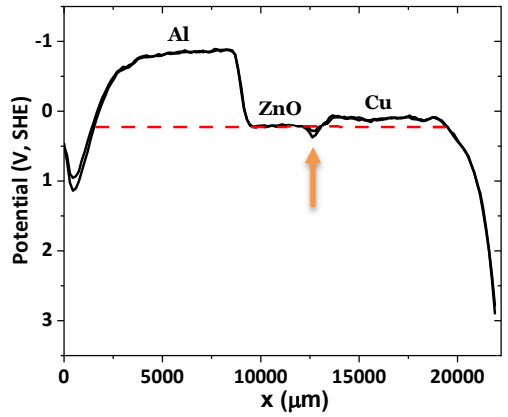

Figure 46. Extended Al/ZnO/Cu cell experience Potential *vs* Surface with SKP.

The voltage measurement with a multimeter at the terminals bulk cell in an open circuit voltage (OCV) was ΔVoc = 0.065 V. Thus, the cell's internal circuit is not totally open, a bulk voltage was registered and the impedance could be calculated by the EIS test, obtaining the equivalent circuit, R_2 = 4.6×10^7 Ω.cm, C_1 = 2.6 pF.cm$^{-1,}$ of the internal resistance and capacitance of the cell (figure 48). The capacitance C_1 was calculated for the dimensions of the cell (figure 49), A = (2.2 x 0.47) cm^{-2} and d = 0.45 cm.

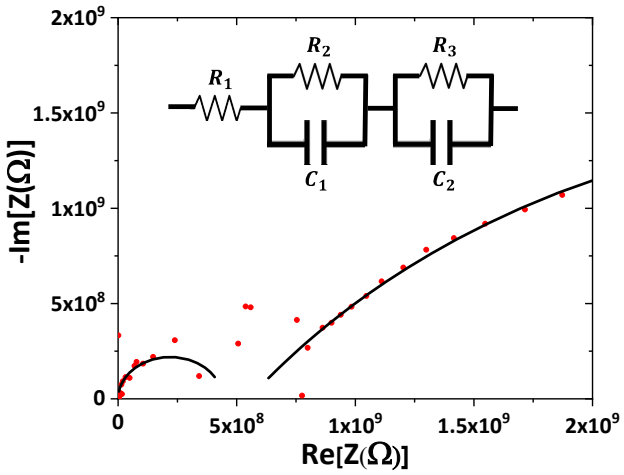

Figure 47. Result analysis of the EIS: Nyquist plot and equivalent circuit

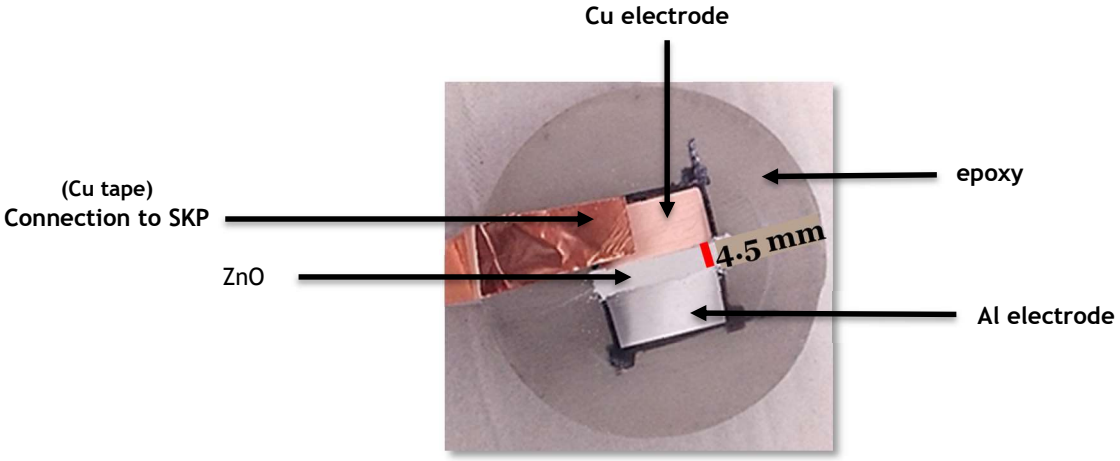

Figure 48. The appearance of the Cu/ZnO/Al cell

The potential difference at the open circuit (OCV) of the Al/ZnO/Cu cell, before and after the experiments, indicates that the cell is highly resistive, ΔV_{oc_Before} =0.065 V and ΔV_{oc_After} = 0.066 V.

Considering the SKP experimental values of the chemical potential of the aluminium $\mu_{(Al)}$ and copper and $\mu_{(Cu)}$:

$\left|\frac{\mu_{(Al)}-\mu_{(Cu)}}{e}\right| = 1.13\ V$ and using the potential,

$V = \left|\frac{\mu_{(Al)}-\mu_{(Cu)}}{e}\right| - (R_i I)_{total} = 0.07\ \text{V} \Leftrightarrow R_i = 0.46 \times 10^7\ \Omega$ or $R_i = 0.23 \times 10^7\ \Omega$.cm

which results into the approximate resistance obtained by EIS, $R_2 = 4.6{\times}10^7\ \Omega.\text{cm}$.

Before the EIS analysis, the cell Cu/ZnO/Al rested for 12 h at room temperature. The impedance is very high and the data suffer from scattering, thus the experimental resistance obtained by EIS is not as quite as expected.

In the next picture, it can be seen the SKP, *in operando*, performing the experiment with the Al/ZnO/Cu cell,

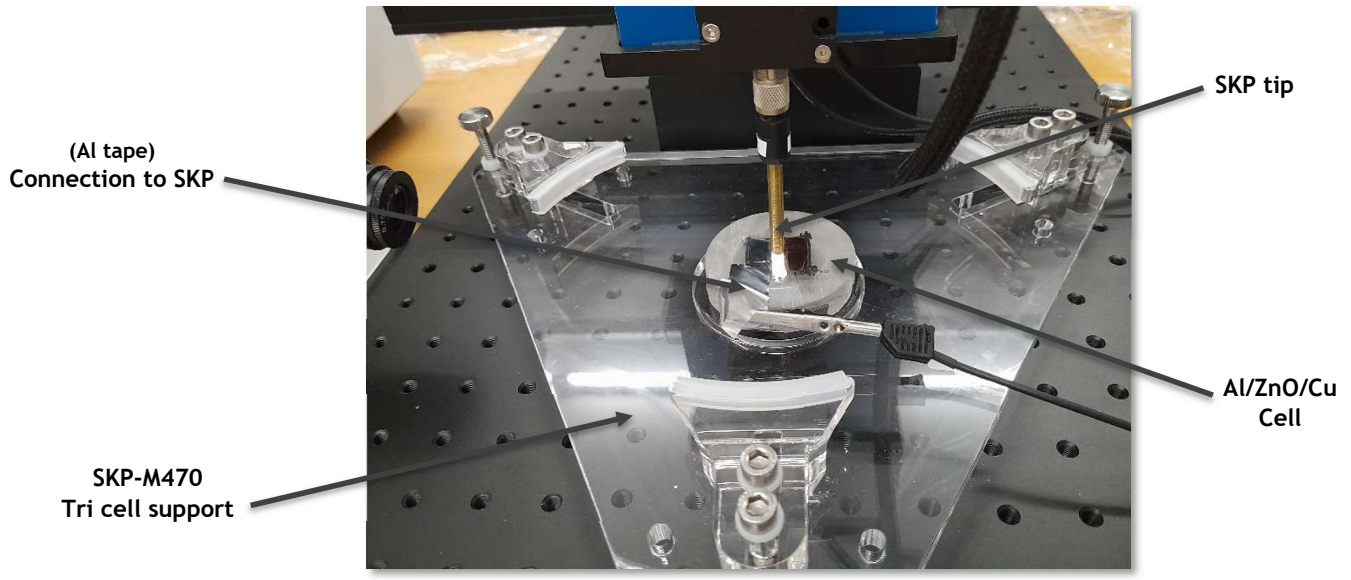

Figure 49. SKP *in operando* with the Al/ZnO/Cu connected by Al electrode.

In the CTM/SKP essays of the Al/ZnO/Cu cell with a scan length of 1.2 cm (figures 52-55) it was obtained identical values of surface chemical potential and behavior than performed with the 2.2 cm scan (figures 45-47). In the analysis of the results, slight differences in the value of the surface chemical potential ZnO at the Al/ZnO interface (figure 55, orange arrow), more pronounced, doubling towards the positive potentials (SHE scale). This aspect indicates the presence of an accumulation of positively charged species. Compared with

the extended Al/ZnO/Cu cell experience (figure 48) it also shows the accumulation of positive charges but on the side of the ZnO/Cu interface. These inverse behaviors are in agreement with the fact that the chemical potentials of Al and Cu are greater than those of ZnO's (physical scale), and thus an initial accumulation of positively charged species at both interfaces is necessary to equalize Fermi levels[70].

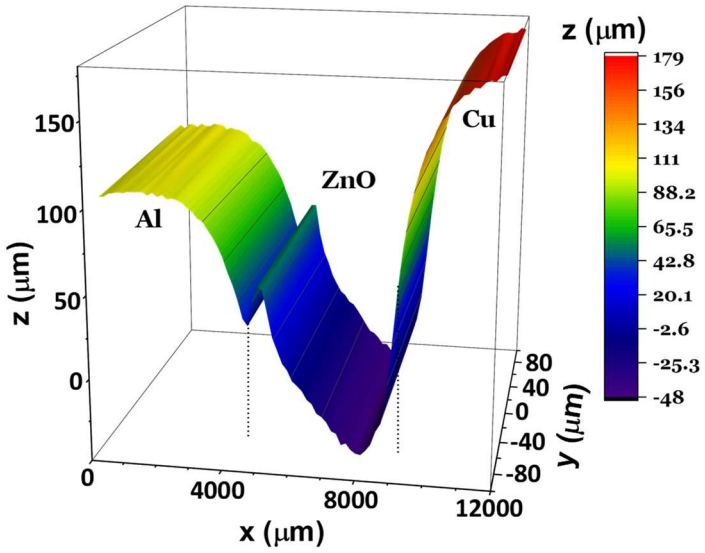

Figure 50. CTM topography of the cell´s surface Al/ZnO/Cu. Circuit close through the Al electrode

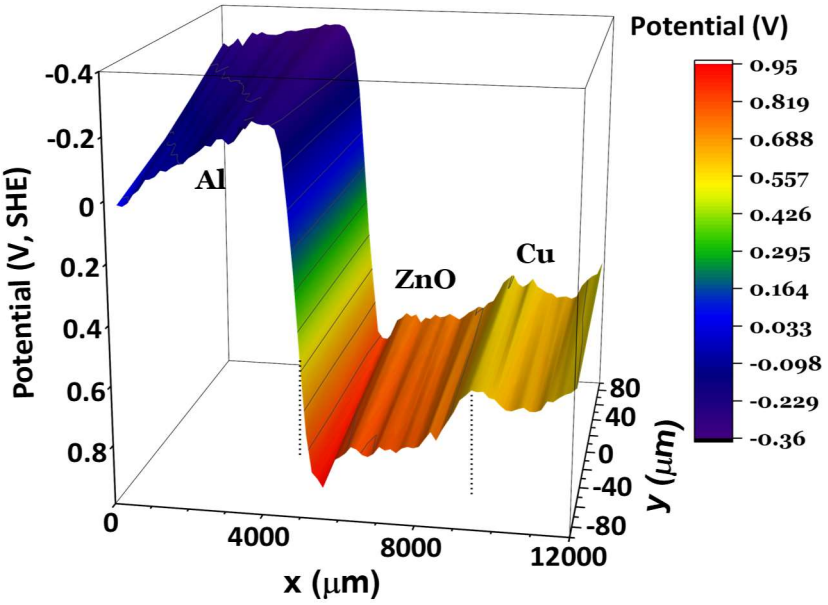

Figure 51. 3D plot of the Potential vs Surface Al/ZnO/Cu cell experience with SKP. Circuit close through the Al electrode.

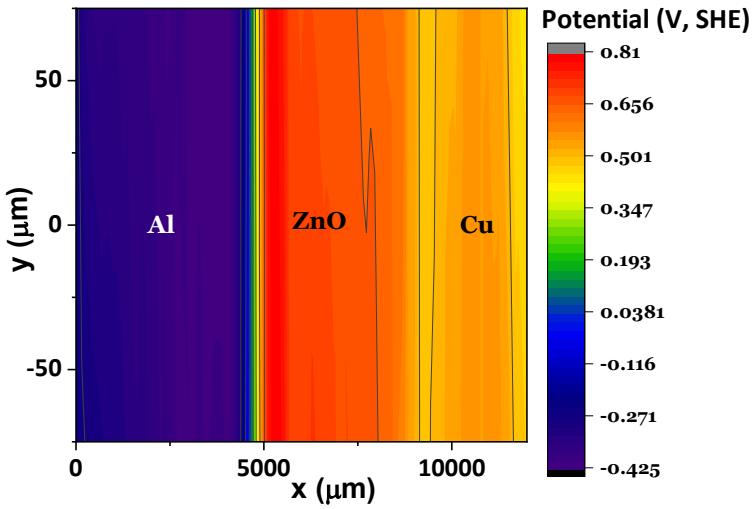

Figure 52. 2D plots of the potential gradient of the Al/ZnO/Cu cell's obtained with SKP.

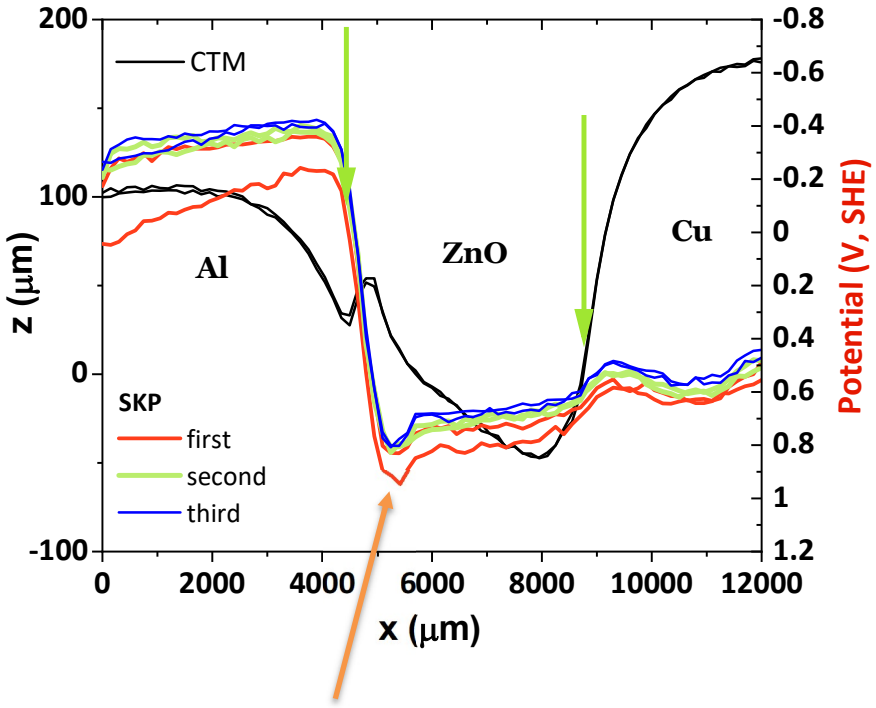

Figure 53. Consecutive CTM and SKP experiments correspond to two different zones of the cell Al/ZnO/Cu. Al electrode is connected to M470 through the Al tape.

In the tests with the circuit closed through the Al electrode to SKP, when the Al is connected to the SKP instead of Cu , substantial changes can not be seen in the analysis results (figure 55). After the second line obtained in the first run, all the subsequent SKP experiments show similar surface chemical potential behavior. In figure 55, the green arrows delimit the ZnO zone.

In the figures 48 and 53 to 55 it was mentioned Al/ZnO/Cu cell. That is the same cell than Cu/ZnO/Al but only the order was changed to distinguish when the cell was connected through the Al electrode (Al/ZnO/Cu) or through the Cu electrode (Cu/ZnO/Al).

4.3.2. Double heterojunction Cu/ZnO/Zn cell

In this study case, it is also sought to study the ZnO with other materials used in batteries/cells, in order to be an added benefit for the studies of batteries. Thus, a heterojunction cell/ZnO/Zn was created, keeping the positive electrode (Cu) and changing the negative to the Zn metal.

The procedures of the experiments of the 4.3.2 section were similar to those performed in experiments with the Cu/ZnO/Al cell.

The following figure shows the results of the analysis of the topography of the cell surface (figure 56), by CTM, electrically connected to SKP with Cu tape. Figure 58 presents the SKP results for the CDP of the Cu/ZnO/Zn cell.

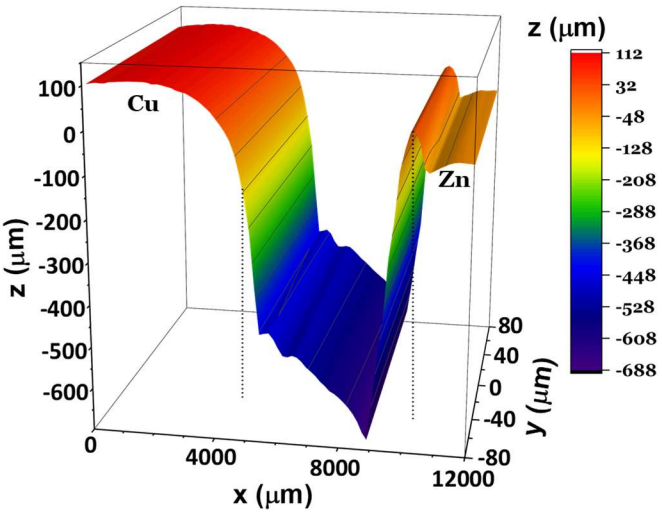

Figure 54. CTM topography of the cell´s surface Cu/ZnO/Zn.

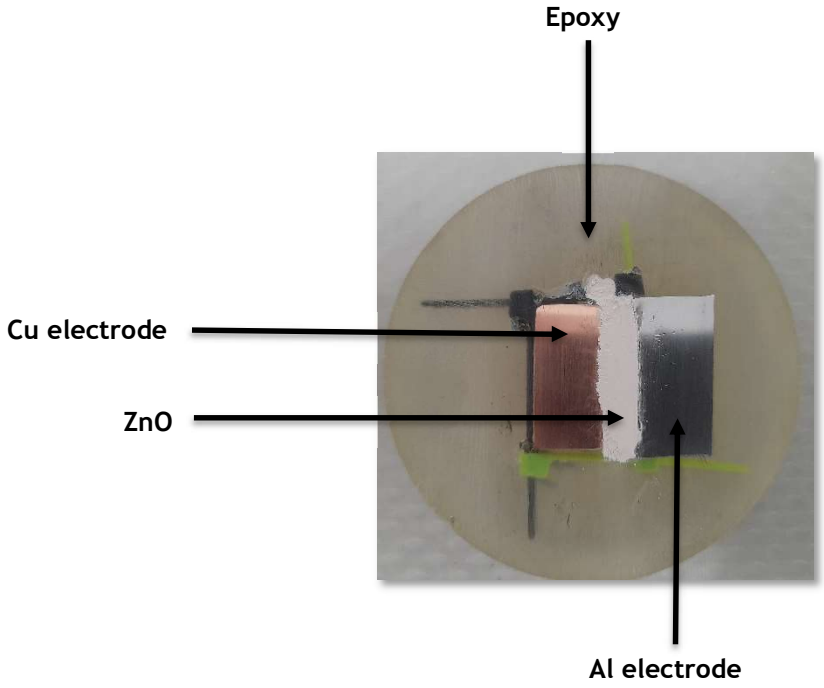

Figure 55. Cu/ZnO/Zn cell

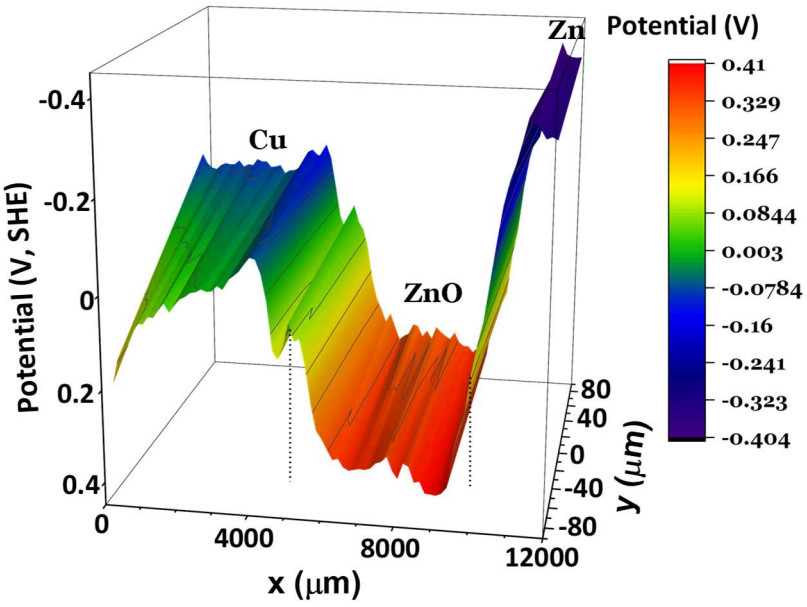

Figure 56. 3D plot of the Potential *vs* Surface of the Cu/ZnO/Zn cell with SKP

The cell Cu/ZnO/Zn was electrically connected to SKP with Cu tape. SKP surface chemical potentials of the Cu and Zn present a gradient, especially the Zn electrode, which is noticeably more abrupt. The electrode Cu tends to align its electrochemical potential with ZnO potential, as can be seen in figure 58. This analysis is similar to the experiments that were made with Cu/ZnO/Al. Thus, it turns out that they have a similar bearing.

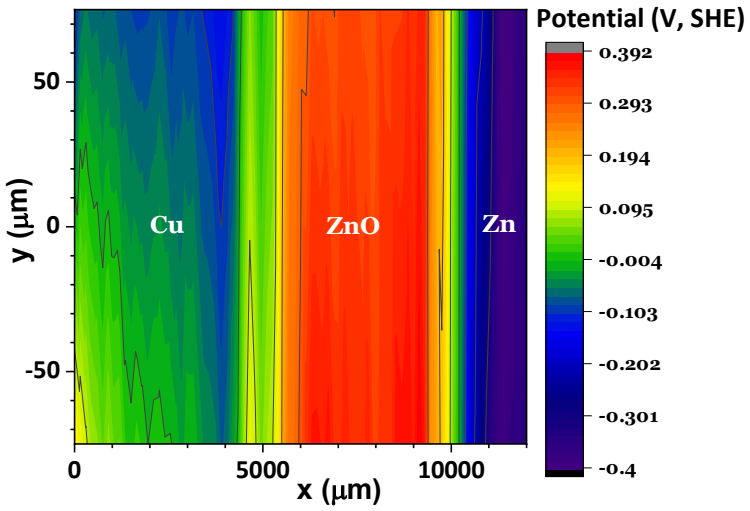

Figure 57. 2D plots of the potential gradient of the Cu/ZnO/Zn cell's obtained with SKP.

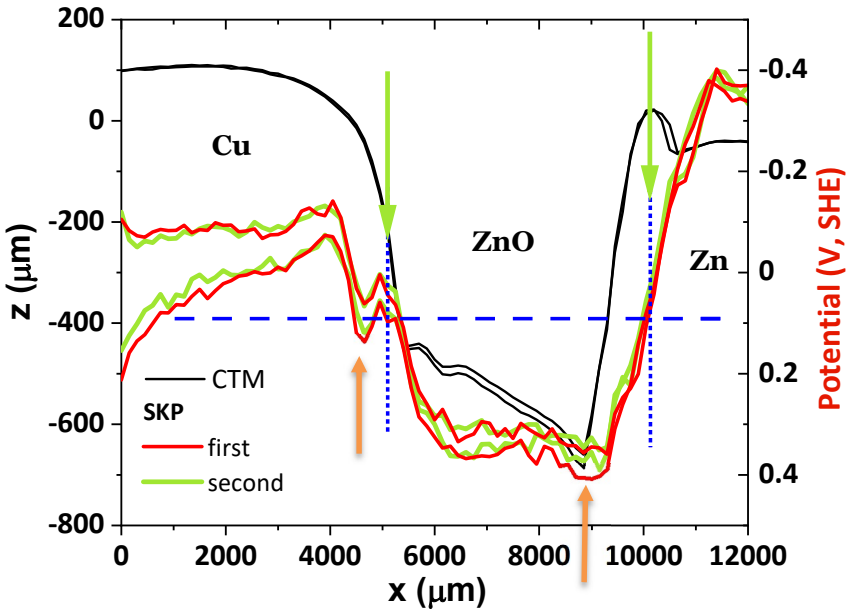

Figure 58.Consecutive CTM and SKP experiments correspond to two different zones of the cell Cu/ZnO/Zn. Cu electrode connected to the M470 through the Cu tape

Hence, it can be seen that the results obtained with the experiments with the Cu/ZnO/Zn cell (figures 58-61) present the resistive element in ZnO/Zn as well seen in the experiments with the Cu/ZnO/Al cell at the interface with ZnO/Al. In the Cu/ZnO/Al cell, $\Delta V = R_i I$ assumes the values of 0.81 and 0.79 V on the Zn/ZnO interface.

In figure 60, it has been observed time after introducing the ZnO in the cell and performing the CTM scan (first: 25 minutes, figure 58 and second: 59 minutes, figure 59) has no substantial changes over time. Therefore, the cell with ZnO demonstrated a stable status.

As can also be seen, in figure 60, a notorious accumulation of positive charge was observed in both interfaces (orange arrows), on Cu/ZnO and ZnO/Zn, similar to the experiencies with Cu/ZnO/Al (figures 48 and 55).

In the following figure (61), one sees the surface chemical potential of materials in electrical contact, on some points (green line), tends to equalize their surface chemical potentials, due to dielectric metal interactions. This phenomenon also occurs in the experiments with the cell Cu/ZnO/Al (figures 47-48), although with the cell Cu/ZnO/Zn it is more notorious.

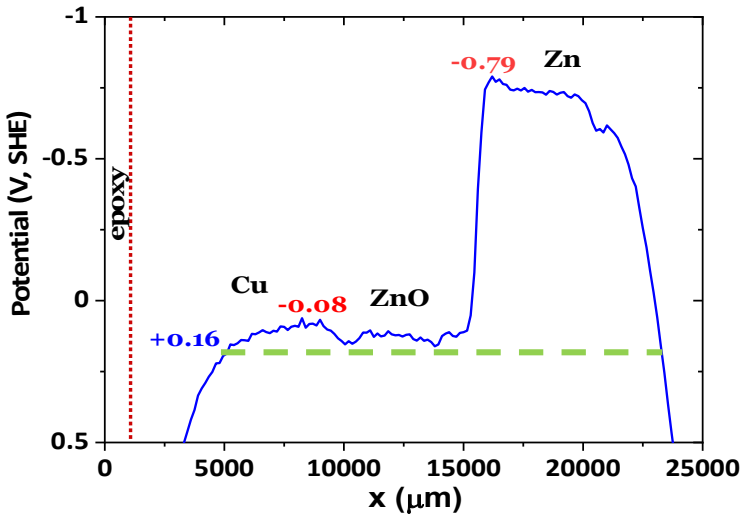

Figure 59. Extended Cu/ZnO/Zn cell experience Potential *vs* Surface with SKP.
Cu electrode connected to the M470 through the Cu tape, approaching the epoxy at the Cu side.

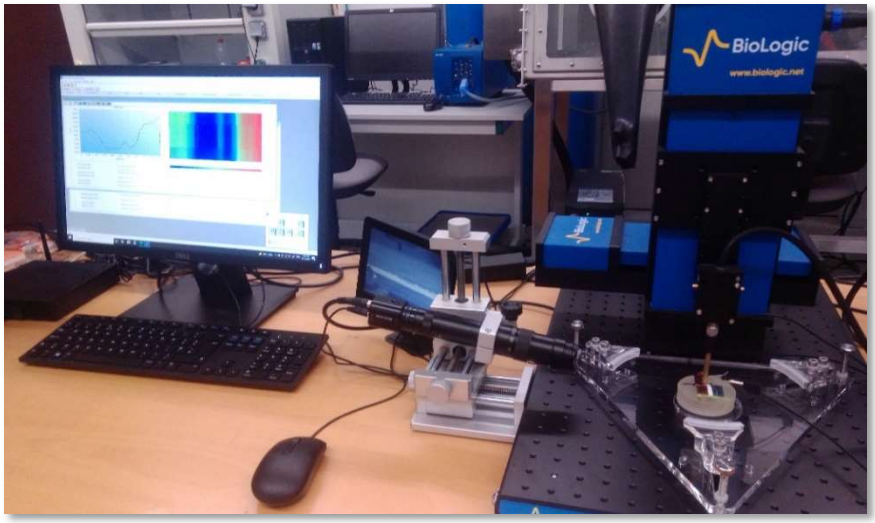

Figure 60. SKP in operando with the Cu/ZnO/Zn connected by Cu electrode.

Chapter 5

Conclusions

In this work, metals, single heterojunctions and double heterojunctions were analyzed, where metals are not only electrodes but also current collectors.

In the study of isolated metals, it was concluded that the potential results are within the standard nominal values. In the case of zinc, it may have been a little different but still within the experimental incertainties.

The SKP plots of the single heterojunctions do not show any surface chemical potential gradients at the Zn/Cu and Al/Cu interfaces. The metals were insulated by air. It also shows that the metals had a flat surface without bending as shows in the Al/ZnO/Cu and Zn/ZnO/Cu cells. The copper, when measured alone as a control, shows an average surface potential of 0.19 V and presents values from 0.166 to 0.216 V in the experiments, which proves the results of this work.

In the double heterojunction cell, the dielectric ZnO revealed a bending of the conduction and valence bands due to the diffusion of Zn^{2+} to the interstitial sites with release electrons to the donor band. It is shown the accumulation of positively charged species on the ZnO interfaces appears in both experiments (Cu/ZnO/Al and Cu/ZnO/Zn). The positive charge accumulation detail is more clearly observed at Cu/ZnO/Zn interfaces.

Metallic collector electrodes have high dynamics and the ability to accumulate charges in equal and opposite signs, which results in bending their surface chemical potentials with large amplitude. In the operating cell, metals reflect a tendency to align surface chemical potentials within the cell at the dielectric level. Therefore, indicating that the dielectric effect on the surface chemical potential of metals is long-range and based on an electric field.

An alignment of the surface chemical potentials of the three materials away from the interfaces and away from the edges of the cell was observed in these two cell heterojunctions.

ZnO behaves like a dielectric that has charge storage capacity, being inexpensive, safe, stable and reliable.

Chapter 6

Future work

The field of activity for semiconductors and batteries is extensive and of paramount interest. This work revealed that it can apply and associate new materials in the area of batteries but it can easily be extended to solar cells and other equipment in micro and nano scale. This study can be extended to other oxides such as Al_2O_3, Li_2O, CaO, MgO, SiO and SnO_2. In addition to these, experiments with solid electrolytes would be compelling on a use basis in Cu//Zn and Cu//Al cells. In addition to the SKP method, which proved to be very useful, nano studies can also be carried out, with other complementary methods.

Chapter 7

Research activities

Published Articles

A. Nuno Guerreiro, Manuela C. Baptista, Beatriz A. Maia, M. Helena Braga. “Interfacial chemistry with ZnO: in operando work functions in hetero cells” ACS Applied Energy Materials Vol. 5 Nº. 8 p. 9811-9822. DOI: 10.1021/acsaem.2c01503

Abstracts in conferences:

FISICA 2022 - 23ª Conferência Nacional de Física: A. Nuno Guerreiro, M. Helena Braga. “Scanning Kelvin Probe - Characterization of solid-state devices”

Congresso MATERIAIS 2022: A. Nuno Guerreiro, M. Helena Braga.”Structural Cork in Ferroelectric Solid-State Devices by Scanning Kelvin Probe”

Congresso MATERIAIS 2022: Manuela C. Baptista, Hesham Khalifa, A. Nuno Guerreiro, M. Helena Braga. “Anode-Less Rechargeable Lithium Battery: The Effect of an Artificial Interface Layer”

Congresso DCE21 - Congresso Doutoral em Engenharia: A. Nuno Guerreiro, M. Helena Braga .“Scanning Kelvin Probe to advance solid-state devices”

Congresso DCE21 - Congresso Doutoral em Engenharia: Federico Danzi, A. Nuno Guerreiro, M. Helena Braga .“ All-solid state structural batteries: Manufacturing and electrochemical tests”

References

[1] W. R. Harper and P. R. S. L. A, "The Volta effect as a cause of static electrification," *Proc. R. Soc. London. Ser. A. Math. Phys. Sci.*, vol. 205, no. 1080, pp. 83–103, 1951, doi: 10.1098/rspa.1951.0019.

[2] W. A. Zisman, "A new method of measuring contact potential differences in metals," *Rev. Sci. Instrum.*, vol. 3, no. 7, pp. 367–370, 1932, doi: 10.1063/1.1748947.

[3] B. Martin and H. Kliem, "Space charge measurements with the scanning Kelvin probe," *IEEE Trans. Dielectr. Electr. Insul.*, vol. 15, no. 2, pp. 560–567, 2008, doi: 10.1109/TDEI.2008.4483478.

[4] A. Hussain and M. Haque, "Novel Probe Designs for the Scanning Kelvin Probe System," *STM Journals*, vol. 1, no. 1, pp. 1–30, 2014.

[5] M. Rohwerder, "Passivity of metals and the kelvin probe technique," *Encycl. Interfacial Chem. Surf. Sci. Electrochem.*, pp. 414–422, Jan. 2018, doi: 10.1016/B978-0-12-409547-2.13405-5.

[6] N. A. Surplice and R. J. D'Arcy, "A critique of the Kelvin method of measuring work functions," *J. Phys. E.*, vol. 3, no. 7, pp. 477–482, 1970, doi: 10.1088/0022-3735/3/7/201.

[7] B. Ritty, F. Wachtel, F. Ott, R. Manquenouille, and J. B. Donnet, "New application of the Kelvin method involving the scanning of the bucking voltage," *Rev. Sci. Instrum.*, vol. 51, no. 10, pp. 1421–1423, 1980, doi: 10.1063/1.1136091.

[8] J. Baczyński, "Computer-controlled vibrating capacitor technique for determining work function," *Rev. Sci. Instrum.*, vol. 59, no. 11, pp. 2471–2473, 1988, doi: 10.1063/1.1139930.

[9] G. Friedbacher and H. Fuchs, "Classification of scanning probe microscopies," *Pure Appl. Chem.*, vol. 71, no. 7, pp. 1337–1357, 1999, doi: 10.1046/j.1365-3075.1999.00266.x.

[10] R. Car, G. Ertl, and H.-J. Freund, *Kelvin Probe Force microscopy:From single charge detection to device characterization*. Springer International Publishing AG, 2018. doi: 10.1007/978-3-319-75687-5.

[11] X. Shi, W. Qing, T. Marhaba, and W. Zhang, "Atomic force microscopy - Scanning electrochemical microscopy (AFM-SECM) for nanoscale topographical and electrochemical characterization: Principles, applications and perspectives," *Electrochim. Acta*, vol. 332, p. 135472, Feb. 2020, doi: 10.1016/J.ELECTACTA.2019.135472.

[12] A. Moldovan, A. Marinescu, S. Brajnicov, N. Dumitrescu, N. D. Scarisoreanu, and M. Dinescu, "Scanning probe techniques for nanoscale imaging and patterning," *Funct. Nanostructured Interfaces Environ. Biomed. Appl.*, pp. 97–112, Jan. 2019, doi: 10.1016/B978-0-12-814401-5.00005-0.

[13] M. Wicinski, W. Burgstaller, and A. W. Hassel, "Lateral resolution in scanning Kelvin probe microscopy," *Corros. Sci.*, vol. 104, pp. 1–8, 2016, doi: 10.1016/j.corsci.2015.09.008.

[14] A. Nazarov, N. Le Bozec, and D. Thierry, "Scanning Kelvin Probe assessment of steel corrosion protection by marine paints containing Zn-rich primer," *Prog. Org. Coatings*, vol. 125, pp. 61–72, Dec. 2018, doi: 10.1016/J.PORGCOAT.2018.08.024.

[15] G. Ebrahimi, F. Rezaei, and J. Neshati, "Investigation on corrosion protection mechanism of polyaniline nanoparticles doped with phosphoric acid by scanning Kelvin probe and other electrochemical methods," *J. Taiwan Inst. Chem. Eng.*, vol. 70, pp. 427–436, Jan. 2017, doi: 10.1016/J.JTICE.2016.11.007.

[16] G. Williams, H. N. McMurray, and R. C. Newman, "Surface oxide reduction by hydrogen permeation through iron foil detected using a scanning Kelvin probe," *Electrochem.*

commun., vol. 27, pp. 144–147, Feb. 2013, doi: 10.1016/J.ELECOM.2012.11.022.

[17] Ö. Özkanat, B. Salgin, M. Rohwerder, J. M. C. Mol, H. De Wit, and H. Terryn, "Scanning Kelvin probe study of (Oxyhydr)oxide surface of aluminum alloy," *J. Phys. Chem. C*, vol. 116, no. 2, pp. 1805–1811, 2012, doi: 10.1021/jp205585u.

[18] L. Ganborena, J. M. Vega, B. Özkaya, H. J. Grande, and E. García-Lecina, "AN SKP and EIS study of microporous nickel-chromium coatings in copper containing electrolytes," *Electrochim. Acta*, vol. 318, pp. 683–694, Sep. 2019, doi: 10.1016/J.ELECTACTA.2019.05.108.

[19] C. Senöz, S. Evers, M. Stratmann, and M. Rohwerder, "Scanning Kelvin Probe as a highly sensitive tool for detecting hydrogen permeation with high local resolution," *Electrochem. commun.*, vol. 13, no. 12, pp. 1542–1545, Dec. 2011, doi: 10.1016/J.ELECOM.2011.10.014.

[20] A. Castaldini, D. Cavalcoli, A. Cavallini, and M. Rossi, "Scanning Kelvin probe and surface photovoltage analysis of multicrystalline silicon," *Mater. Sci. Eng. B*, vol. 91–92, no. 92, pp. 234–238, Apr. 2002, doi: 10.1016/S0921-5107(01)01018-2.

[21] K. Dirscherl, I. Baikie, G. Forsyth, and A. Van der Heide, "Utilisation of a micro-tip scanning Kelvin probe for non-invasive surface potential mapping of mc-Si solar cells," *Sol. Energy Mater. Sol. Cells*, vol. 79, no. 4, pp. 485–494, Sep. 2003, doi: 10.1016/S0927-0248(03)00064-3.

[22] B. Lägel, I. D. Baikie, and U. Petermann, "A novel detection system for defects and chemical contamination in semiconductors based upon the Scanning Kelvin Probe," *Surf. Sci.*, vol. 433–435, pp. 622–626, Aug. 1999, doi: 10.1016/S0039-6028(99)00025-4.

[23] A. Nazarov, T. Prosek, and D. Thierry, "Application of EIS and SKP methods for the study of the zinc/polymer interface," *Electrochim. Acta*, vol. 53, no. 25, pp. 7531–7538, Oct. 2008, doi: 10.1016/J.ELECTACTA.2007.11.053.

[24] B. Andreon, B. L. Guenther, W. L. Cavalcanti, L. Colombi Ciacchi, and P. Plagemann, "On the use of scanning Kelvin probe for assessing in situ the delamination of adhesively bonded joints," *Corros. Sci.*, vol. 157, pp. 11–19, Aug. 2019, doi: 10.1016/J.CORSCI.2019.03.001.

[25] M. H. Braga *et al.*, "Topological feedback towards energy harvesting," 2022.

[26] M. Rohwerder, S. Isik-Uppenkamp, and M. Stratmann, "Application of SKP for in situ monitoring of ion mobility along insulator/insulator interfaces," *Electrochim. Acta*, vol. 54, no. 25, pp. 6058–6062, Oct. 2009, doi: 10.1016/J.ELECTACTA.2009.03.012.

[27] G. Williams and N. McMurray, "Latent fingermark visualisation using a scanning Kelvin probe," *Forensic Sci. Int.*, vol. 167, no. 2–3, pp. 102–109, 2007, doi: 10.1016/j.forsciint.2006.08.018.

[28] M. Thompson, L. E. Cheran, M. Zhang, M. Chacko, H. Huo, and S. Sadeghi, "Label-free detection of nucleic acid and protein microarrays by scanning Kelvin nanoprobe," *Biosens. Bioelectron.*, vol. 20, no. 8, pp. 1471–1481, Feb. 2005, doi: 10.1016/J.BIOS.2004.06.022.

[29] B. J. Gow *et al.*, "Electrical potential of acupuncture points: Use of a noncontact scanning kelvin probe," *Evidence-based Complement. Altern. Med.*, vol. 2012, no. January 2014, 2012, doi: 10.1155/2012/632838.

[30] S. Huber, M. Wicinski, and A. W. Hassel, "Suitability of Various Materials for Probes in Scanning Kelvin Probe Measurements," *Phys. Status Solidi Appl. Mater. Sci.*, vol. 215, no. 15, Aug. 2018, doi: 10.1002/PSSA.201700952.

[31] "Height tracking with the SKP370 or SKP470 module - Scanning Probes - Application Note 1 - BioLogic." https://www.biologic.net/documents/height-tracking-with-the-skp370-or-skp470-module-scanning-probes-application-note-1/ (accessed Jul. 14, 2022).

[32] A. Kahn, "Fermi level, work function and vacuum level Materials Horizons FOCUS," *Cite this Mater. Horiz*, vol. 3, p. 27, 2016, doi: 10.1039/c5mh00160a.

[33] M. Rohwerder and F. Turcu, "High-resolution Kelvin probe microscopy in corrosion science: Scanning Kelvin probe force microscopy (SKPFM) versus classical scanning Kelvin probe (SKP)," *Electrochim. Acta*, vol. 53, no. 2, pp. 290–299, 2007, doi:

10.1016/j.electacta.2007.03.016.

[34] G. S. Frankel *et al.*, “Potential control under thin aqueous layers using a Kelvin Probe,” *Corros. Sci.*, vol. 49, no. 4, pp. 2021–2036, 2007, doi: 10.1016/j.corsci.2006.10.017.

[35] K. M. Gupta and N. Gupta, “Semiconductor Materials: Their Properties, Applications, and Recent Advances,” in *Advanced Semiconducting Materials and Devices*, Springer International Publishing, 2016, pp. 3–40. doi: 10.1007/978-3-319-19758-6_1.

[36] I. D. Baikie and P. J. Estrup, “Low cost PC based scanning Kelvin probe,” *Rev. Sci. Instrum.*, vol. 69, no. 11, pp. 3902–3907, 1998, doi: 10.1063/1.1149197.

[37] N. SATO, “Electrocthemistry of Semiconductors,” *Tetsu-to-Hagane*, vol. 76, no. 9, pp. 1423–1436, 1998, doi: 10.2355/tetsutohagane1955.76.9_1423.

[38] A. Shaheen, J. Alam, and M. S. Anwar, “Band Structure and Electrical Conductivity in Semiconductors,” *Mater. Eng.*, pp. 1–26, 2010.

[39] D. Lide, “Handbook of chemistry and physics: a ready-reference book of chemical and physical data,” *Choice Rev. Online*, vol. 47, no. 07, pp. 47–3553, Mar. 2010, doi: 10.5860/CHOICE.47-3553.

[40] Z. L. Wang, “Nanostructures of zinc oxide,” *Mater. Today*, vol. 7, no. 6, pp. 26–33, Jun. 2004, doi: 10.1016/S1369-7021(04)00286-X.

[41] S. Talam, S. R. Karumuri, and N. Gunnam, “Synthesis, Characterization, and Spectroscopic Properties of ZnO Nanoparticles,” *Int. Sch. Res. Netw. ISRN Nanotechnol.*, vol. 2012, 2012, doi: 10.5402/2012/372505.

[42] Y. Fei, Y. Li, Y. Li, A. Xie, Y. Li, and D. Sun, “Properties study of ZnO films prepared by ALD,” *J. Mol. Struct.*, vol. 1269, p. 133804, Dec. 2022, doi: 10.1016/J.MOLSTRUC.2022.133804.

[43] M. Kumar, H. Jeong, and D. Lee, “Nonvolatile memory devices based on undoped and Hf- and NaF-doped ZnO thin film transistors with Ag nanowires inserted between ZnO and gate insulator interface,” *RSC Adv.*, vol. 7, no. 44, pp. 27699–27706, 2017, doi: 10.1039/c7ra03460a.

[44] F. Farahbod and S. Farahmand, “Empirical investigation of heating and kinematic performance of ZnO Nano fluid in a heat pipe,” *J. Nanofluids*, vol. 6, no. 1, pp. 128–135, 2017, doi: 10.1166/jon.2017.1306.

[45] D. Kaur, A. Bharti, T. Sharma, and C. Madhu, “Dielectric Properties of ZnO-Based Nanocomposites and Their Potential Applications,” *Int. J. Opt.*, vol. 2021, 2021, doi: 10.1155/2021/9950202.

[46] F. X. Liang, Y. Gao, C. Xie, X. W. Tong, Z. J. Li, and L. B. Luo, “Recent advances in the fabrication of graphene–ZnO heterojunctions for optoelectronic device applications,” *J. Mater. Chem. C*, vol. 6, no. 15, pp. 3815–3833, Apr. 2018, doi: 10.1039/C8TC00172C.

[47] L. Zheng *et al.*, “Network structured SnO2/ZnO heterojunction nanocatalyst with high photocatalytic activity,” *Inorg. Chem.*, vol. 48, no. 5, pp. 1819–1825, Mar. 2009, doi: 10.1021/IC802293P/SUPPL_FILE/IC802293P_SI_001.PDF.

[48] M. T. Uddin *et al.*, “Nanostructured SnO2-ZnO heterojunction photocatalysts showing enhanced photocatalytic activity for the degradation of organic dyes,” *Inorg. Chem.*, vol. 51, no. 14, pp. 7764–7773, Jul. 2012, doi: 10.1021/IC300794J/SUPPL_FILE/IC300794J_SI_001.PDF.

[49] M.-C. Jeong *et al.*, “ZnO-Nanowire-Inserted GaN/ZnO Heterojunction Light-Emitting Diodes,” *Small*, vol. 3, no. 4, pp. 568–572, Apr. 2007, doi: 10.1002/SMLL.200600479.

[50] N. Park, K. Sun, Z. Sun, Y. Jing, and D. Wang, “High efficiency NiO/ZnO heterojunction UV photodiode by sol–gel processing,” *J. Mater. Chem. C*, vol. 1, no. 44, pp. 7333–7338, Oct. 2013, doi: 10.1039/C3TC31444H.

[51] S. Y. Tsai, M. H. Hon, and Y. M. Lu, “Fabrication of transparent p-NiO/n-ZnO heterojunction devices for ultraviolet photodetectors,” *Solid. State. Electron.*, vol. 63, no.

1, pp. 37–41, Sep. 2011, doi: 10.1016/J.SSE.2011.04.019.

[52] C. Luo, D. Li, W. Wu, Y. Zhang, and C. Pan, “Preparation of porous micro–nano-structure NiO/ZnO heterojunction and its photocatalytic property,” *RSC Adv.*, vol. 4, no. 6, pp. 3090–3095, Dec. 2013, doi: 10.1039/C3RA44670K.

[53] R. Kavitha and S. G. Kumar, “A review on plasmonic Au-ZnO heterojunction photocatalysts: Preparation, modifications and related charge carrier dynamics,” *Mater. Sci. Semicond. Process.*, vol. 93, pp. 59–91, Apr. 2019, doi: 10.1016/J.MSSP.2018.12.026.

[54] A. Sekkat, D. Bellet, G. Chichignoud, D. Muñoz-Rojas, and A. Kaminski-Cachopo, “Unveiling Key Limitations of ZnO/Cu 2 O All-Oxide Solar Cells through Numerical Simulations,” *ACS Appl. Energy Mater.*, vol. 5, no. 5, pp. 5423–5433, May 2022, doi: 10.1021/acsaem.1c03939.

[55] J. Holzl and F. K. Schulte, *Solid Surface Physics - Work Functions of Metals*. 1979. [Online]. Available: https://link.springer.com/content/pdf/10.1007%2FBFb0048918.pdf

[56] A. G. MASSEY, “COPPER,” in *The Chemistry of Copper, Silver and Gold*, vol. 630, Elsevier, 1973, pp. 1–78. doi: 10.1016/B978-0-08-018860-7.50006-2.

[57] D. H. Whittum, “Surface Physics Exercises in Quantum Mechanics,” *Physics (College. Park. Md).*, no. May, pp. 1–17, 2014.

[58] IUPAC, “Periodic-Table-of-Elements.” https://iupac.org/what-we-do/periodic-table-of-elements/ (accessed Jul. 22, 2022).

[59] N. Anyadike, “Copper A Material for the New Millennium,” in *Copper*, no. June 1996, Elsevier, 2002, pp. 1–26. doi: 10.1016/B978-1-85573-592-7.50004-7.

[60] International Copper Study Group, “The World Copper Factbook,” *Int. Copp. Study Gr.*, p. 63, 2020, [Online]. Available: http://www.icsg.org/

[61] M. Thompson, Ed., “Copper,” in *Base Metals Handbook*, 3rd ed., Woodhead Publishing, 2006, pp. 3-1-3–77. doi: 10.1016/B978-1-84569-154-7.50003-7.

[62] J.R. Davis, *METALS HANDBOOK*, 2nd ed. ASM International, 1998.

[63] E. T. George and D. S. MacKenzie, *Handbook of Aluminum: Physical Metallurgy and Processes*, 1st ed., vol. 1. CRC Press, 2003. doi: 10.1111/j.1939-0025.1969.tb02453.x.

[64] William F. Gale, *The physical properties of pure metals*, vol. cap14. 2004.

[65] J. Chanut *et al.*, “Surface properties of cork: Is cork a hydrophobic material?,” *J. Colloid Interface Sci.*, vol. 608, pp. 416–423, Feb. 2022, doi: 10.1016/J.JCIS.2021.09.140.

[66] A. N. Guerreiro and M. H. Braga, “Structural Cork in Ferroelectric Solid-State Devices by Scanning Kelvin Probe,” *MDPI*, 2022, doi: 10.3390/materproc2022008114.

[67] F. Danzi, M. Valente, and M. H. Braga, “Sodium and potassium ion rich ferroelectric solid electrolytes for traditional and electrode-less Sodium and potassium ion rich ferroelectric solid electrolytes for traditional and electrode-less structural batteries,” vol. 10, p. 31111, 2022, doi: 10.1063/5.0080054.

[68] “SKP Probes - Biologic.” https://www.biologic.net/accessory/skp-probes/ (accessed Jul. 10, 2022).

[69] S. Trasatti, “The Absolute Electrode Potential□: an Explanatory Note,” *Pure Appl. Chem.*, vol. 58, no. 7, pp. 955–966, 1986, [Online]. Available: http://iupac.org/publications/pac/58/7/0955/

[70] M. H. Braga, J. E. Oliveira, T. Kai, A. J. Murchison, A. J. Bard, and J. B. Goodenough, “Extraordinary Dielectric Properties at Heterojunctions of Amorphous Ferroelectrics,” *J. Am. Chem. Soc.*, vol. 140, no. 51, pp. 17968–17976, Dec. 2018, doi: 10.1021/JACS.8B09603/SUPPL_FILE/JA8B09603_SI_001.PDF.

Appendix

1.SKP experimental results of Cu/ZnO/Al heterojunctions

2.SKP Experimental results of Cu/ZnO/Zn heterojunctions

3.“Interfacial chemistry with ZnO: *in operando* work functions in hetero cells” article

1. SKP experimental results of Cu/ZnO/Al heterojunctions

“Cu_ZnO_Al” cell experiments

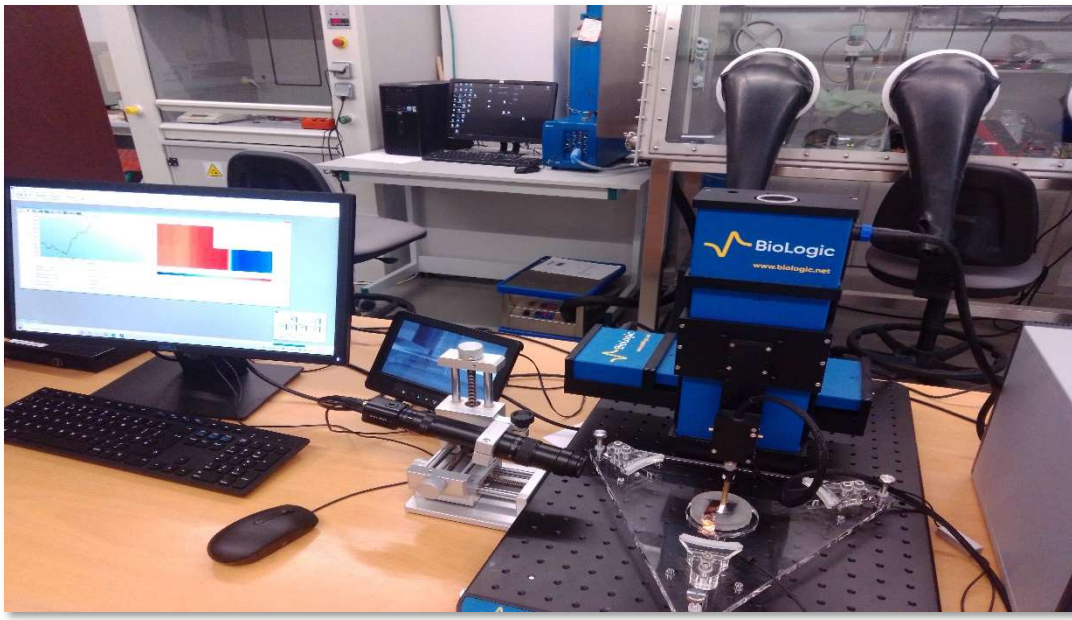

Cell "Cu ZnO Al" experiment

Data experiment 1

- Scan direction **: Cu --> ZnO--> Al**
- Approximate measurements of electrodes and ZnO: **Electrode Cu:** ~3.20mm; **óxide ZnO:** ~4.30mm; **Electrode Al**: ~4.50mm
- Connection to M470 through Cu electrode with Cu tape
- Calibration: copper
- Oxide gap dimensions: ~(22mm x 4.7mm); depth ~6mm;
- Scan area: 12,00mm x 0,15mm
- Distance tip-sample: 100 µm
- Potential between 2 electrodes, before the experiment 1: 0,065 V

Map Cu_ZnO_Al by CTM

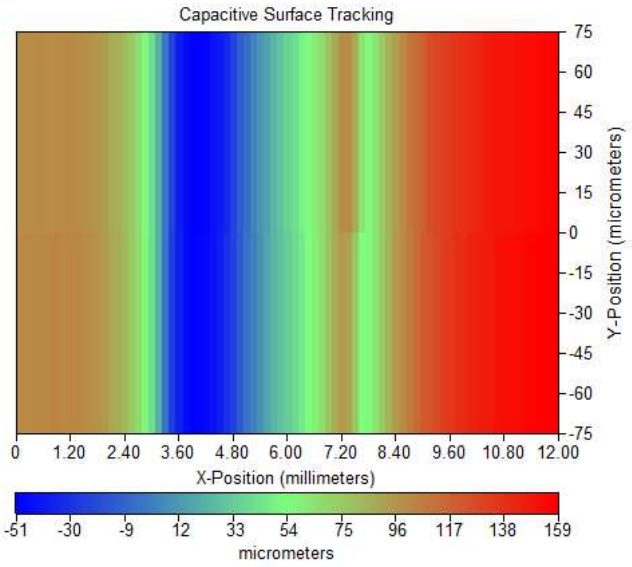

a)

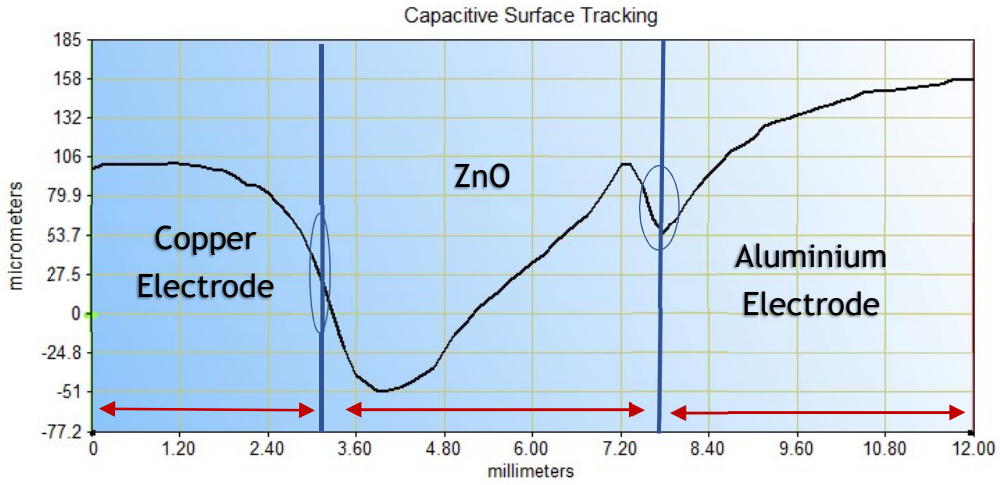

b)

Figure 1. a) Cu_ZnO_Al cell's topography obtain by CTM, experiment 1

b) Cu_ZnO_Al cell's graph by CTM, experiment 1

Experiment 1SKP1

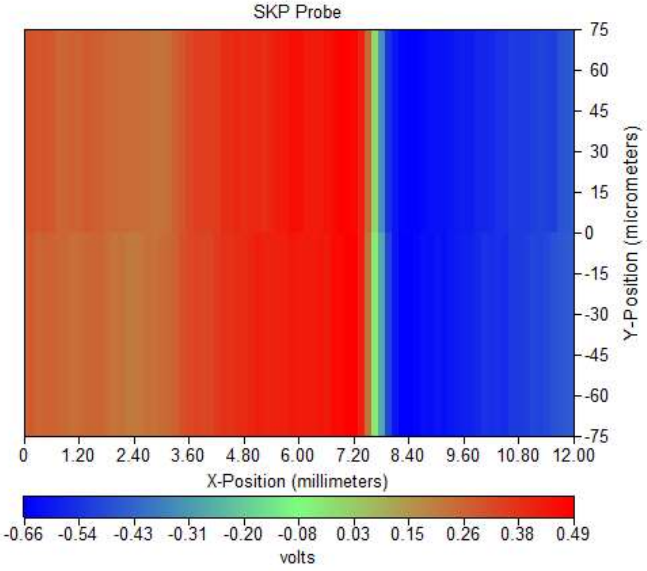

a)

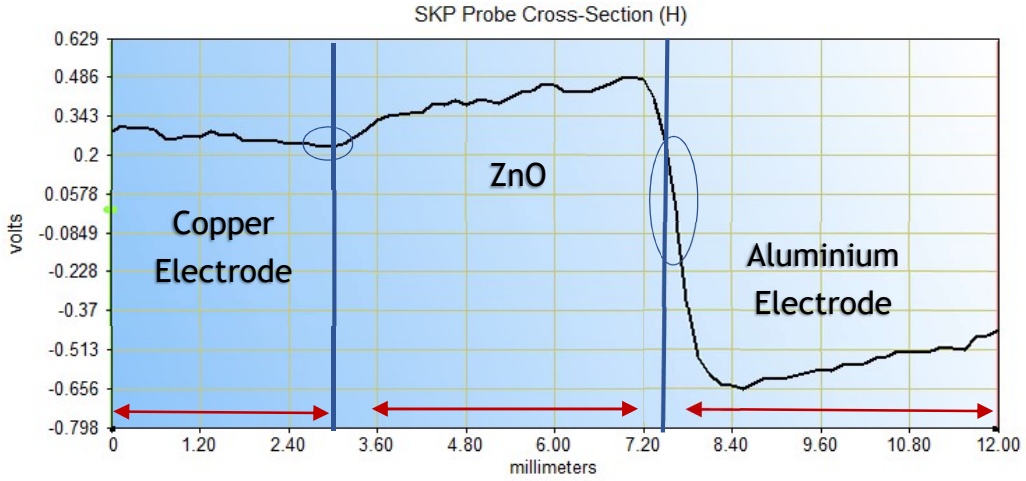

b)

Figure 2. a) Gradient of electrical potential of the Cu_ZnO_Al cell by **SKP1**, experience 1
b) Line of the electrical potential Cu_ZnO_Al cell by **SKP1**, experience 1

Experiment 1SKP2

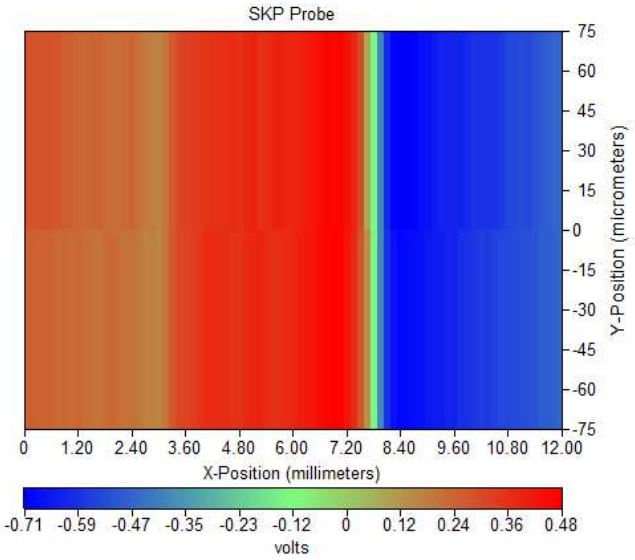

a)

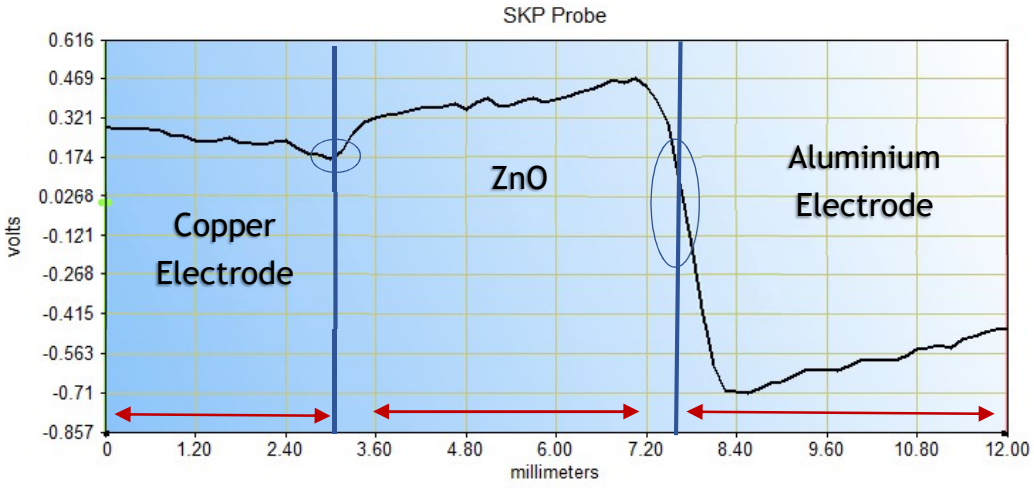

b)

Figure 3. a) Gradient of electrical potential of the Cu_ZnO_Al cell by **SKP2**, experiment 1
b) Line of the electrical potential Cu_ZnO_Al cell by **SKP2**, experiment 1

Figure 4. Cu_ZnO_Al cell

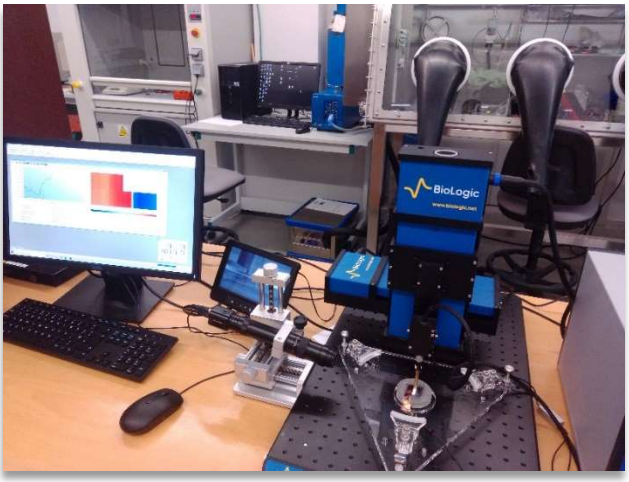

Figure 5. Cu_ZnO_Al cell, experiment 1

Experiment data 2

- Scan direction **: Cu --> ZnO--> Al**
- Approximate measurements of electrodes and ZnO: **Electrode Cu:** ~3,20mm; **Oxide ZnO:** ~4,30mm; **Electrode Al**: ~4,50mm
- Connection to M470 through Cu electrode with Cu tape
- Calibration: copper
- Oxide gap dimensions: ~(22mm x 4.7mm); depth ~6mm;
- Scan area: 12,00mm x 0,15mm
- Distance tip-sample: 100 µm
- Potential between 2 electrodes, before the experiment 1: 0,066 V

Map of the Cu_ZnO_Al cell by CTM

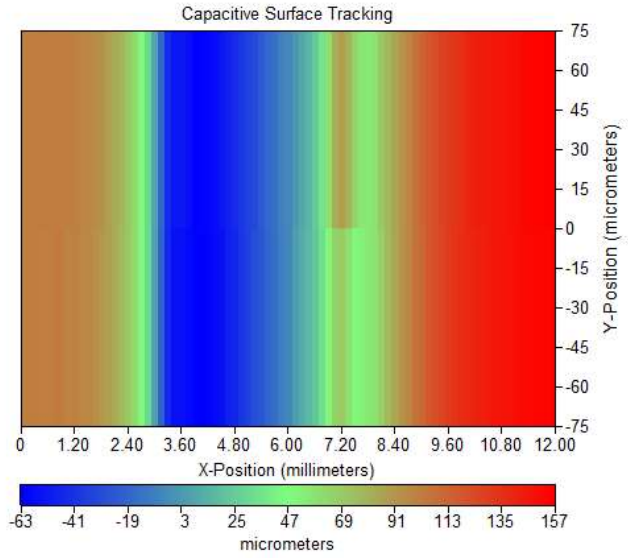

a)

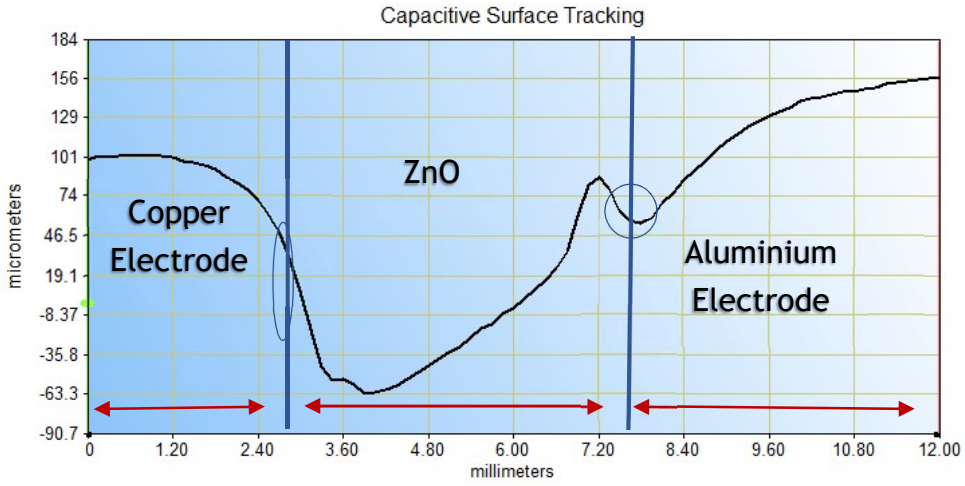

b)

Figure 6. a) Cu_ZnO_Al cell's topography obtain by CTM, experiment 2

b) Cu_ZnO_Al cell's graph by CTM, experiment 2

Experiment 2SKP3

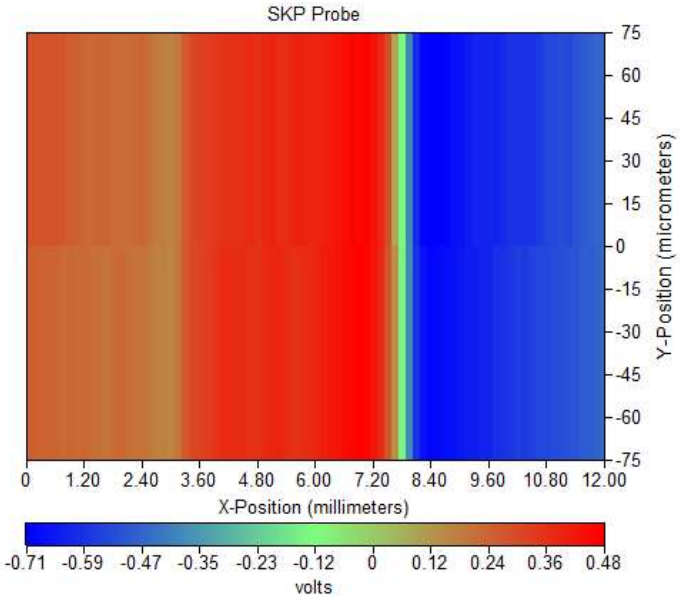

a)

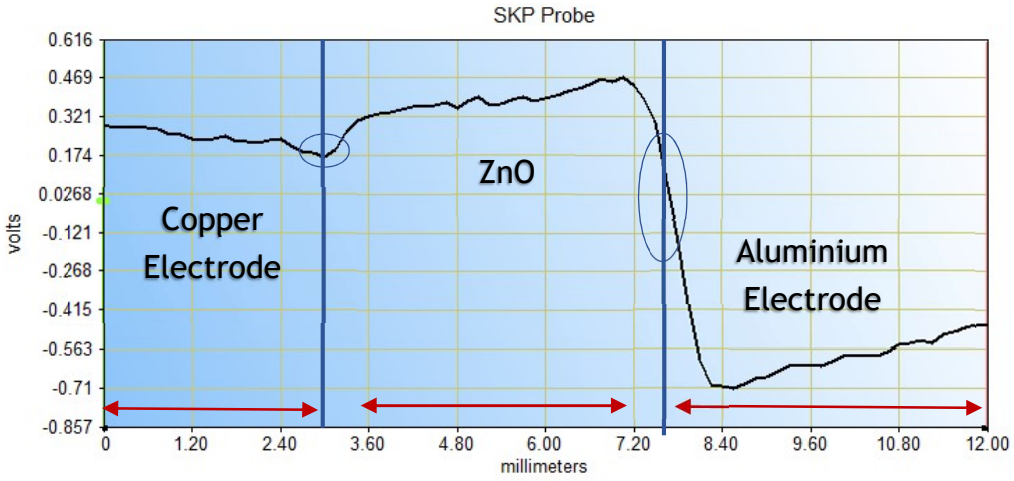

b)

Figura 7. a) Gradient of electrical potential of the Cu_ZnO_Al cell by **SKP3**, experiment 2
b) Line of the electrical potential Cu_ZnO_Al cell by **SKP3**, experiment 2

Experiment 2SKP4

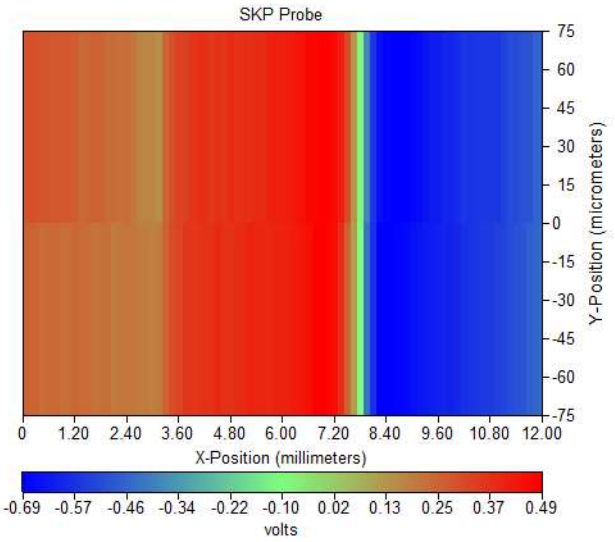

a)

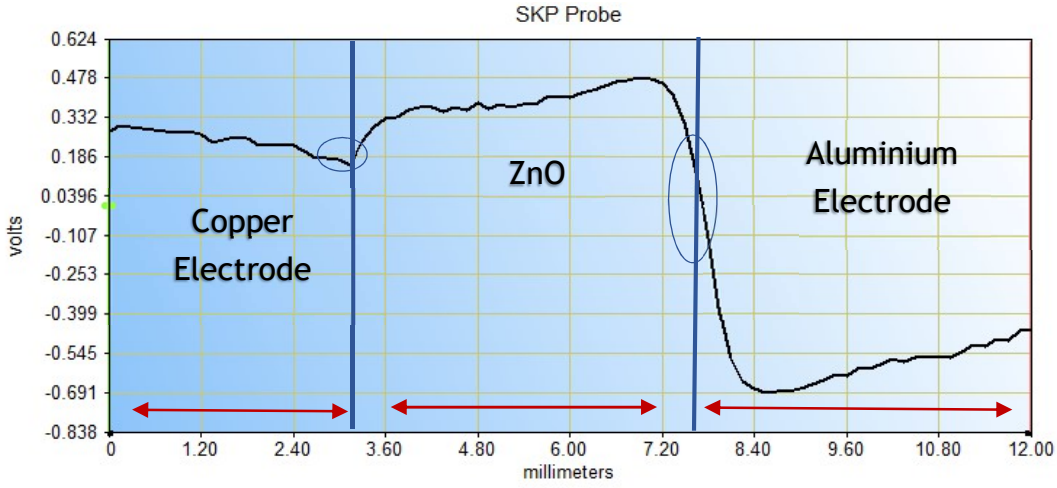

b)

Figure 8. a) Gradient of electrical potential of the Cu_ZnO_Al cell by **SKP4**, experiment 2
b) Line of the electrical potential Cu_ZnO_Al cell by **SKP4**, experiment 2

Experiment data 3

- Scan direction **: Al --> ZnO--> Cu**

- Approximate measurements of electrodes and ZnO: **Electrode Al:** ~4p50mm; **oxide ZnO:** ~4,30mm; **Electrode Cu**: ~3,20mm

- Connection to M470 through Al electrode with Al tape

- Calibration: copper

- Oxide gap dimensions: ~(22mm x 4.7mm); depth ~6mm;

- Scan area: 12,00mm x 0,15mm

- tip-sample: 100 µm

Map of the Al_ZnO_Cu Cell by CTM

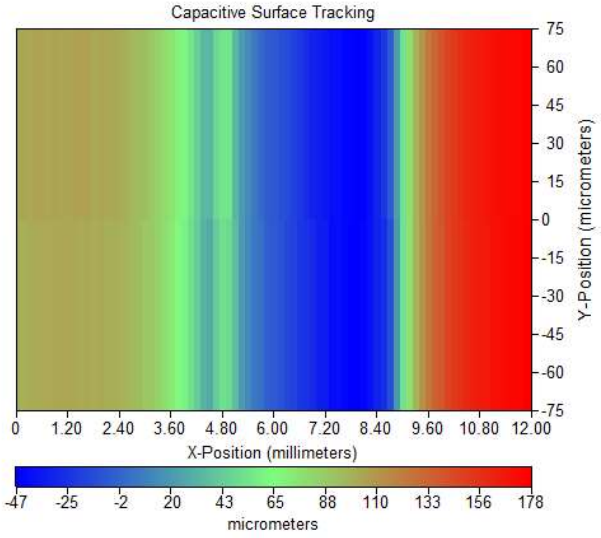

a)

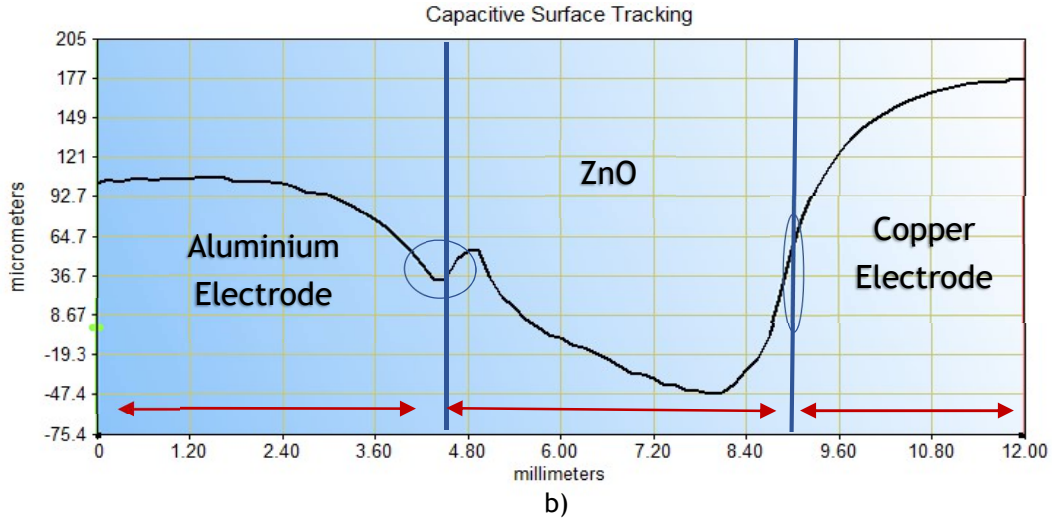

b)

Figure 9. a) Cu_ZnO_Al cell's topography obtain by CTM, experiment 3

b) Cu_ZnO_Al cell's graph by CTM, experiment 3

Experiment 3SKP5

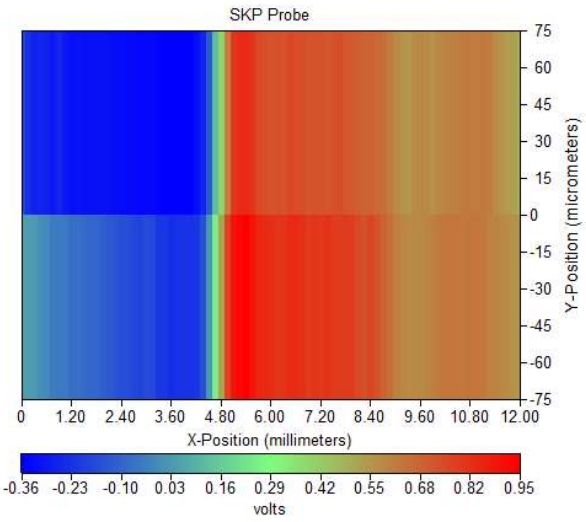

a)

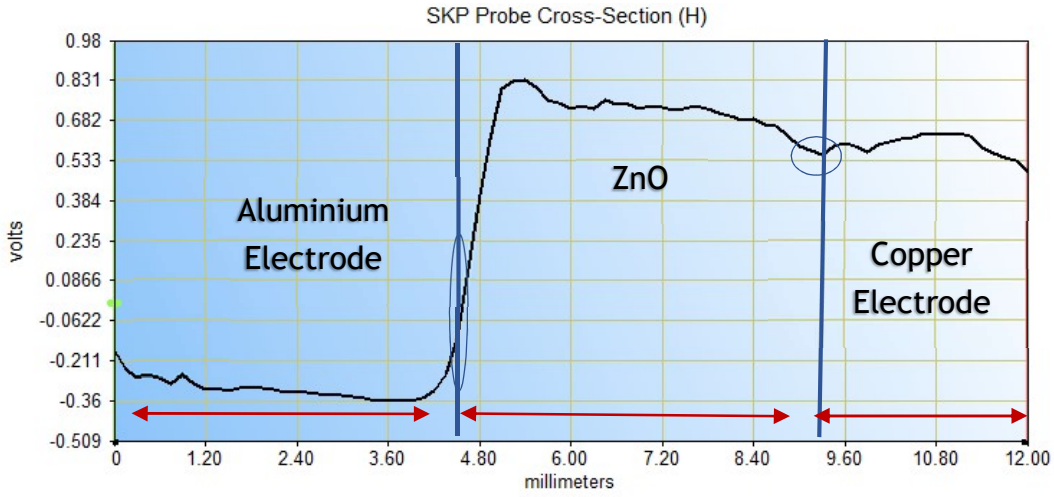

b)

Figure 10. a) Gradient of electrical potential of the Cu_ZnO_Al cell by **SKP5**, experiment 3
b) Line of the electrical potential Cu_ZnO_Al cell by **SKP5**, experiment 3

Experiment 3SKP6

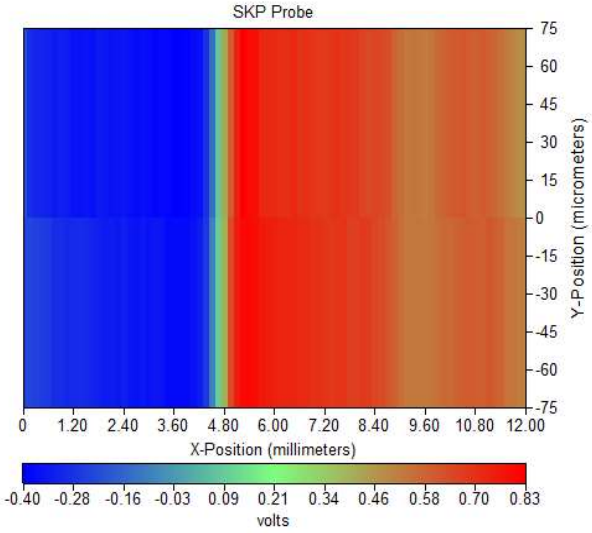

a)

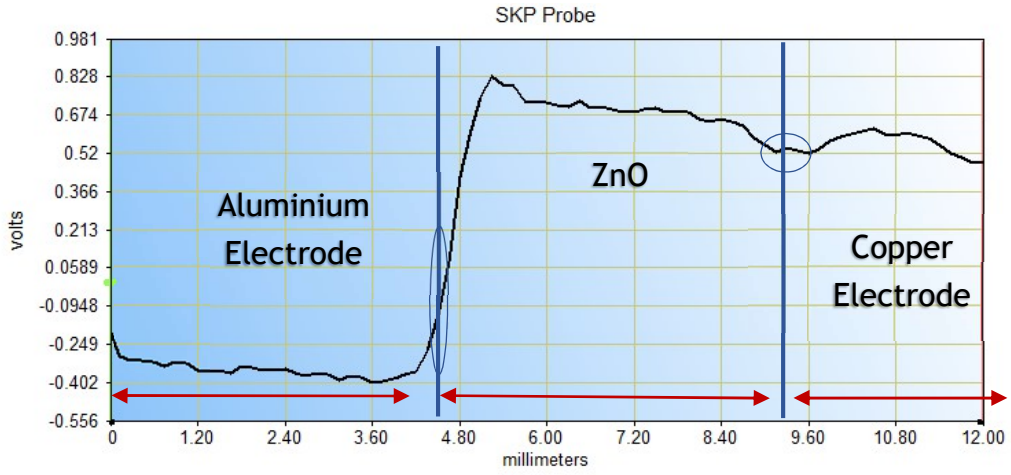

b)

Figure 11. a) Gradient of electrical potential of the Cu_ZnO_Al cell by **SKP6**, experiment 3
b) Line of the electrical potential Cu_ZnO_Al cell by **SKP6**, experiment 3

Experiment 3SKP7

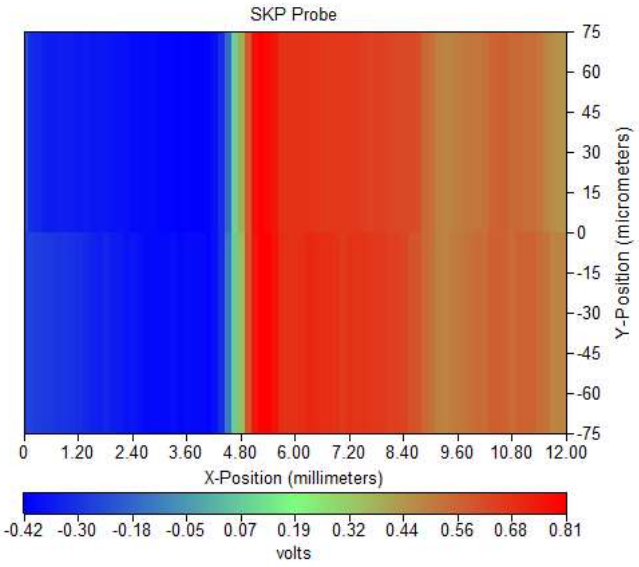

a)

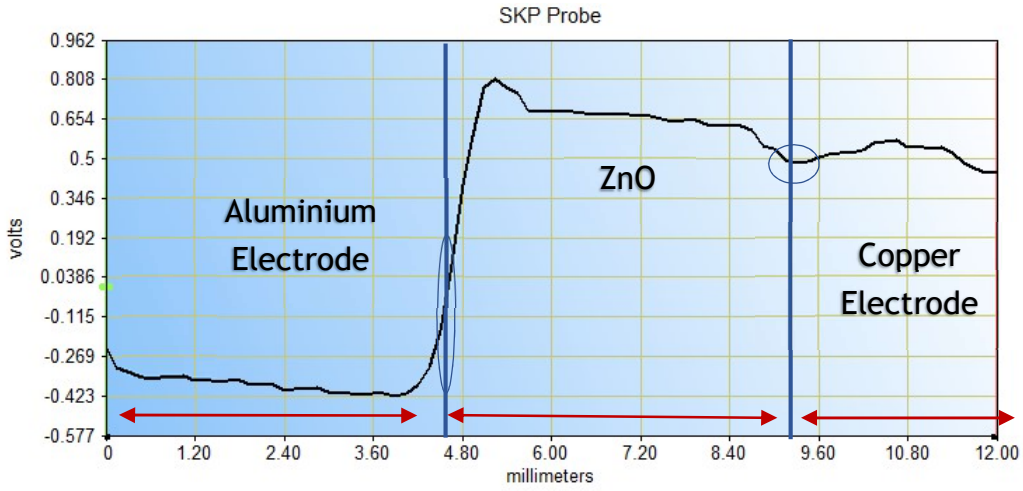

b)

Figure 12. a) Gradient of electrical potential of the Cu_ZnO_Al cell by **SKP7**, experiment 3
b) Line of the electrical potential Cu_ZnO_Al cell by **SKP7**, experiment 3

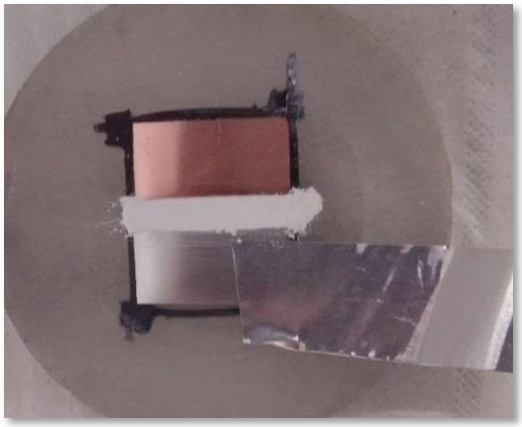

Figure 13. Al_ZnO_Cu cell before the experiment 3

2. SKP experimental results of Cu/ZnO/Zn heterojunctions

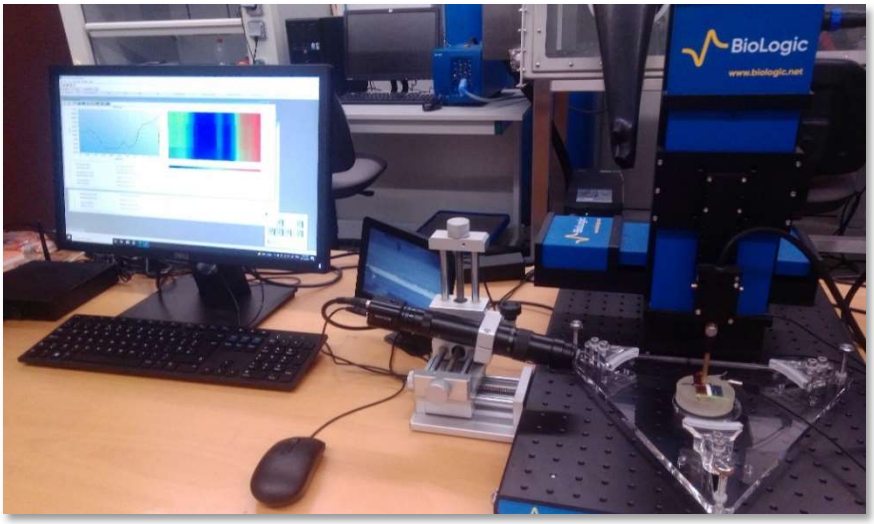
BioLogic
www.biologic.net

“Cu_ZnO_Zn” cell experiments

Experiments data 1

- Scan direction : **Cu --> ZnO--> Zn**
- Approximate measurements of electrodes and ZnO: **Electrode Cu:** ~5.10mm; **oxide ZnO:** ~5.20mm; **Electrode Zn**: ~2.80mm
- Connection to M470 through Cu electrode with Cu tape
- Calibration: copper
- Oxide gap dimensions: ~(20mm x 5mm); depth ~6mm;
- Scan area: 12.00mm x 0.15mm
- Tip-sample distance: 100 µm

Map Cu_ZnO_Zn by CTM1

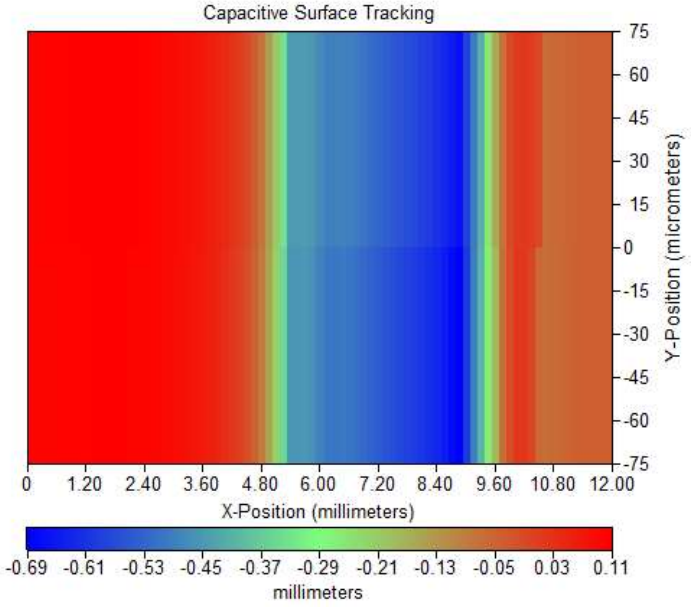

a)

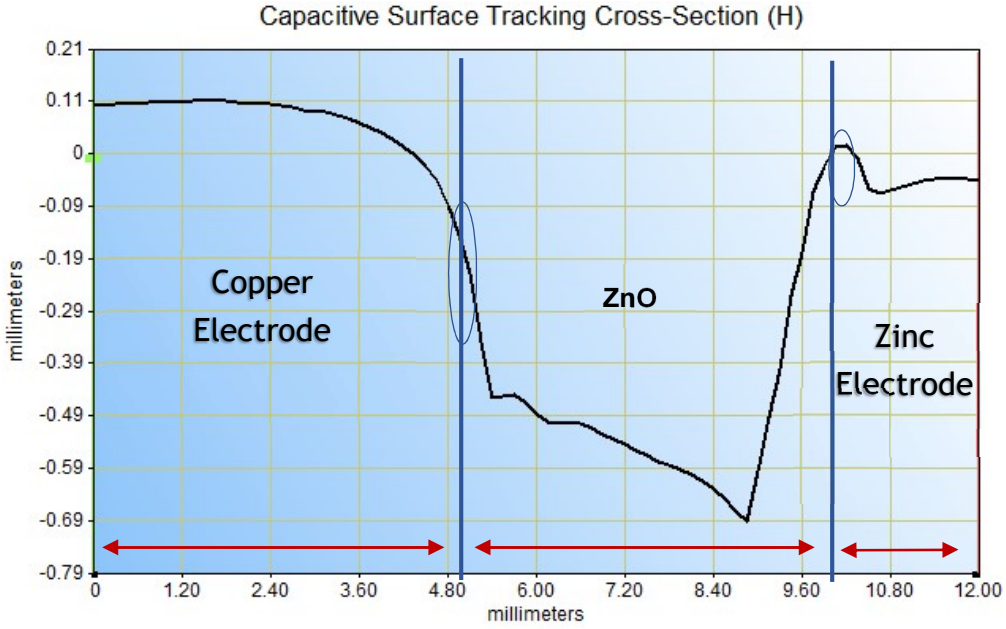

b)

Figure 1. a) Cu_ZnO_Zn cell's topography obtain by CTM1, experiments 1

b) Cu_ZnO_Zn cell's graph by CTM1, experiments 1

Experiments 1SKP1

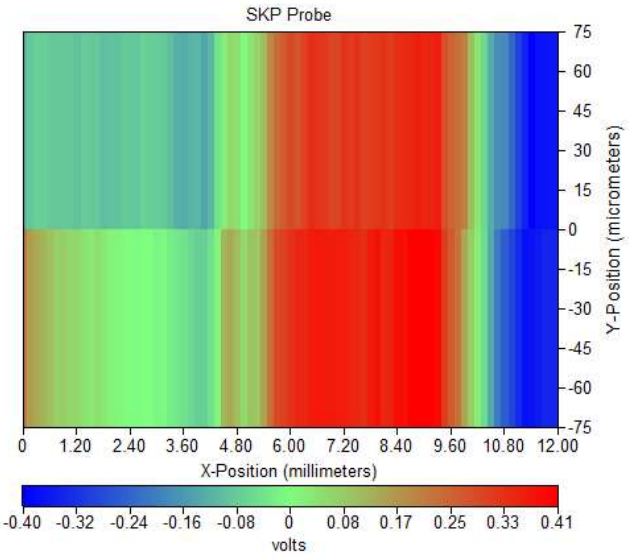

a)

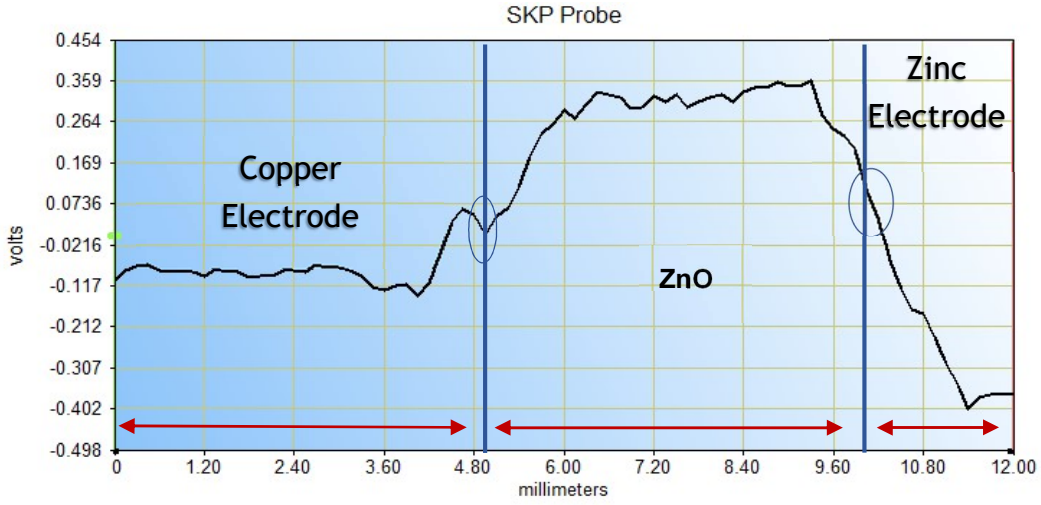

b)

Figure 2. a) Gradient of electrical potential of the Cu_ZnO_Zn cell by **SKP1**, experiments 1
b) Line of the electrical potential Cu_ZnO_Zn cell by **SKP1**, experiments 1

Experiments 1SKP2

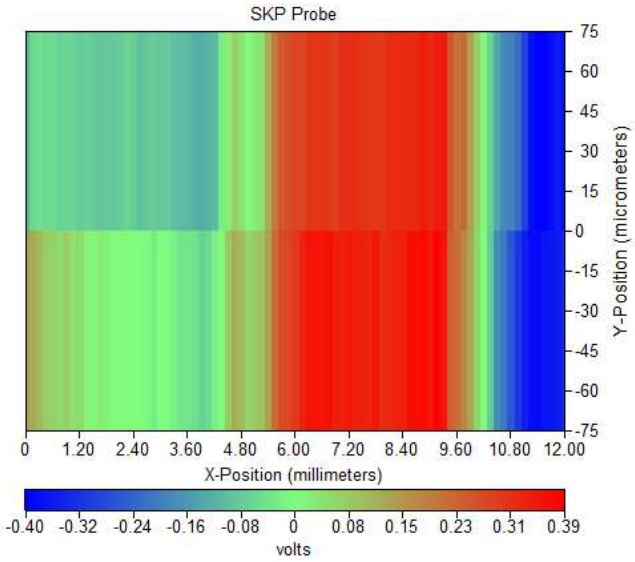

a)

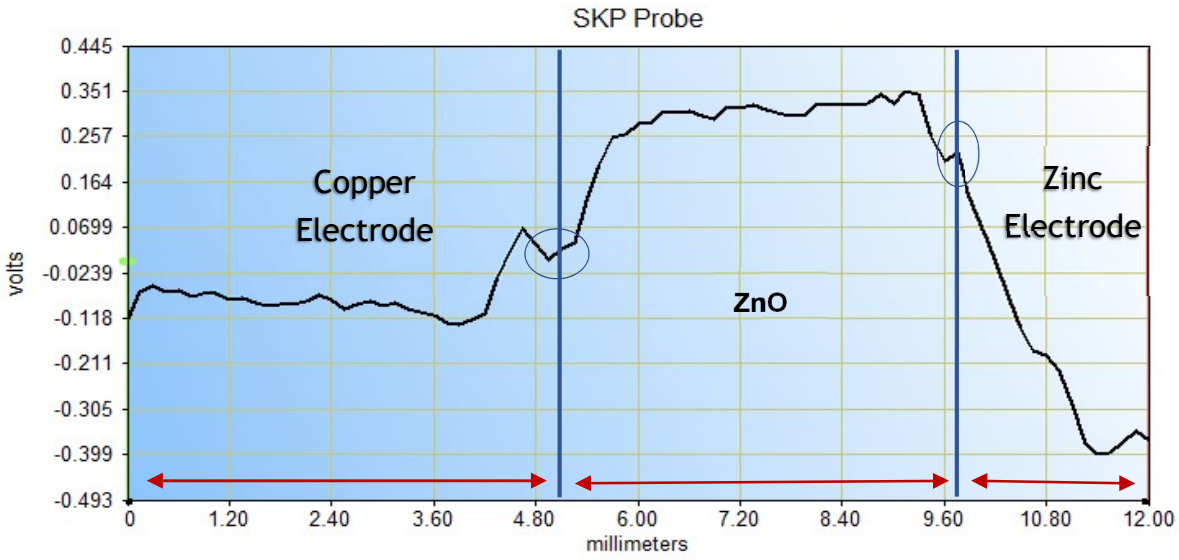

b)

Figure 3. a) Gradient of electrical potential of the Cu_ZnO_Zn cell by **SKP2**, experiments 1
b) Line of the electrical potential Cu_ZnO_Zn cell by **SKP2**, experiments 1

Map of the Cu_ZnO_Zn cell by CTM2

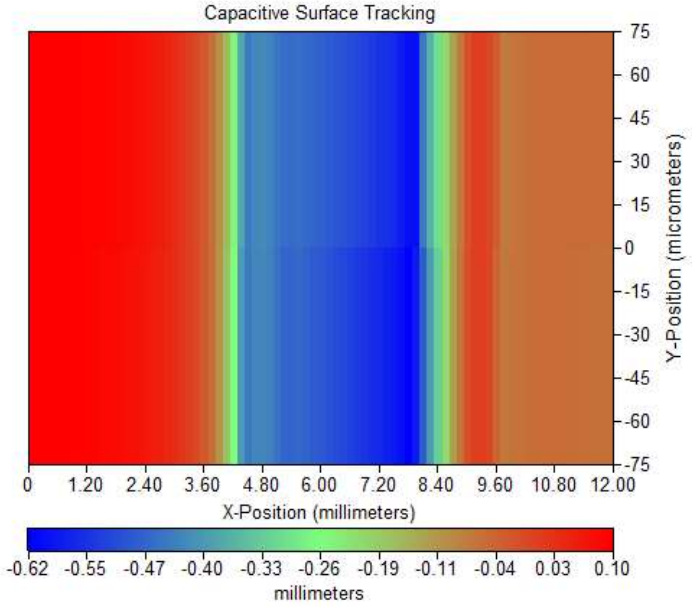

a)

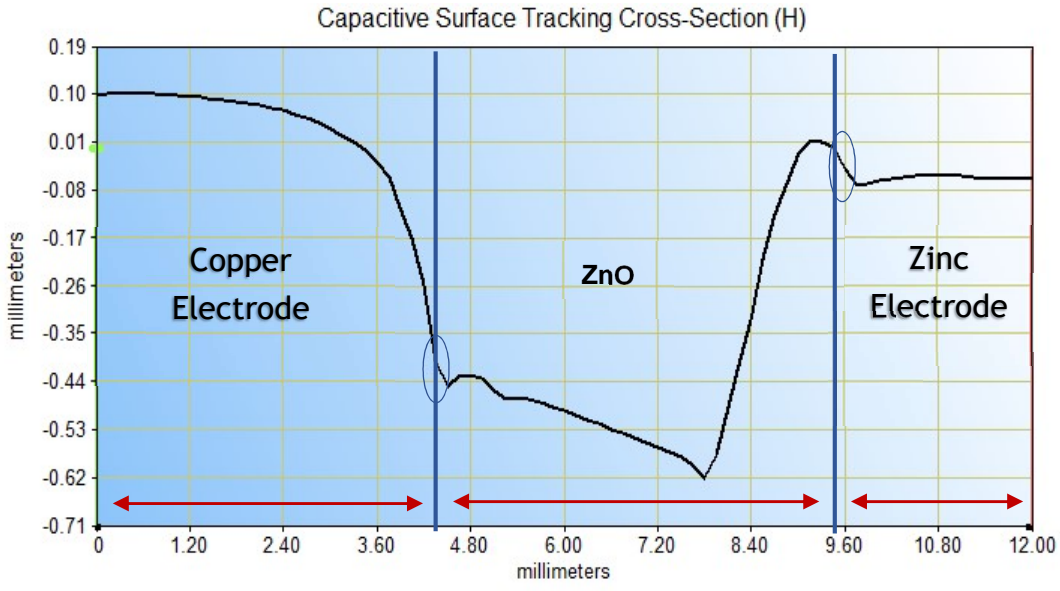

b)

Figure 4. a) Cu_ZnO_Zn cell's topography obtain by CTM2, experiments 2

b) Cu_ZnO_Zn cell's graph by CTM2, experiments 2

Experiments 2 SKP3

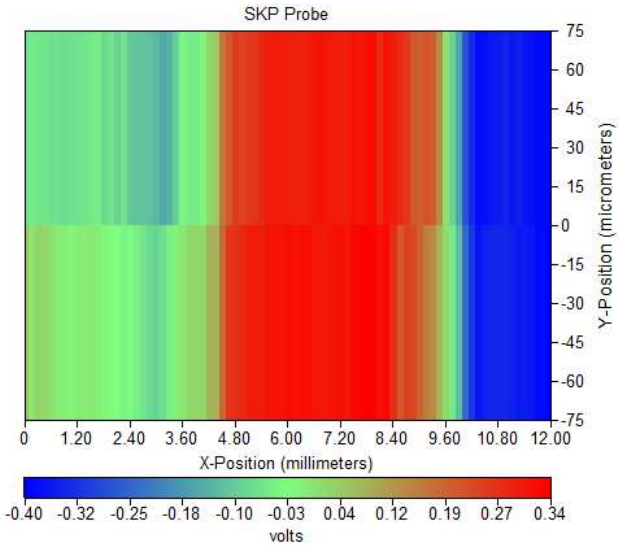

a)

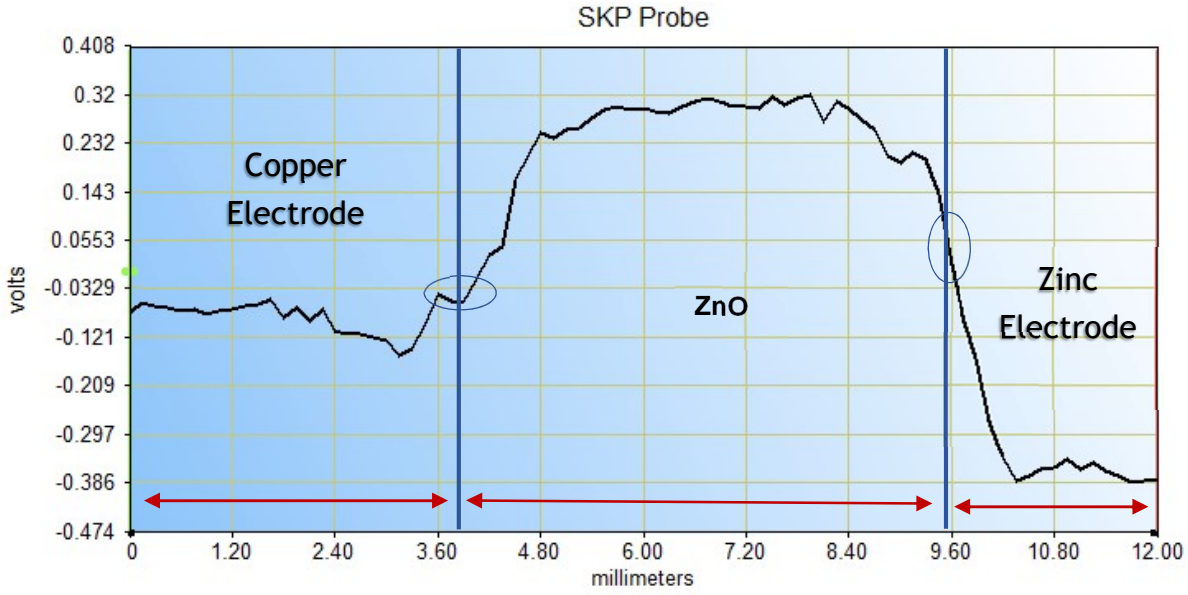

b)

Figure 5. a) Gradient of electrical potential of the Cu_ZnO_Zn cell by **SKP3**, experiments 2

b) Line of the electrical potential Cu_ZnO_Zn cell by **SKP3**, experiments 2

3. “Interfacial chemistry with ZnO: *in operando* work functions in hetero cells” article

Interfacial chemistry with ZnO: *in operando* work functions in hetero cells

A. Nuno Guerreiro[1], Manuela C. Baptista[1], Beatriz A. Maia[1,2], M. Helena Braga[1,2,*]
[1]Engineering Physics Department, Engineering Faculty, University of Porto, 4200-465 Porto, Portugal
[2]LAETA - INEGI, Institute of Science and Innovation in Mechanical and Industrial Engineering, 4200-465 Porto, Portugal
*Correspondence: mbraga@fe.up.pt

Abstract: Interfacial additives such as oxides may help solve diffusion and nucleation obstacles in heterojunctions of solid-state devices. Healing strategies may rely on them, particularly in ZnO, which has numerous applications, from photovoltaics and sensors to superconductors and batteries as a lithiumphilic interlayer. Here we show a case study based on *in operando* cells with two heterojunctions and the ZnO as a dielectric semiconductor. The cells show how the Cu/ZnO surface chemical potentials equalize by forming a more negatively charged region where nucleation of a new phase will likely be facilitated and the dielectric's role in interlaying with negative and positive electrodes. The highly ohmic behavior of the interface, negative electrode (metal) /dielectric, is also analyzed. The advantage of the Scanning Kelvin Probe (SKP) in studying the surface chemical potentials is demonstrated. *Ab initio* simulations used DFT and hybrid functional HS06 to determine the bulk ZnO's band structure and optical properties, including relative permittivities. Aluminum, zinc, copper, and zinc oxide *work functions* were obtained after simulating the correspondent surfaces and compared with contact potentials obtained with SKP. The study extends hyperbolically into the cell's dimensions to understand all the interplays of the components. An unexpected long-range equalization of the surface chemical potentials of the three cell constituents away from the interfaces may mirror a metal-insulator-metal plasmonic interaction that can be tailored for solar applications.

1. Introduction

As the electrical revolution tends to transform society, different solutions stand out for solving the energy storage problems associated with replacing fossil fuels with an electrical equivalent. This surge is aggravated by the need to compensate for the daily fluctuations in energy harvesting as the grids are not dimensioned to accommodate these fluctuations.

New and greener energy sources have been extensively studied in the last years. Li-ion batteries (LIB) enabled the wireless technologies market to ascend [1], paving the way for the electrification revolution. Lithium-ion is the most desired mobile ion as lithiated anodes and cathodes allow higher energy density. However, lithium is not widely available [2], and in both brine and mineral formulations, environmental challenges arise in extraction and refinement processes.

Lithium metal reacts readily with air and needs to be handled in an inert atmosphere. However, lithium metal is the desired anode as its theoretical capacity is 3860 $mAh.g^{-1}$ [3]. The Li anode allows for the use of the total capacity of cathodes, such as sulfur, as the electrode which defines the battery cell's capacity is the one with the lowest capacity. Sulfur

(S_8, 1675 $mAh.g^{-1}$), which has a much higher capacity than the cathode materials in Li-ion batteries, may be fully employed in Li-S batteries [4]. The latter batteries are being developed with solid-state electrolytes, as solid-state cells are not flammable, allowing for the use of Li and preventing sulfides' shuttle, another problem in Li-S batteries [5]–[7].

Research on Li-ion and Li batteries is partially focused on avoiding wasting lithium and on fabrication processes that do not rely on inert atmospheres. It is under such a scenario that anode-less Li batteries assume particular relevance. A current collector is employed in this case, and no Li metal is incorporated in the initial assembly [8].

Anode-less Li batteries, where the lithium anode is plated from an all-solid-electrolyte onto the current collector, do not waste Li and may allow for the fabrication of batteries without recurring to air-free environments. Anode-less batteries, however, may introduce other drawbacks besides those associated with solid-state batteries. If the electrolyte is not Li^+ rich, the cathode's capacity decreases even further than it usually does in Li batteries. Additional Li may be irreversibly lost while plating on the anode current collector. Moreover, copper, which is used as Li current collector, is not lithiumphilic, difficulting the Li plating. Therefore, the challenge is to plate Li homogeneously onto the collector with no or reduced losses. For achieving this goal, an interfacial material that allows for nucleation and homogeneous deposition of the Li is paramount. Healing properties are also highly appreciated to increase batteries' cycle life. Here, we study ZnO that may enhance lithium nucleation and enable the tailoring of efficient anode-less current collectors.

1.1 Interfacial engineering

Interfacial engineering is lately assuming more importance as batteries become solid. Recently, Tong et al. [9] reviewed interfacial chemistry in anode-less batteries, focusing on the low columbic efficiency and dendrite formation resolution. Interfacial problems, such as heterogeneous Li coating, interfacial parasitic reactions, and the presence of dead lithium, were addressed. The study and analysis of interfacial chemistry with the fabrication of an inorganic layer on the anode current collector to reinforce the interface and reduce the nucleation barrier to increase the adhesion of Li on this surface was analyzed by C. Heubner et al. [10].

Here, we study ZnO and ZnO/metal heterojunctions (i.e., Al, Cu, and Zn) that may be used to tailor anode-less current collectors. Nonetheless, zinc oxide has numerous applications that are hereafter partially reported.

1.1.1 Zinc oxide (ZnO)

In 2010 Ozgur et al. [11] studied ZnO devices and applications, highlighting that it is a material with suitable properties for electronics, photonics, acoustics, and sensing. Zinc oxide

can be used in transparent thin-film transistors (TFTs) because of its high optical transmittance and conductivity. At the same time, ZnO may have an advantage over other semiconductors because it has a high exciton binding energy (60 meV), an asset for optical emitters. Added to this is its possible applicability in acoustic wave devices. Zinc oxide has an excellent electromechanical coupling with devices that use nanowires/nanorods such as biosensors, gas sensors, and solar cells; these ZnO nanostructures are relatively easy to produce giving them good charge transport properties and high crystalline quality.

Liang et al. [12] remarked on the importance of ZnO as a binary semiconductor, consisting of elements of group II and VI of the periodic table, with a sizeable direct bandgap (3.37 eV) at room temperature. The fabrication of graphene/ZnO hybrid heterostructures using high or low-temperature methods was reviewed, as well as the applications of graphene/ZnO in various optoelectronic devices such as photodiodes, phototransistors, solar cells, light-emitting diodes (LED), and lasers. Other heterojunctions were also subject to different studies with ZnO, as according to the respective applications, there are benefits in using different tandem materials, such as CuO/ZnO [13], SnO_2/ZnO [14], [15], GaN/ZnO [16], NiO/ZnO [17]–[19] and Au/ZnO [20]. Very recently, Sekkat et al. [21] unveiled the external quantum efficiency of the Cu_2O/ZnO solar cells as a function of interface defects and side/double side illumination. Electron transport occurs from Cu_2O to ZnO, and hole transport in the opposite direction within Cu_2O. These findings are related to the present work.

1.1.2. ZnO dielectric properties

As already mentioned, ZnO is a trustworthy choice in several applications, from semiconductors to photoconductivity. Zinc oxide shows a large bandgap where the most common doping happens due to interstitial zinc sites and oxygen voids and relies on its ionic character. Moreover, ZnO oxide is classified as an intrinsic n-type semiconductor when excess electrons create a donor band, assisting the electron in jumping to the conduction band [22]. In this case, the intrinsic n-type conductivity of ZnO is followed by a high electron density of 10^{21} cm^{-3} [23].

However, ZnO can also be classified as a piezoelectric material. Piezoelectrics are dielectric materials with a twist; they allow the existence of a polarizing electrostatic field in response to applied mechanical stress along with the [0001]-direction because of their noncentrosymmetric structure; ultimately, ZnO possesses a charge storage capability [24]. Zinc oxide also exhibits pyroelectric properties; it can polarize and maintain inner electric fields in response to temperature variations.

Materials can be subdivided considering the value of their relative real permittivity (ε'_r), high-ε'_r materials ($\varepsilon'_r > 7$), and low-ε'_r materials ($\varepsilon'_r < 3.9$). Look and co-workers [25]

assessed the relative real permittivity of the bulk ZnO to be $\varepsilon'_r = 8$ at 1 MHz and room temperature, while Langton et al. [26] found a ε'_r value of 10.4 from 1 MHz to 10 MHz. Other values were obtained when varying the thickness of the film or even the particles size.

1.1.3 ZnO in energy storage devices

Artificially engineering the copper-current collector surface is one of the strategies to extend the life of anode-less batteries. Specifically, in the case under study, the aim is to obtain a homogeneous and stable lithiumphilic surface.

Lithium ions diffuse into the copper sheet through the grain boundaries, and therefore, if the Cu sheet is used as a current collector, the alloying reaction may occur. A limitation that results from the latter is that dendritic Li grows from the grain boundaries with a 3D fractal structure. A possible via to avoid dendrite growth is to modify the current collector surface with wetting agents, such as nanoparticles, as these cause the surface tension to decrease. Consequently, the deposition of Li becomes uniform. Thus, by using agents such as Al, Au, Ag, C, Mg, Pt, Si, Sn, and Zn, it is possible to decrease the nucleation overpotential of Li and, consequently, control the deposition of Li on a lithiumphobic substrate [9]. In addition, ZnO nanoparticles (<500 nm) prevent passivation and allow full utilization of the active materials [27]. Studies by Y. Liu et al. [28] take an interesting approach, a lithium metal anode design by infusing molten lithium into a polymer matrix; they use a ZnO coating to make the surface lithiumphilic.

Kumar Pandey et al. [29] reviewed the general applications of ZnO as an n-type nanostructured semiconductor because of its unique and tuneable properties. With optimum chemical and thermal stability, ZnO holds numerous applications in supercapacitors, lithium-ion batteries, and dye-sensitized solar cells; ZnO-based nanostructures have excellent potential as electrode materials in LIBs and supercapacitors. Finally, Zhang et al. [30] studied the ZnO@TiN_xO_y core/shell nanorod structure for rechargeable Zn anodes.

2. Methods

2.1. Electrochemical potential and EDLC

The electrochemical potential of specie i, $\bar{\mu}_i{}^{\alpha}$, in a phase α with charge z_i, can be calculated as expressed in Equation 1,

$$\bar{\mu}_i{}^{\alpha} = \mu_i{}^{\alpha} + z_i F \phi_i{}^{\alpha} \quad (1)$$

where $\mu_i{}^{\alpha}$ represents the chemical potential of i in the α phase, F is the Faraday constant, and $\phi_i{}^{\alpha}$ the surface potential of i specie, also in the α phase [31].

When two species, i and j, establish electrical contact, their electrochemical potential will reach an equilibrium where the electrochemical potential of both species will be the same, as represented in Equation 2.

$$\bar{\mu}_i - \bar{\mu}_j = 0 = \left(\mu_i - \mu_j\right) - z_i F(\phi_j - \phi_i) \Leftrightarrow \mu_i - \mu_j = z_i F(\phi_j - \phi_i) \quad (2)$$

Considering the specific case where i species are electrons, ${\bar{\mu}_e}^{\alpha}$ is called the Fermi level and corresponds to the electron energy level. The Fermi level can be considered equal to the chemical potential only if the material is isolated and ${\phi_i}^{\alpha} \approx 0$.

Bearing this in mind, Equation 2 gives essential information about what will happen at the interfaces metal/ZnO. Since ZnO becomes an intrinsic n-type semiconductor due to the presence of defects, such as Zn interstitials, polarization by ionic diffusion is likely. In fact, ZnO is a piezoelectric and a pyroelectric, as stated before. It is then possible to align the chemical potentials at the interfaces by ionic polarization, forming a double-layer capacitor (EDLC), and the exchange of electrons may or may not occur depending on ohmic or Schottky barriers.

At the negative electrode/dielectric interface (ZnO), the difference in chemical potentials is $\mu_{(-)} - \mu_{ZnO} = e\Delta V_{(-),ZnO}$; therefore, when the internal resistance is negligible, the difference in chemical potentials is compensated by forming an electrical double-layer capacitor (EDLC) that "brings" the electrochemical potentials to alignment or equalization. When the internal resistance is not negligible, the energy stored at the interfacial EDLCs is partially, or all, spent in this resistance, the equalization of the electrochemical potentials does not occur, and the voltage of the cell is $\Delta V = \frac{(\mu_{i(-)} - \mu_{ZnO})}{e} + \frac{(\mu_{ZnO} - \mu_{(+)})}{e} - (R_i I)_{total}$. If diffusion or drift of electrons occurs, the chemical potentials equalize by variation of the chemical potentials with the possible formation of an interphase. Variations in the composition, such as gradients, will also reflect the variation in the chemical potentials.

2.2 Scanning Kelvin Probe (SKP)

The Scanning Kelvin Probe (SKP) is a non-invasive technique derived from the Atomic Force Microscopy (AFM) and allows the electrochemical study of the materials' surface, especially conductors. In this study, the SKP was used to determine the *work function* of materials and cells. In particular, the equalization of the Fermi levels (electrochemical potentials) [32] between sample and probe (Figs. 1a to 1c), which is the working principle of the SKP, our focus and a novel approach presented for the study of energy storage cells [33]-[35]

The SKP technique allows for analyzing the surface's contact potentials difference (CPD) on a micrometrical scale. In this work, it was used capacitive tracking measurement (CTM) to

scan the surfaces. The cells (Figs. 1d and 1e) had flat surfaces with a reduced slope that could be observed when the examined surface was a couple of centimeters-squared. The CTM is a height tracking technique that maintains a constant distance between the SKP's probe tip and the sample. The probe "follows" the surface without losing proximity information. The distance chosen for this study between the tip and the sample was 100 μm, with CTM and SKP monitored through a micro camera.

All SKP measurements were performed with a Biologic SKP-M470 with two U-SKP370 probe tips of tungsten wire with diameters of 500 μm and 150 μm [36]. The electrical contact between the CTM/SKP and the cells was made either through the positive (Cu) or negative electrodes (Al, Zn). For both Cu and Al, tapes of the corresponding materials were used in order to avoid an additional heterojunction.

In summary, with the SKP measurements, it was possible to obtain: **(1)** contact potential differences within a cell; **(2)** the *work function* of each material in the cell; **(3)** the materials' topographies; **(4)** capacitance of the cells; **(5)** *in operando* behavior of a solid-state cell.

The Fermi levels, or electrochemical potentials, of the sample $\bar{\mu}_{sample}$ and SKP tip $\bar{\mu}_{SKP}$, their vacuum energies $E_{V,sample}$ and $E_{V,SKP}$, and *work functions* χ_{sample} and χ_{SKP} relate to the chemical potentials μ_{sample} and μ_{SKP} and surface potentials ϕ_{sample} and ϕ_{SKP} (Figs. 1a to 1c) through the equation,

$$\begin{aligned}\bar{\mu}_{sample} - \bar{\mu}_{SKP} &= \left(E_{V,sample} + \chi_{sample}\right) - \left(E_{V,SKP} + \chi_{SKP}\right) \\ &= \left(\mu_{sample} - \mu_{SKP}\right) - z_i F(\phi_{SKP} - \phi_{sample})\end{aligned} \tag{3}$$

When $E_{V,sample} - E_{V,SKP} = 0$ and $\phi_{sample} - \phi_{SKP} = 0$, the sample and probe tip have the same vacuum level and are electrically insulated from each other and other materials,

$$\bar{\mu}_{sample} - \bar{\mu}_{SKP} = \chi_{sample} - \chi_{SKP} = \mu_{sample} - \mu_{SKP} \tag{4}$$

In the above circumstances, the SKP shows the chemical potential of the sample ZnO in each scanned region. When the sample is in electrical contact with other materials, it contains trapped charges and manifests catalytic, corrosion, or band bending phenomena, affecting its *work function*. Hereafter, the output potentials are designated surface chemical potentials and account for surface and chemical potentials.

It is noteworthy that the tip or cantilever of the SKP oscillates with a certain frequency, and therefore, the bias applied voltage is DC with an AC component.

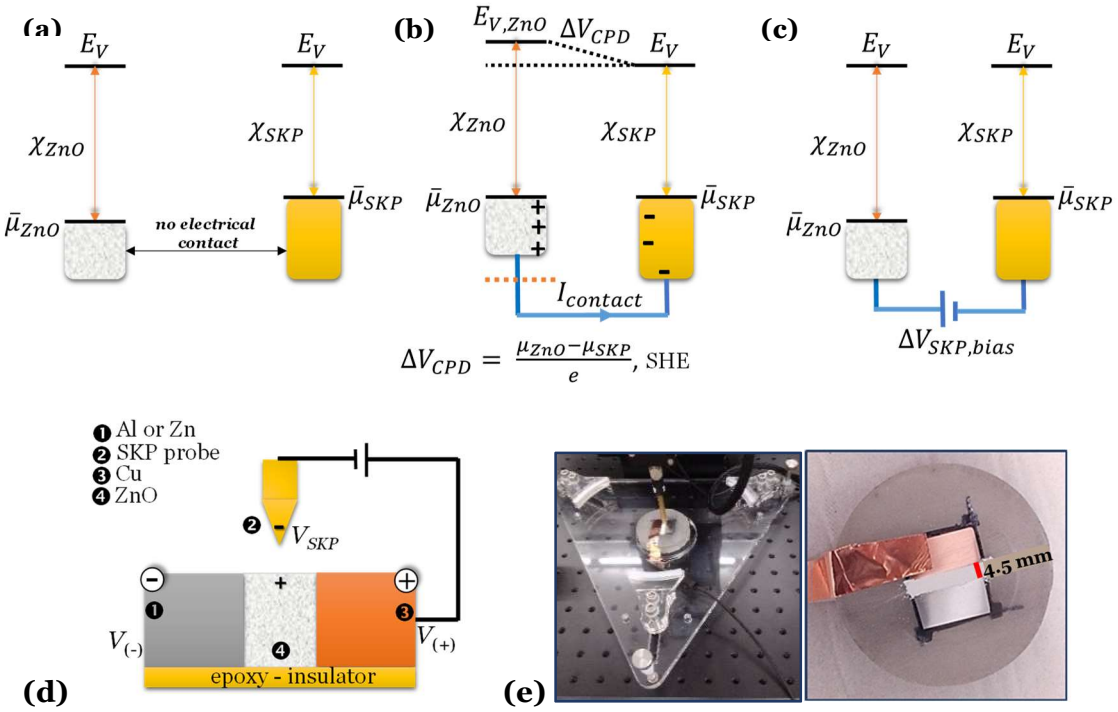

Figure 1. Working principle of the SKP. **(a)** sample (ZnO) and probe tip of the SKP with no electrical contact; **(b)** the sample gets in electrical contact with the SKP tip. The difference in vacuum levels between sample (ZnO) and tip (SKP) is equal to the contact potential difference (CPD); **(c)** the amplifier of the SKP applies a bias potential difference to the ZnO//SKP circuit ($\Delta V_{SKP,bias} = -\Delta V_{CPD}$); **(d)** schematics of the cell, probe tip, and $\Delta V_{SKP,bias}$; **(e)** photo of the SKP apparatus and cell. Note that the bias voltage $\Delta V_{SKP,bias}$ is DC and AC.

2.3 Electrical Impedance Spectroscopy (EIS)

Yatskiv et al. [37] studied the optical and electrical characterization of CuO/ZnO heterojunctions, employing EIS experiments. The authors have shown that the highly resistive depletion layer defined the electrical transport and the sensing properties of CuO and ZnO structures at the interface.

Impedance spectroscopy is a dynamic technique where a voltage perturbation (AC) is applied to a system, and the amplitude/phase shift of the response is measured [38]. This technique is widely used to obtain the equivalent circuits comprising the previous components. This method can be seen as a powerful tool for understanding the distributed capacitive, inductive, and resistive properties and ion transport [39]. The impedance corresponding to the equivalent circuit,

$$Z(\omega) = Re[Z(\omega)] - jIm[Z(\omega)] \quad (5)$$

where $Re[Z(\omega)]$ and $-Im[Z(\omega)]$ are the real and imaginary components of the impedance $Z(\omega)$ [40] as a function of the frequency ω.

Here, the EIS technique is useful for understanding the bulk and interfacial mechanisms in the ZnO heterojunctions; EIS was performed in a frequency range of 1 MHz to 0.1 Hz with an amplitude signal of 10 mV at room temperature to determine the resistance to charge transport in ZnO and Al/ZnO/Cu cell (Fig. 1e).

In the Nyquist plot obtained with EIS, the resistance R and capacitance C of two non-ideal capacitors were minimized and calculated, taking into account the series between two capacitors, being each one in parallel with a resistor, as shown hereafter. The capacitors' components correspond to species with natural frequency $\leq 10^6$ Hz (i.e., interfacial space charge, ions, and low-frequency dipoles). The capacitor in the Nyquist plot, consistent with the semi-circle at a higher frequency, corresponds to the cell Al/ZnO/Cu, where Zn^{2+} ions are free to move in the bulk ZnO. The capacitor at lower frequencies may relate to a chemical interaction occurring at the interface Cu/ZnO where Zn^{2+} accumulates to compensate for the difference in chemical potentials with the copper that charges negatively. This latter chemical interaction may rely on a Cu oxide layer, i.e., CuO/ZnO or Cu_2O/ZnO, where electrons tunnel from the copper electrode to the conduction band of ZnO. Nonetheless, the calculated resistances only represent an order of magnitude, as the impedances are too scattered and too high for meaningful calculations.

2.4 *Ab initio* simulations

The surface properties of ZnO are critical in determining the activity of the material, and in this respect, Wander and Harrison [41] studied ZnO ($10\bar{1}0$) by *ab initio* simulations. Ren et al. [42] also performed *ab initio* simulations of lattice constants and lattice stabilities of ZnX (X = O, S, Se, Te) at different electronic temperatures using the pseudopotential method of Generalized Gradient Approximation (GGA) within the DFT. Ellmer and Bikowski [43] restated that one of the limitations in DFT model calculations is the underestimation of the fundamental difference of the ZnO band (E_g = 3.4 eV) with calculated bandgap values ranging from 0.4 to 3.77 eV [44].

In this work, we have used VASP6 (Vienna Ab initio Simulation Package), a framework of the Density Functional Theory (DFT), and hybrid functional HSE06 packages, from which structural and electric properties were optimized [45], [46], with plane-wave cutoff of >400 eV, reciprocal space projection, and spacing of k points of 0.3 $Å^{-1}$. *Ab initio* simulations were performed with simplified, schematic representations of complex physical systems without defects like stacking faults, vacancies, antisites, or impurities. Nonetheless, Frenkel and Schottky defects, essential to describe the n-type semiconductor ZnO, may be simulated as in [47].

Local Density (LDA) and Generalized Gradient Approximations (GGA) underestimate the band gap E_g, significantly, which translates into difficulty in calculating the absolute positions

of the defect and donor levels relative to the valence or conduction band edges [48]. As highlighted in [2], the hybrid functional HSE06 is more suitable for simulating the electric properties of semiconductors such as ZnO. Here we have optimized the wurtzite structure of ZnO, hexagonal $P6_3mc$ space group, using DFT, and the electrical properties (including band structure) and optical properties using DFT and HSE06.

The surfaces of ZnO, Al, Cu, and Zn were also simulated to determine the *work functions* from the total average potentials. The planar and macro potentials were obtained; the latter was integrated of over 10 Å for the determination of the macroscopic average. The *work functions* were calculated using the macro potentials by making the difference between the maximum (potential of the electrons at rest on the surface) and the average potential at the middle point between the minimum and maximum potentials immediately before and after the line that marks the surface.

2.5 Materials

Zinc oxide, 99.99 %, powder with diameters < 74 μm from Alfa Aesar, was used as dielectric material. The oxide based cells were fabricated with two different metal electrode pairs (copper/aluminium and copper/zinc) disjoined by a ZnO-powders filled gap (Fig. 1e), which is the object of study (Fig. 1d). The electrodes were fixed on epoxy support. Before beginning the calibration procedures on SKP, the cell is prepared following the process: (1) sand and polish the electrodes; (2) thoroughly clean the particles residues; and (3) fully dry the cell. After that, the cell is ready to be filled with oxide powder in the gap between the electrodes, tightly compressed, and leveled by the electrodes. The oxide is also fully dry. The materials under study have the following dimensions:

Al/ZnO/Cu: Al with (10 × 22 × 4.7) mm^3; ZnO with (4.5 × 22 × 4.7) mm^3; Cu with (10 × 22 × 4.7) mm^3. Zn/ZnO/Cu: Zn with (10 × 20 × 6.3) mm^3; ZnO with (5 × 20 × 6.3) mm^3; Cu with (10 × 20 × 6.3) mm^3. The cell is then filled in a humidity-controlled box and connected to the SKP-M470 (Fig. 1e). As stated before, tapes of the same materials that connected to the SKP were used to avoid an additional heterojunction.

3. Results and Discussion

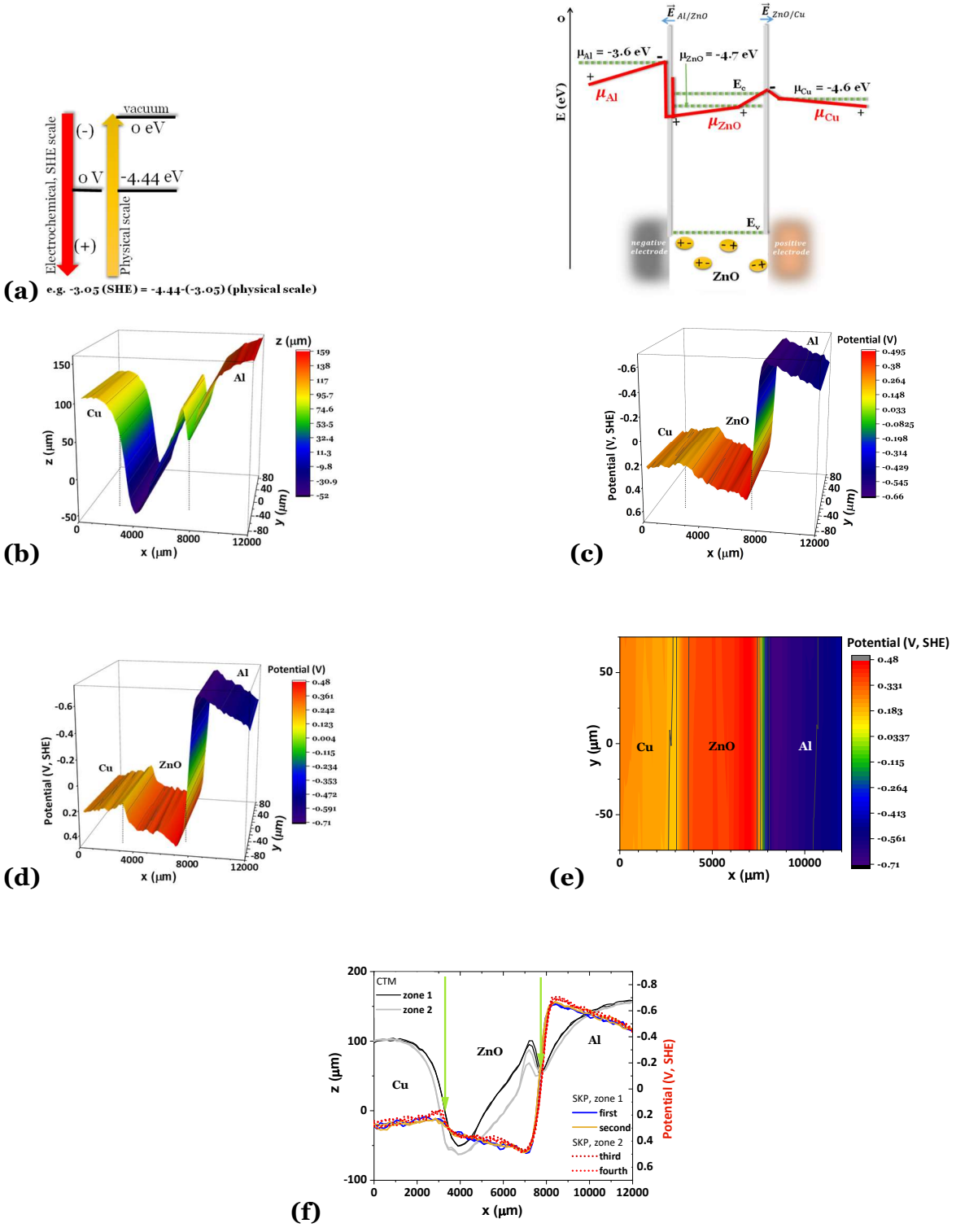

Figure 2 Topography and electrochemical potentials for an Al/ZnO/Cu cell when the CTM/SKP circuit is closed through the Cu; **(a)** Schematic representation of the SHE to Physical scale for the absolute chemical potentials and a schematics on the electric and dielectric structure of the cell before the components are put into contact (dotted lines) and while being measured as a cell with SKP (full lines), having the ZnO as an insulator with intrinsic n-type semiconductor capabilities. Although the ZnO is 99.99% pure, Zn^{2+} diffusion, or hydrogen absorption from moisture likely transform ZnO into an intrinsic n-type semiconductor; **(b)** CTM analysis of the topography of the surface of the cell; **(c)** and **(d)** SKP plots of the cell made with a ~40 min interval showing the surface almost does

not change. The cell is electrically connected to the SKP via the Cu. The surface chemical potentials of the Cu and Al show a substantial gradient, especially the Al; the Cu seems to align its electrochemical potential with the ZnO as the small peak observed is likely an EDLC with associated charge gradients; **(e)** 2D plot demonstrating the sharp transition from -0.66 to 0.48 V, highlighting the internal resistance (quantum well) correspondent to an almost opened circuit at the ZnO/Al interface. A cell showing no resistance or surface oxides could theoretically show a potential difference of [μ_{Al}-$\mu_{Cu} = \frac{1.66-(-0.34)}{e} \approx 2$ V]. The cell shows an OCV ΔV_{oc} = 0.065 V; **(f)** CTM and SKP consecutive experiments with time intervals of 30-40 min corresponding to two different zones of the cell.

To try to clarify the discussion of the results, it is noteworthy that in 1986, a publication from IUPAC [49] analyzed the conversion between the absolute chemical potentials scale, having as reference the standard hydrogen electrode (SHE), and the Physical scale having as reference the electrons at rest in vacuum at 0 eV (Fig. 2a). The absolute chemical potential energy measured from vacuum corresponds to the *work function* when the surface potential is $\phi_i = 0$. This equivalence is essential in this work, in which work functions, surface, absolute chemical potentials, and electrochemical potentials are correlated with contact difference potentials.

The AFM measurements with the surface topography's capacitive tracking (CTM) (Fig. 2b) are taken into account by the instrument in the SKP measurements; in other words, the topography does not influence the SKP results.

A good coating material to serve as a nucleation center for Li plating should not introduce resistance to the cell and transport electrons from the current collector to the Li^+-ions. With different cells Al/ZnO/Cu and Zn/ZnO/Cu and recurring to an SKP and different scanning lengths of 1.2 to 2.2 cm, we demonstrated the dielectric character of the oxide, likely enhanced by the ionic diffusion of Zn^{2+}. We have also shown the ZnO internal resistance in cell likely reflects the incapacity to align its electrochemical potential with the negative electrode (e.g., Figs. 2c to 2f and 3). While at the Cu/ZnO heterojunction there is a continuity of the surface chemical potential with a slight accumulation of negative charge at the interface (Figs. 2c to 2f and 3a and 3b), at the ZnO/Al side, there is a discontinuity or a step increase of the surface potentials possible corresponding to a potential well (Fig. 2a schematics of the cell) where electrons have a reduced probability to tunnel through. Nevertheless, although the voltage in the terminals of the bulk cell is reduced at open circuit (OCV) to ΔV_{oc} = 0.065 V, the cell's internal circuit is not fully open because, not only the bulk voltage can be registered, but the impedance can be determined (Fig. 3c).

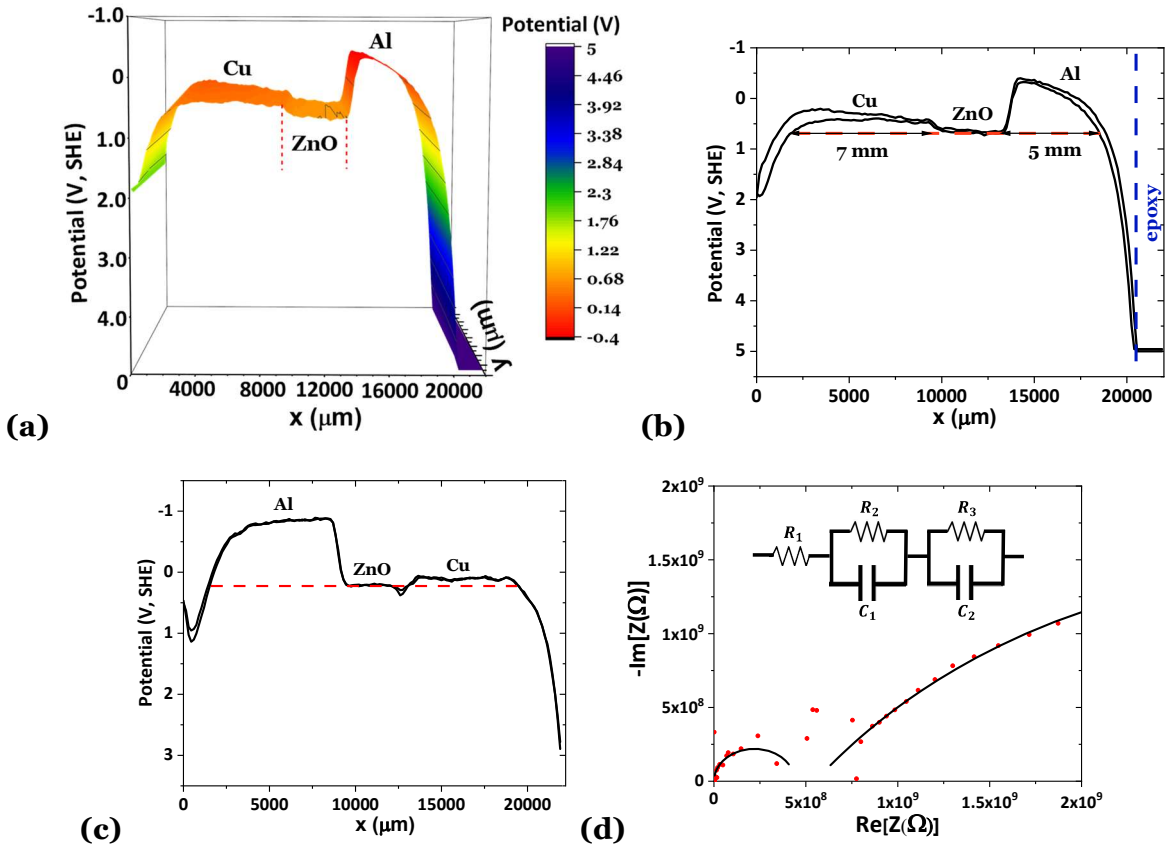

Figure 3 An Al/ZnO/Cu cell when the CTM/SKP circuit is closed through the Cu **(a)** and **(b);** and through the Al **(c)**. **(a)** and **(b)** extended scan of 2.2 cm approaching the epoxy at the Al end; alignment of the surface chemical potentials at the Cu/ZnO heterojunction and discontinuity at the ZnO/Al heterojunction corresponding to a highly resistive element; it is noteworthy that the surface chemical potentials equalize at least in three points within the cell: ~2.1 mm from the epoxy on the Al side and ~1.8 mm from the first data point on the Cu side; **(c)** SKP is connected to the cell through the Al; **(d)** EIS to determine the internal resistance and capacitance of the Al/ZnO/Cu cell at ~20°C. Equivalent circuit showing R_2 = 4.6×10⁷ Ω.cm, C_1 = 2.6 pF.cm$^{-1,}$ which are of the order of magnitude of the internal resistance and capacitance of the cell. Note that the metals, and especially Al, show a wide range of surface chemical potentials.

Pure ZnO is a semiconductor with an experimental band gap of 3.37 eV [12]. In Figure 3c, bending of the surface chemical potential of ZnO at the ZnO/Cu interface may indicate accumulation of Zn^{2+} ions (more positively charged region). It is known that ZnO, due to its ionic character, may quickly turn into an n-type intrinsic semiconductor by the formation of oxygen vacancies or by the action of the hydrogen in the water (or moisture), besides the occupation of interstitial sites by Zn^{2+} as pointed before. All the possible processes imply giving up electrons to the donor band.

The SKP plots show considerable stability, highlighted by the minimal variations in the experiments in different points in time (Figs. 2f and 3c).

Experiments with the SKP and Al/ZnO/Cu (Figs. 3a to 3c) and Zn/ZnO/Cu cells show an evident disruption of the surface potential at the interfaces Al/ZnO and Zn/ZnO, as shown hereafter. The step decrease in the electrochemical potentials, possibly indicating the presence of an impedance (internal resistance) due to a potential well, makes the alignment

of the electrochemical potentials or Fermi levels of Al/ZnO and Zn/ZnO at the interfaces impossible; nevertheless, points laying on the red dashed lines (Figs. 3b and 3c), while away from the edges of the cell show an equalization of the surface chemical potentials of the ZnO with Al and Cu (~2.1 mm from the epoxy on the Al side, and ~1.8 mm from the first data point on the Cu side). From the best of our knowledge, this is a novel result. We have not observed this same equalization in cells of the type $Al/Li_{2.99}Ba_{0.005}ClO/Cu$ (Support Information SI, Fig. S1); but other cells such as $Al/Al_2O_3/Cu$ (SI, Fig. S2) and $Al/Li_2O/Cu$ (SI, Fig. S2), show similar behavior.

The potential difference at open circuit (OCV) of the Al/ZnO/Cu cell, before and after the experiments, indicates that the cell is highly resistive ($\Delta V_{OC,before} = 0.065$ V and $\Delta V_{OC,after} = 0.066$ V). Considering the experimental $\left|\frac{\mu_{(Al)}-\mu_{(Cu)}}{e}\right| = 1.13$ eV (SKP) and using the potential, $\Delta V = \left|\frac{\mu_{(Al)}-\mu_{(Cu)}}{e}\right| - (R_i I)_{total} = 0.07$ V $\Leftrightarrow R_i = 0.46 \times 10^7$ Ω or $R_i = 0.23 \times 10^7$ Ω.cm, which is in reasonable agreement with the approximate resistance obtained by EIS, $R_2 = 4.6{\times}10^7$ Ω.cm (Fig. 3d). The cell rested for 12 h at ~20°C before the analysis. However, the impedance is very high, and the data suffer from scattering, so the experimental resistance obtained by EIS, calculated using the equivalent circuit in Fig. 3d, is not as reliable as desirable.

The capacitance ($C = 0.8$ pF) was calculated for the dimensions of the cell, $A = (2.2 \times 0.47)$ cm^{-2}, $d = 0.45$ cm (Figs. 1d) and dielectric constant ($\varepsilon'_r = 4$) obtained using *ab initio* (HSE06 functional) and shown later. Compared with the capacitance obtained with EIS ($C_1 = 6$ pF), the theoretical capacitance is one order of magnitude lower. The difference might be attributed to the HSE06 functional simulated relative permittivity or to the EIS data scattering due to extreme difficulty in measuring very high resistances with EIS.

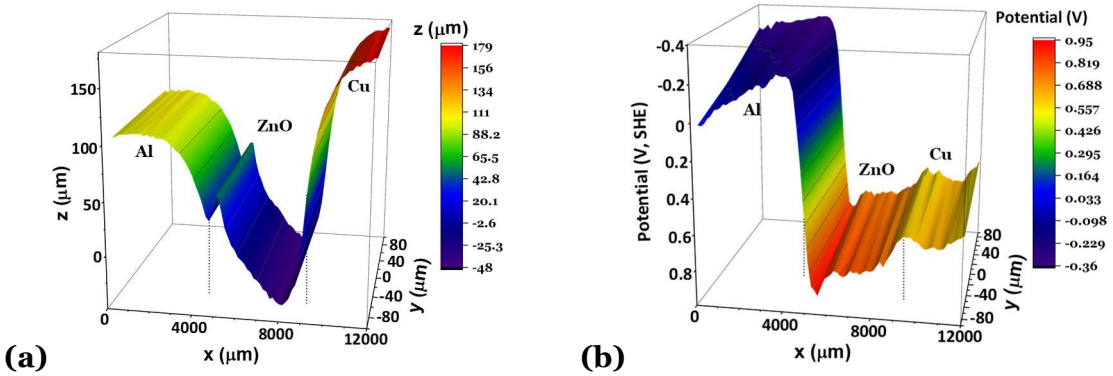

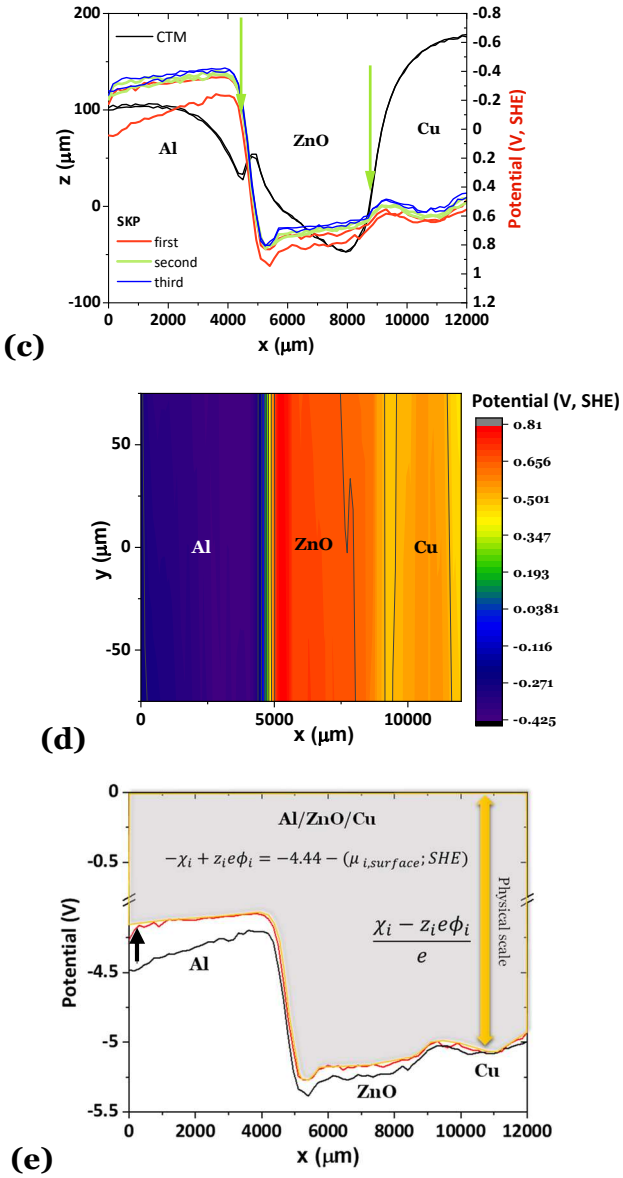

Figure 4 An Al/ZnO/Cu cell when the CTM/SKP circuit is closed through the Al. CTM topography in **(a)** and SKP contact difference potentials in **(b)** to **(e)**. **(c)** plots show no substantial changes when the Al is connected to the SKP instead of Cu, as shown in Fig. 2; after the second line obtained in the first run, all the subsequent SKP experiments show similar surface chemical potentials profile . OCV V_{OC} = 0.066 V obtained after 1h24 [ΔV = 1.00 - ($R_i I$) = 0.066 V]. **(e)** 1D chemical potentials μ_i as a function of the work functions χ_i and surface potentials ϕ_i in an Al/ZnO/Cu heterojunction when Al is connected to the SKP.

The analysis of Fig. 4 shows comparable surface chemical potentials for Cu, Al, and ZnO as when the CTM/SKP is connected to the Al or Cu in Fig. 3 and similar diffusion and eventual drift of electrons from the copper electrode to the ZnO. Nonetheless, there are some subtleties, the more pronounced ZnO surface chemical potential bending towards the positive potentials (SHE scale), at the Al/ZnO interface, in Fig. 4, indicates the presence of an accumulation of positively charged species, such as Zn^{2+} or holes. Conversely, it is shown the accumulation of positively charged species on the ZnO side of the interface ZnO/Cu in Fig. 3c when the SKP is also connected to the Al electrode. These reverse behaviors are in agreement

with the fact that the chemical potentials of both Al and Cu are bigger than the ZnO's (Physical scale), and so an initial accumulation of positively charged species at both interfaces is required to equalize the Fermi levels [50]. This positive charge accumulation detail is more clearly observed in both Cu/ZnO and ZnO/Zn interfaces in Fig. 5 where the cell analyzed is Cu/ZnO/Zn.

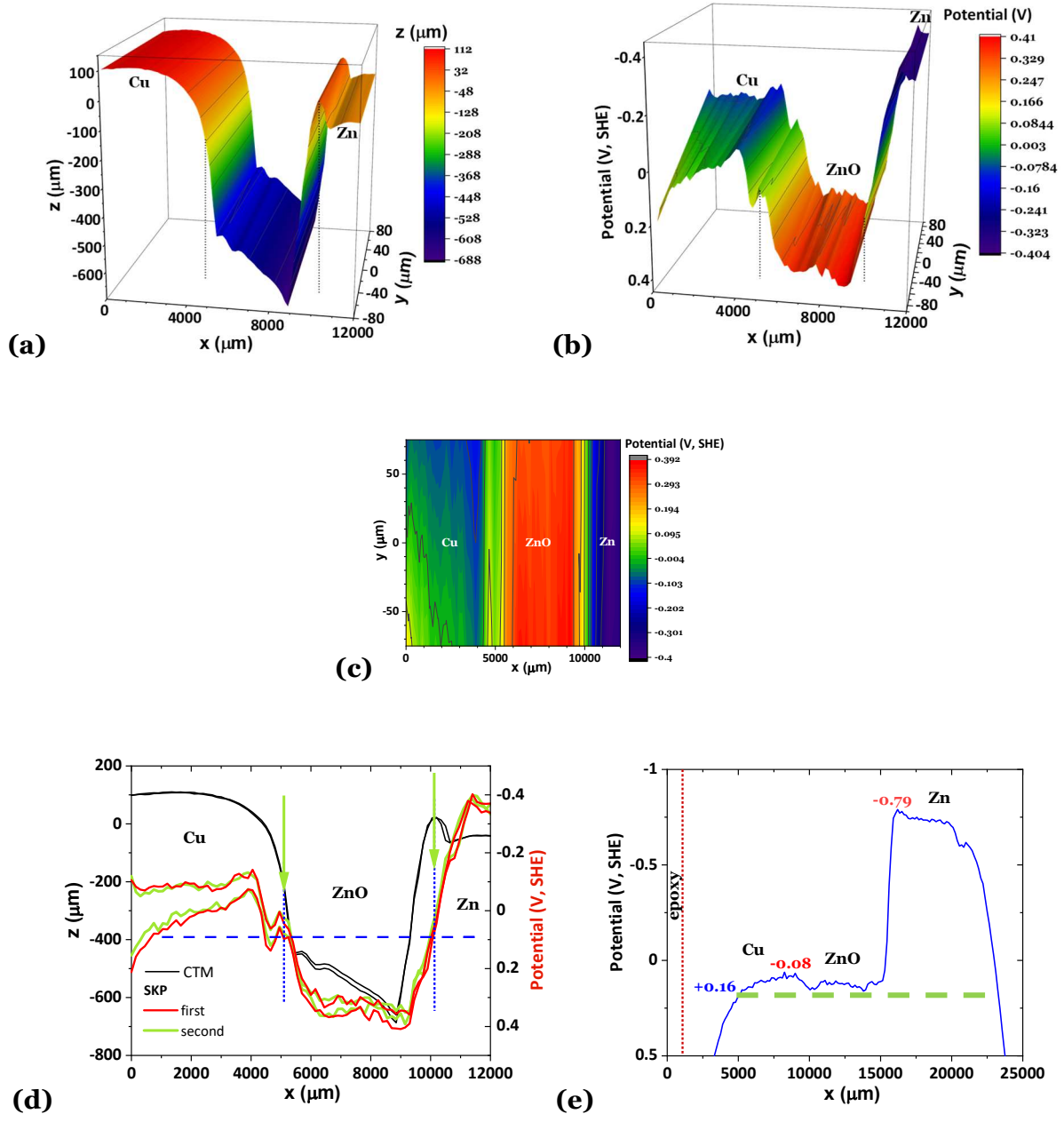

Figure 5 A Zn/ZnO/Cu cell when the CTM/SKP circuit is closed through the Cu. CTM topography **(a)** and SKP surface chemical potentials **(b)**, **(c)**, and **(d)** plots show no substantial changes over time. Time after introducing the ZnO in the cell and performing the CTM scan **(b)** first: 25 min, **(c)** second: 59 min; **(d)** no considerable changes are observed over time and the ZnO polarizes at both surfaces positively to equalize the Fermi levels by forming EDLCs with opposed polarizations. An EDLC followed by the likely formation of an interphase with a higher surface potential seems to have been formed at the Cu/ZnO interface, showing negative/positive/negative charged layers on the Cu side and a positive layer on the ZnO side; all the species involved align their surface

chemical potentials at 0.09 V; **(e)** Surface chemical potentials of the cell scanned from the interface with the epoxy at 0 to 24.15 mm, showing equalization of the three potentials at +0.16 V (full graph at SI, Fig. S4).

The experiments with the Zn/ZnO/Cu cell in Fig. 5 show a resistive element at the Zn/ZnO similar to those shown before at the Al/ZnO interface with the Al/ZnO/Cu cells. In the Al/ZnO/Cu cells, $\Delta V = R_i I$ assumes the values of 1.16 V and 1.07 V (Figs. 2c, and 2d) when SKP is connected to Cu, and 1.31 and 1.24 V (Figs. 4b, and 4d) when SKP is connected to Al, both at the Al/ZnO interface; $\Delta V = R_i I$ is 0.81 and 0.79 V (Figs. 5b and 5c) on Zn/ZnO interface of the Zn/ZnO/Cu cell.

As in the Al/ZnO/Cu cell, the Cu/ZnO heterojunction in Zn/ZnO/Cu is likely to show an EDLC with eventual formation of an interphase due to electron diffusion and drift, characterized in SKP scans by a broad peak pointing to the negative potential axis.

In Figs. 5d and 5e, it is demonstrated one more time how the surface chemical potential of three or four materials in electrical contact through a series of thick layers equalizes their surface chemical potentials in at least one point, which again is understood in the light of plasmonic interactions metal-dielectric reflected on the electric field.

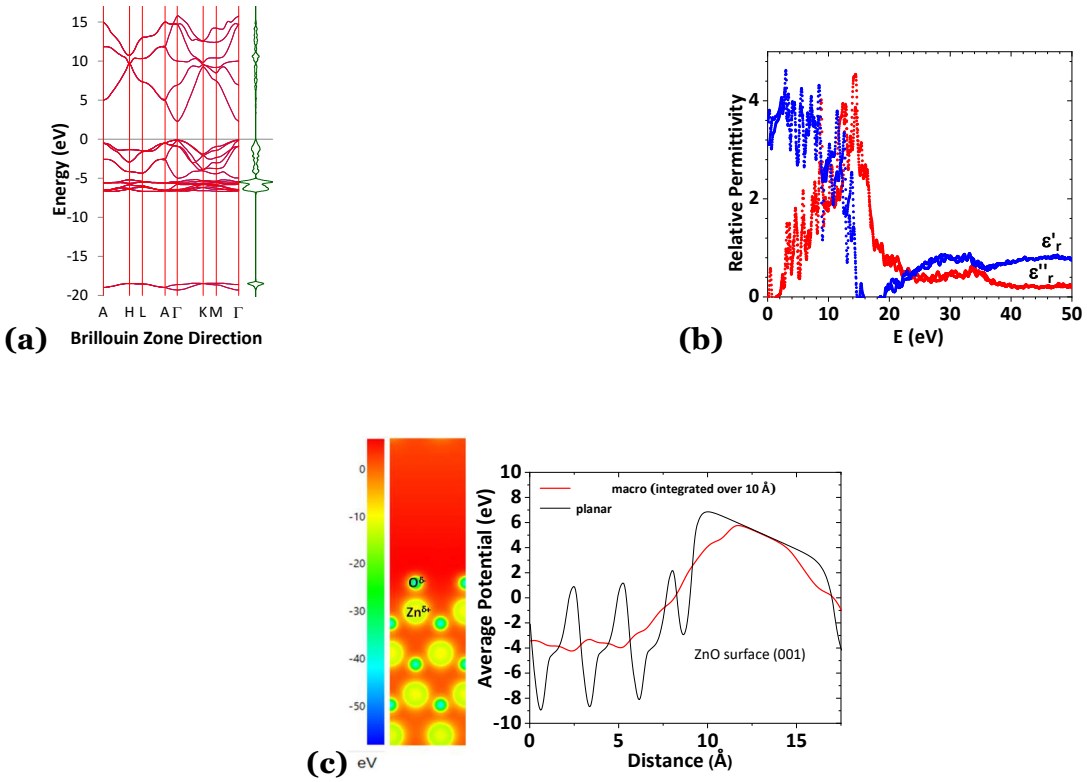

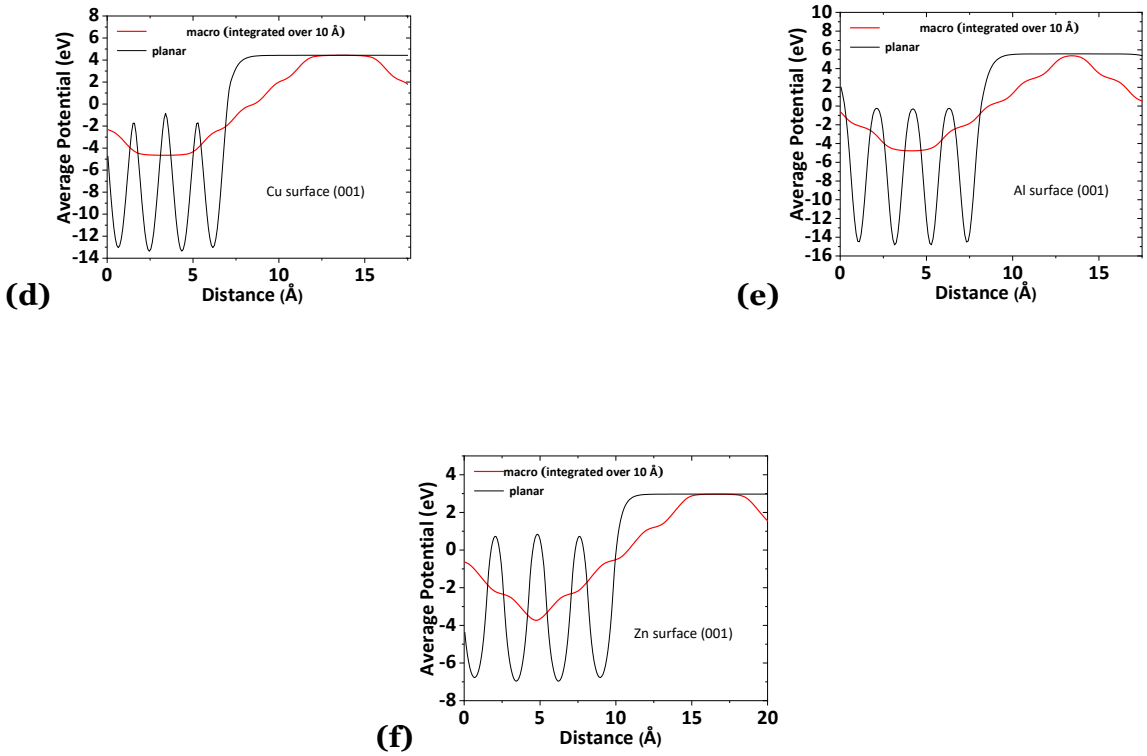

Figure 6 *Ab initio* calculations for ZnO hexagonal $P6_3mc$ space group: **(a)** band structure showing a direct semiconductor and an energy gap of E_g = 2.389 eV (calculations with HS06 functional); **(b)** the relative permittivity tensor vs. energy; dielectric constant $\varepsilon'_r \approx 4$. Theoretical average potential for planar and macroscopic surfaces and *work functions* calculated for a (001) surface: **(c)** χ(ZnO) = 4.74 eV (μ_{ZnO} = +0.30 eV, SHE); **(d)** χ(Cu) = 4.58 eV (μ_{Cu} = +0.14 eV, SHE); **(e)** χ(Al) = 4.69 eV (μ_{Al} = +0.25 eV, SHE); **(f)** χ(Zn) = 3.49 eV (μ_{Zn} = -0.95 eV, SHE).

Theoretical simulations of the ZnO optimized structure in Fig. 6 include the band structure (semiconductor with a direct gap of 2.387 eV, Fig. 6a) and the real ε'_r and imaginary ε''_r relative permittivities' tensor (Fig. 6b). Surfaces were optimized (Fig. 6c), and the average potential and the work functions were calculated (Figs. 6c to 6f). The theoretical work function for the Al, χ(Al) = 4.69 eV (μ_{Al} = +0.25 eV, SHE) calculated for a (001) surface (Fig. 6e) deviates from the absolute chemical potential (-1.66 eV, SHE [47]), indicating the constant presence of a surface electrostatic potential associated with Al ($3\phi_{Al} \approx -1.91\ V$). The *work functions* calculated for (001) surfaces and obtained for ZnO, χ(ZnO) = 4.74 eV (μ_{ZnO} = +0.30 eV, SHE) (Fig. 6c), Cu, χ(Cu) = 4.58 eV (μ_{Cu} = +0.14 eV, SHE) (Fig. 6e), and Zn, χ(Zn) = 3.49 eV (μ_{Zn} = -0.95 eV, SHE) (Fig. 6f), agree with the insulated species' chemical potentials. The *work function* is a surface property and may be affected by the surface orientation; therefore, surfaces with different orientations were simulated beyond those shown in Fig. 6.

The maximum thickness of the ZnO in a solid-state device should be much smaller than ~1 mm whenever the ZnO is deposited on the surface of a negative electrode-like species to avoid highly resistive interactions. ZnO seems to be fitted to deposit on a copper current-collector and be used as a nucleation center to plate an alkali metal, such as lithium, due to the

accumulation of more negatively charged species at the Cu/ZnO interface, as discussed previously.

An essential feature is the surface chemical potentials' gradient capability demonstrated by the electrodes-collectors such as Al, Cu, and Zn in Figs. 2 to 5. The latter capability leads to an equalization of the chemical potentials of all the materials in the cell at the dielectric level as shown in Fig. 3a to 3c. This asseveration indicates that the dielectric or electrolyte is the determinant material, defining the impedance of a cell such as a battery, capacitor, transistor, or photovoltaic.

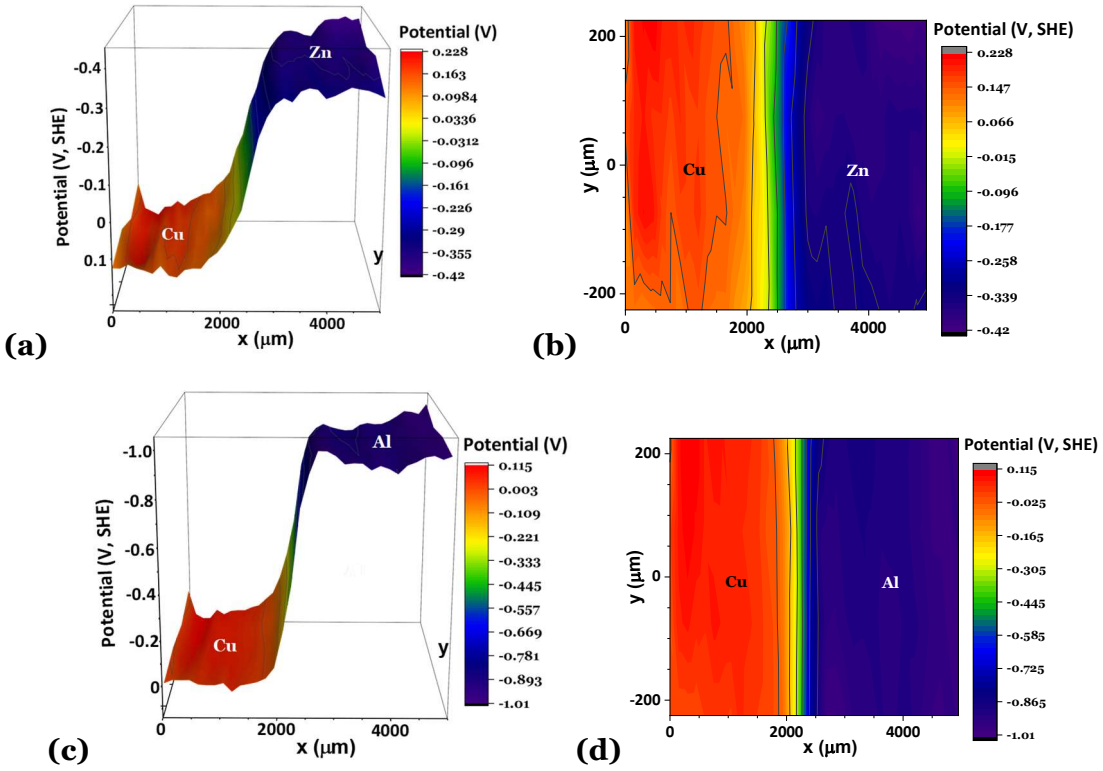

Figure 7 Heterojunctions Zn//Cu and Al//Cu when the SKP circuit is closed through the Cu. A gap of air separates the two metals. The three metals in **(a)** to **(d)** show the potentials they usually display when they are insulated; **(b)** and **(d)** are 2D plots corresponding to **(a)** and **(c)**, respectively. The Al, Zn, and Cu in Zn//Cu and Al//Cu heterojunctions, show flat potentials. Similarly Al/ZnO and Zn/ZnO, ohmic discontinuities are observed for the present Cu/Zn and Cu/Al heterojunctions constituting potential wells.

The SKP plots of Fig. 7 do not show any surface chemical potential gradients at the interfaces Zn//Cu and Al//Cu where the two metals are separated by air that plays the role of a potential well. The metals also show flat surfaces not showing the tendency to bending as observed in the Al/ZnO/Cu and Zn/ZnO/Cu cells. Insulated copper measured as a control, shows an average surface potential of 0.19 V, while varying from 0.166 to 0.216 V, which is in good agreement with the present results.

To summarize, if ions are not free to move towards the interfaces and form EDLCs, where the energy is stored, an impedance corresponding to the difference in chemical potentials of the materials forming the interface, $\Delta V = R_i I$, arises.

Conclusions

Here we analyze two and one heterojunctions-cells where the electrodes are also current collectors. The dielectric is ZnO, which is used in various types of solid-state devices, from photovoltaics to batteries smooth bending of the surface chemical potentials of ZnO, likely reflecting the bending of the conduction and valence bands due to Zn^{2+} diffusion to the interstitial sites with electrons release to the donor band. It is also possible that the bending reflects the polarization, through ionic movement, of the ZnO where the two ends must be polarized positively to bring the electrochemical potential of the ZnO up towards the equalization with the electrochemical potentials of the electrodes-collectors.

The zinc oxide proved to be theoretically suited to be applied on the Cu current collector in anode-less and lithium battery cells to nucleate lithium during charging, as it shows equalization of the surface chemical potentials at the interface, reflecting a negligible resistive element at the same time as it allows for a negatively charged region at the interface. It is noteworthy that here, however, Cu was the positive electrode.

Using a hybrid functional, the band structure of ZnO, including its bandgap and relative permittivity were simulated. The work functions of ZnO, Zn, Al, and Cu were also simulated after their surfaces had been optimized, and are in agreement with the SKP scans of the *in operando* cells.

The surface chemical potentials obtained for the cell's materials, both experimentally with SKP and using *ab initio* simulations, are in agreement with the state of the art.

The metal electrodes-collectors have high dynamics and capability to accumulate tandem charges of equal and opposite signs which results in bending their surface chemical potentials with great amplitude. In the *in operando* cell, the metals reflect a certain emergency to align surface chemical potentials within the cell at the dielectric level. Therefore, indicating that the dielectric effect on the surface chemical potential of the metals is long-range and electric field-based.

The latter novel feature observed in these two heterojunctions cells containing oxides such as ZnO, Al_2O_3, Li_2O (SI, Figs. S2 to S4), but also CaO, MgO, SiO, SnO_2 (not shown in this work), consisting on the alignment of the three materials surface chemical potentials away from the

interfaces and away from the edges of the cell is obtained in a Cu/ZnO/Al cell at [μ_{Cu}(1.86 mm) = μ_{ZnO}(10.60 to 13.40 mm) = μ_{Al}(18.50 mm) = +0.68 eV], and [μ_{Al}(1.54 mm) = μ_{ZnO}(9.54 to 12.05 mm) = μ_{Cu}(19.35 mm) = +0.21 eV] depending on the metal that connects with the SKP. For the Cu/ZnO/Zn cell, the equalized potentials are found at [μ_{Cu}(5.25 mm) = μ_{ZnO}(10.05 and 13.80 mm) = μ_{Zn}(23.25 mm) = +0.16 eV]. It is highlighted that the ZnO is μm-powders in contact with two different bulk metals, forming a metal-insulator-metal multijunction, where the three-point equalization of the surface chemical potentials might be due to a *plasmonic* interaction with applications in photovoltaics and high efficient LEDs.

Acknowledgments

This work was supported by the CAVALI project, with reference POCI-01-0247-FEDER-047728, co-funded by the ERDF, through the COMPETE 2020, under the PORTUGAL 2020 Partnership Agreement and the Portuguese Foundation for Science and Technology FCT UIDP/50022/2020 Emerging Technologies – LAETA. BAM thanks the "FLY.PT—Mobilize the Portuguese aviation industry to disrupt the future urban air transport" project, co-financed by the European Regional Development Fund (ERDF) through Portugal 2020; MHB acknowledges Professor John B. Goodenough for his endowment to the MatER – Materials for Energy Research lab, FEUP.

Contributions

Cell fabrication and SKP experiments: ANG; specific review of state of the art: ANG, MCB, and BAM; conceptualization, formal analysis, supervision: MHB; original draft, review, and editing: All. All authors have read and agreed to the published version of the manuscript.

Data availability

The data that support the findings of this study are available from the corresponding author upon reasonable request.

References

(1) Liu, J.; Bao, Z.; Cui, Y.; Dufek, E. J.; Goodenough, J. B.; Khalifah, P.; Li, Q.; Liaw, B. Y.; Liu, P.; Manthiram, A.; Meng, Y. S.; Subramanian, V. R.; Toney, M. F.; Viswanathan, V. V.; Whittingham, M. S.; Xiao, J.; Xu, W.; Yang, J.; Yang, X. Q.; Zhang, J. G. Pathways for Practical High-Energy Long-Cycling Lithium Metal Batteries. *Nat. Energy 2019 43* **2019**, *4* (3), 180–186. https://doi.org/10.1038/s41560-019-0338-x.

(2) Danzi, F.; Valente, M.; Terlicka, S.; Materials, M. B.-A.; 2022, U. Sodium and Potassium Ion Rich Ferroelectric Solid Electrolytes for Traditional and Electrode-Less Structural Batteries. *APL Mater.* **2022**, *10*, 031111. https://doi.org/10.1063/5.0080054.

(3) Oliveira, J. C. R. E.; Braga, M. H. Increasing the Reactive Surface Area of a Li Three Dimensional Negative Electrode by Morphology Control. *Appl. Phys. Lett.* **2013**, *103* (23), 233901. https://doi.org/10.1063/1.4836579.

(4) Pope, M. A.; Aksay, I. A.; Pope, A.; Aksay, A. Structural Design of Cathodes for Li-S Batteries. *Adv. Energy Mater.* **2015**, *5* (16), 1500124. https://doi.org/10.1002/AENM.201500124.

(5) Yue, J.; Yan, M.; Yin, Y.-X.; Guo, Y.-G.; Yue, J.; Yan, M.; Yin, Y.-X.; Guo, Y.-G. Progress of the Interface Design in All-Solid-State Li–S Batteries. *Adv. Funct. Mater.* **2018**, *28* (38), 1707533. https://doi.org/10.1002/ADFM.201707533.

(6) Liu, Y.; He, P.; Zhou, H. Rechargeable Solid-State Li–Air and Li–S Batteries: Materials, Construction, and Challenges. *Adv. Energy Mater.* **2018**, *8* (4), 1701602. https://doi.org/10.1002/AENM.201701602.

(7) Yang, X.; Luo, J.; Sun, X. Towards High-Performance Solid-State Li–S Batteries: From Fundamental Understanding to Engineering Design. *Chem. Soc. Rev.* **2020**, *49* (7), 2140–2195. https://doi.org/10.1039/C9CS00635D.

(8) Park, S. H.; Jun, D.; Lee, G. H.; Lee, S. G.; Lee, Y. J. Toward High-Performance Anodeless Batteries Based on Controlled Lithium Metal Deposition: A Review. *J. Mater. Chem. A* **2021**, *9* (26), 14656–14681. https://doi.org/10.1039/D1TA02657G.

(9) Tong, Z.; Bazri, B.; Hu, S.-F.; Liu, R.-S. Interfacial Chemistry in Anode-Free Batteries: Challenges and Strategies. *J. Mater. Chem. A* **2021**, *9*, 7396. https://doi.org/10.1039/d1ta00419k.

(10) Heubner, C.; Maletti, S.; Auer, H.; Hüttl, J.; Voigt, K.; Lohrberg, O.; Nikolowski, K.; Partsch, M.; Michaelis, A. From Lithium-Metal toward Anode-Free Solid-State Batteries: Current Developments, Issues, and Challenges. *Adv. Funct. Mater.* **2021**, *31* (51), 2106608. https://doi.org/10.1002/ADFM.202106608.

(11) Ozgur, Ü.; Hofstetter, D.; Morkoç, H. ZnO Devices and Applications: A Review of Current Status and Future Prospects. *Proc. IEEE* **2010**, *98* (7), 1255–1268. https://doi.org/10.1109/JPROC.2010.2044550.

(12) Liang, F. X.; Gao, Y.; Xie, C.; Tong, X. W.; Li, Z. J.; Luo, L. B. Recent Advances in the Fabrication of Graphene–ZnO Heterojunctions for Optoelectronic Device Applications. *J. Mater. Chem. C* **2018**, *6* (15), 3815–3833. https://doi.org/10.1039/C8TC00172C.

(13) Zhu, L.; Li, H.; Liu, Z.; Xia, P.; Xie, Y.; Xiong, D. Synthesis of the 0D/3D CuO/ZnO Heterojunction with Enhanced Photocatalytic Activity. *J. Phys. Chem. C* **2018**, *122* (17), 9531–9539. https://doi.org/10.1021/ACS.JPCC.8B01933.

(14) Zheng, L.; Zheng, Y.; Chen, C.; Zhan, Y.; Lin, X.; Zheng, Q.; Wei, K.; Zhu, J. Network Structured SnO2/ZnO Heterojunction Nanocatalyst with High Photocatalytic Activity. *Inorg. Chem.* **2009**, *48* (5), 1819–1825. https://doi.org/10.1021/IC802293P/SUPPL_FILE/IC802293P_SI_001.PDF.

(15) Uddin, M. T.; Nicolas, Y.; Olivier, C.; Toupance, T.; Servant, L.; Müller, M. M.; Kleebe, H. J.; Ziegler, J.; Jaegermann, W. Nanostructured SnO2-ZnO Heterojunction Photocatalysts Showing Enhanced Photocatalytic Activity for the Degradation of Organic Dyes. *Inorg. Chem.* **2012**, *51* (14), 7764–7773. https://doi.org/10.1021/IC300794J/SUPPL_FILE/IC300794J_SI_001.PDF.

(16) Jeong, M.-C.; Oh, B.-Y.; Ham, M.-H.; Lee, S.-W.; Myoung, J.-M.; Jeong, M.-C.; Oh, B.-Y.; Ham, M.-H.; Lee, S.-W.; Myoung, J.-M. ZnO-Nanowire-Inserted GaN/ZnO Heterojunction Light-Emitting Diodes. *Small* **2007**, *3* (4), 568–572. https://doi.org/10.1002/SMLL.200600479.

(17) Park, N.; Sun, K.; Sun, Z.; Jing, Y.; Wang, D. High Efficiency NiO/ZnO Heterojunction UV Photodiode by Sol–Gel Processing. *J. Mater. Chem. C* **2013**, *1* (44), 7333–7338.

https://doi.org/10.1039/C3TC31444H.

(18) Tsai, S. Y.; Hon, M. H.; Lu, Y. M. Fabrication of Transparent P-NiO/n-ZnO Heterojunction Devices for Ultraviolet Photodetectors. *Solid. State. Electron.* **2011**, *63* (1), 37–41. https://doi.org/10.1016/J.SSE.2011.04.019.

(19) Luo, C.; Li, D.; Wu, W.; Zhang, Y.; Pan, C. Preparation of Porous Micro–Nano-Structure NiO/ZnO Heterojunction and Its Photocatalytic Property. *RSC Adv.* **2013**, *4* (6), 3090–3095. https://doi.org/10.1039/C3RA44670K.

(20) Kavitha, R.; Kumar, S. G. A Review on Plasmonic Au-ZnO Heterojunction Photocatalysts: Preparation, Modifications and Related Charge Carrier Dynamics. *Mater. Sci. Semicond. Process.* **2019**, *93*, 59–91. https://doi.org/10.1016/J.MSSP.2018.12.026.

(21) Sekkat, A.; Bellet, D.; Chichignoud, G.; Muñoz-Rojas, D.; Kaminski-Cachopo, A. Unveiling Key Limitations of ZnO/Cu2O All-Oxide Solar Cells through Numerical Simulations. *ACS Appl. Energy Mater.* **2021**, *2022*, 5433. https://doi.org/10.1021/ACSAEM.1C03939/ASSET/IMAGES/LARGE/AE1C03939_0008.JPEG.

(22) Da Silva, W. J. C.; Da Silva, M. R.; Takashima, K. Preparation and Characterization of ZnO/CuO Semiconductor and Photocatalytic Activity on the Decolorization of Direct Red 80 Azodye. *J. Chil. Chem. Soc.* **2015**, *60* (4), 2749–2751. https://doi.org/10.4067/S0717-97072015000400022.

(23) Panžić, I.; Capan, I.; Brodar, T.; Bafti, A.; Mandić, V. Structural and Electrical Characterization of Pure and Al-Doped ZnO Nanorods. *Mater. 2021* **2021**, *14* (23), 7454. https://doi.org/10.3390/MA14237454.

(24) Kaur, D.; Bharti, A.; Sharma, T.; Madhu, C. Dielectric Properties of ZnO-Based Nanocomposites and Their Potential Applications. *Int. J. Opt.* **2021**, *2021*. https://doi.org/10.1155/2021/9950202.

(25) Look, D. C.; Reynolds, D. C.; Sizelove, J. R.; Jones, R. L.; Litton, C. W.; Cantwell, G.; Harsch, W. C. Electrical Properties of Bulk ZnO. *Solid State Commun.* **1998**, *105* (6), 399–401. https://doi.org/10.1016/S0038-1098(97)10145-4.

(26) Langton, N. H.; Matthews, D. The Dielectric Constant of Zinc Oxide over a Range of Frequencies. *Br. J. Appl. Phys.* **1958**, *9* (11), 453. https://doi.org/10.1088/0508-3443/9/11/308.

(27) Liu, Y.; Lin, D.; Liang, Z.; Zhao, J.; Yan, K.; Cui, Y. Lithium-Coated Polymeric Matrix as a Minimum Volume-Change and Dendrite-Free Lithium Metal Anode. *Nat. Commun. 2016 71* **2016**, *7* (1), 1–9. https://doi.org/10.1038/ncomms10992.

(28) Kumar Pandey, R.; Dutta, J.; Brahma, S.; -, al; Kannan, K.; Radhika, D.; Raghava Reddy, K.; Theerthagiri, J.; Salla, S.; Senthil, R. A.; Nithyadharseni, P.; Madankumar, A.; Arunachalam, P.; Maiyalagan, T.; Kim, H.-S. A Review on ZnO Nanostructured Materials: Energy, Environmental and Biological Applications. *Nanotechnology* **2019**, *30* (39), 392001. https://doi.org/10.1088/1361-6528/AB268A.

(30) Zhang, Y.; Wu, Y.; Ding, H.; Yan, Y.; Zhou, Z.; Ding, Y.; Liu, N. Sealing ZnO Nanorods for Deeply Rechargeable High-Energy Aqueous Battery Anodes. *Nano Energy* **2018**, *53*, 666–674. https://doi.org/10.1016/J.NANOEN.2018.09.021.

(31) Allen J. Bard; Larry R. Faulkner. *Electrochemical Methods: Fundamentals and Applications*, JOHN WILEY.; Department of Chemistry and Biochemistry University of Texas at Austin, 2000; Vol. 2nd Editio.

(32) Reiss, H. The Fermi Level and the Redox Potential. *J. Phys. Chem.* **1985**, *89* (18),

3783–3791.
https://doi.org/10.1021/J100264A005/ASSET/J100264A005.FP.PNG_V03.

(33) Masuda, H.; Matsushita, K.; Ito, D.; Fujita, D.; Ishida, N. Dynamically Visualizing Battery Reactions by Operando Kelvin Probe Force Microscopy. *Commun. Chem.* **2019**, *2* (1). https://doi.org/10.1038/S42004-019-0245-X.

(34) Zhao, W.; Song, W.; Cheong, L. Z.; Wang, D.; Li, H.; Besenbacher, F.; Huang, F.; Shen, C. Beyond Imaging: Applications of Atomic Force Microscopy for the Study of Lithium-Ion Batteries. *Ultramicroscopy* **2019**, *204*, 34–48. https://doi.org/10.1016/J.ULTRAMIC.2019.05.004.

(35) Zhu, X.; Revilla, R. I.; Hubin, A. Direct Correlation between Local Surface Potential Measured by Kelvin Probe Force Microscope and Electrochemical Potential of LiNi 0.80 Co 0.15 Al 0.05 O 2 Cathode at Different State of Charge. *J. Phys. Chem. C* **2018**, *122* (50), 28556–28563. https://doi.org/10.1021/ACS.JPCC.8B10364/ASSET/IMAGES/LARGE/JP-2018-10364J_0007.JPEG.

(36) *SKP Probes - Biologic*. https://www.biologic.net/accessory/skp-probes/ (accessed 2022-06-20).

(37) Yatskiv, R.; Tiagulskyi, S.; Grym, J.; Vaniš, J.; Bašinová, N.; Horak, P.; Torrisi, A.; Ceccio, G.; Vacik, J.; Vrňata, M. Optical and Electrical Characterization of CuO/ZnO Heterojunctions. *Thin Solid Films* **2020**, *693*, 137656. https://doi.org/10.1016/J.TSF.2019.137656.

(38) Ryan O'Hayre, Suk-Won Cha, Whitney Colella, F. B. P. *Fuel Cell Fundamentals*, 3rd editio.; John Wiley & Sons, Inc, 2016.

(39) Kedruk, Y. Y.; Bobkov, A. A.; Gritsenko, L. V.; Moshnikov, V. A. Investigation of the Properties of Zinc Oxide by the Method of Impedance Spectroscopy. *Glas. Phys. Chem.* **2022**, *48* (2), 123–129. https://doi.org/10.1134/S1087659622020043.

(40) *Fundamentals of Electrochemistry*, Wiley-Inte.; Bagotsky, V. S., Ed.; 2005.

(41) Wander, A.; Harrison, N. M. An Ab Initio Study of ZnO(10$\bar{1}$0). *Surf. Sci.* **2000**, *457* (1–2), L342–L346. https://doi.org/10.1016/S0039-6028(00)00418-0.

(42) Ren, D.; Xiang, B.; Gao, Y.; Hu, C.; Zhang, H. Ab Initio Study of Lattice Instabilities of Zinc Chalcogenides ZnX (X=O, S, Se, Te) Induced by Ultrafast Intense Laser Irradiation. *AIP Adv.* **2017**, *7* (9), 095021. https://doi.org/10.1063/1.4999445.

(43) Ellmer, K.; Bikowski, A. Intrinsic and Extrinsic Doping of ZnO and ZnO Alloys. *J. Phys. D. Appl. Phys.* **2016**, *49* (41), 413002. https://doi.org/10.1088/0022-3727/49/41/413002.

(44) Erhart, P.; Albe, K.; Klein, A. First-Principles Study of Intrinsic Point Defects in ZnO: Role of Band Structure, Volume Relaxation, and Finite-Size Effects. *Phys. Rev. B - Condens. Matter Mater. Phys.* **2006**, *73* (20), 205203. https://doi.org/10.1103/PHYSREVB.73.205203/FIGURES/6/MEDIUM.

(45) Braga, M. H.; Dębski, A.; Terlicka, S.; Gąsior, W.; Góral, A. Experimental and Ab Initio Study of the Ag–Li System for Energy Storage and High-Temperature Solders. *J. Alloys Compd.* **2020**, *817*, 152811. https://doi.org/10.1016/J.JALLCOM.2019.152811.

(46) Braga, M. H.; Dębski, A.; Terlicka, S.; Gąsior, W.; Góral, A. The Ag–Li System's Experimental and Ab Initio Thermodynamic Dataset. *Data Br.* **2020**, *28*, 104939. https://doi.org/10.1016/J.DIB.2019.104939/ATTACHMENT/1119AA36-BFEE-4B2F-870C-AF6DF109B9DF/MMC1.ZIP.

(47) Braga, M. H.; Stockhausen, V.; Oliveira, J. C. E.; Ferreira, J. A. The Role of Defects in Li3ClO Solid Electrolyte: Calculations and Experiments. *MRS Online Proc. Libr.* **2013**, *1526* (1), 1–5. https://doi.org/10.1557/OPL.2013.519.

(48) Robertson, J.; Gillen, R.; Films, S. C.-T. S.; 2012, U. Advances in Understanding of Transparent Conducting Oxides. *Elsevier* **2012**, *520* (10), 3714–3720. https://doi.org/https://doi.org/10.1016/j.tsf.2011.10.063.

(49) Trasa'tti, S. The Absolute Electrode Potential: An Explanatory Note (Recommendations 1986). *Pure Appl. Chem.* **1986**, *58* (7), 955–966. https://doi.org/10.1351/PAC198658070955/MACHINEREADABLECITATION/RIS.

(50) Braga, M. H.; Oliveira, J. E.; Kai, T.; Murchison, A. J.; Bard, A. J.; Goodenough, J. B. Extraordinary Dielectric Properties at Heterojunctions of Amorphous Ferroelectrics. *J. Am. Chem. Soc.* **2018**, *140* (51), 17968–17976. https://doi.org/10.1021/jacs.8b09603.